

Trapping and cooling rubidium atoms for quantum information

dissertation

by

Herbert Crepaz

submitted to the Faculty of Mathematics, Computer
Science and Physics of the University of Innsbruck

in partial fulfillment of the requirements
for the degree of doctor of science

advisor: o.Univ.-Prof. Dr. Rainer Blatt,
Institute for Experimental Physics

Innsbruck - Barcelona, December 2006

Abstract

In the last years the quest for full control over the quantum state for cold atoms and photons and their interactions with photons has evolved into the vision of so-called ensemble-based quantum information and quantum interfaces. These systems have demonstrated their potential with the successful experimental implementation of quantum memory, teleportation and single-photon generation.

Typical ensemble-experiments have so far employed Quantum-Non-Demolition (QND) measurements on large-volume room-temperature samples. Applying the same concepts to cold atoms promises significant improvements in coherence time, sample lifetime, and efficient atom-light interaction: high optical densities maximize the coupling and small atom numbers favor quantum- over classical noise. Although incoherent matter, with densities up to 1000 times higher than in conventional laser-light traps tightly confined samples are ideally suited for applications where the light-atom interaction depends on collective enhancement effects.

Apart from QND applications, dense, mesoscopic atom samples allow production of ultracold plasmas and very long-range Rydberg molecular states. In the regime of mesoscopic sample sizes, fast dipole blockade-based Rydberg quantum manipulation becomes possible. At the same time, the tight confinement and high collision rates may produce phenomena which normally appear in the quantum degenerate regime and which are interesting beyond quantum information applications, such as hydrodynamic behavior.

Such advanced applications of cold and dense atomic ensembles require sophisticated trapping and cooling schemes and accompanying diagnostic techniques. This thesis describes the planning, implementation and operation of an experimental set-up for producing and characterizing micron sized, cold and dense rubidium samples. Cold atoms, produced in a double-stage magneto-optical trap, are transferred into a far-off-resonance dipole trap generated by strongly focused laser beams from a Yb:YAG disk laser system at 1030 nm. Samples, ranging from several 10^4 down to few atoms, with μK temperatures and densities up to $8 \cdot 10^{14}$ atoms/cm³, are stored for several seconds and their properties are characterized in detail.

The trapped atoms are efficiently detected by resonant excitation; atom numbers are obtained by a calibrated photodiode, and temperatures are extracted by time-of-flight imaging, either on a CCD-camera system or on a photomultiplier.

Energy-selective resonant excitation of the trapped atoms is made possible by to the strong AC Stark shift imposed by the high intensity of the trapping light. This allows for the spectroscopic investigation of energy distributions, atomic level shifts, and sample extensions, and thus for the determination of temperatures and heating rates, as well as thermalization studies. Due to the tight confinement with radial oscillation frequencies up to 80 kHz, the measured energy distributions depend strongly on the geometry of the confining potential.

Measured spectra are consistent with model calculations based on a non-interacting, thermal Bose-gas confined in an anisotropic, 3-dimensional, Gaussian potential.

The measurement tools which have been developed and demonstrated allow precise determination of parameters such as atom number, sample densities and cloud extensions, which are important for the optimization of QND-type interaction as well as for other QI applications.

Zusammenfassung:

Das ständige Streben nach präziserer Kontrolle von immer größeren Ensemble kalter Atome und Photonen und Ideen, diese nutzbringend anzuwenden, führte zu dem, was wir heute unter Ensemble-Quanteninformation und Quanten-Licht Schnittstelle verstehen. Mit der experimentellen Demonstration der Speicherung von Quanteninformation und Teleportation wurde das Potential dieser Systeme eindrucksvoll dargestellt.

Bisher wurde die überwiegende Anzahl dieser Experimente jedoch mit Atomen bei Raumtemperatur durchgeführt und basiert eher auf einer Ausnutzung cleverer physikalischer Ideen als auf aufwändiger Technologie. Ein Übertragen dieser Konzepte auf kalte Atome verspricht signifikante Verbesserungen. Mit Hilfe ausgeklügelter Speicher- und Kühlverfahren und dazugehöriger Zustandsdiagnostik können bestehende Limits durchbrochen werden. Präzise Kenntnis der physikalischen Parameter kalter Atome und hohe optische Dichten sind wichtig für eine Optimierung der QND-Atom-Licht Wechselwirkung durch Maximierung der Kopplungsstärke und Anpassung der Test-Lichtfelder an die Geometrie der Atomwolke.

Unabhängig davon ermöglichen kalte und dichte atomare Ensemble die Produktion von kalten Plasmen und Rydberg-Gasen. Obwohl nichtentartete Quantengase, mit bis zu 1000 mal höheren Dichten als in konventionellen Laser Lichtfallen, eignen sich diese Systeme ausgezeichnet wo die Wechselwirkung von kollektiven Verstärkungs-Effekten abhängt wie Spin Squeezing, Quantenspeicher oder Einzelphoton-Quellen. Die mesoskopische Größe des Ensembles ist dabei eine Notwendigkeit, um Dipol-Blockade basierte Rydberg-Quantengatter zu implementieren. Gleichzeitig können durch die starke Lokalisierung und hohen Kollisionsraten Effekte entstehen, die normalerweise nur im quantenentarteten Regime zugänglich sind, wie hydrodynamisches Verhalten.

Diese Arbeit beschreibt Planung, Aufbau und Betrieb eines Experimentes, das mesoskopische, kalte und dichte Rubidium Atom-Ensemble untersucht. Kalte Atome, erzeugt in einer zweistufigen magneto-optischen Falle, werden in eine Dipolfalle transferiert, bestehend aus ferverstimmten, fokussierten Lichtfeldern eines Yb:YAG disk-Laser Systems bei 1030 nm.

Mikro Kelvin kalte Ensemble, von einigen 10^4 bis hinunter zu wenigen Atomen und mit Dichten von bis zu $8 \cdot 10^{14}$ atomen/cm³, werden einige Sekunden lang gespeichert und deren Eigenschaften detailliert charakterisiert. Die gespeicherten Atome werden dabei durch resonante Anregung effizient detektiert. Die Atomzahl Bestimmung erfolgt mittels einer kalibrierten Photodiode, Temperaturen werden durch time-of-flight Abbildungen auf die CCD-Kamera oder den Photomultiplier extrahiert.

Spektroskopie durch Energie selektive resonante Anregung wird ermöglicht durch die starke AC-Stark Verschiebung der Energiezustände im intensen Lichtfeld des Fallen-Lasers. Gemessene Energieverteilungen sind stark abhängig von der Geometrie des einschließenden Potentials und lassen Rückschlüsse auf die Temperatur, Heizraten und Thermalisierungsdynamik zu. Durch die starke Lokalisierung, mit Fallen-Oszillationsfrequenzen bis zu 80 KHz und hohen Kollisionsraten ergibt sich eine stark Fallengeometrie bedingte Besetzungsverteilung. Gemessene Spektren werden verglichen mit Modellrechnungen basierend auf einem nichtwechselwirkenden, thermischen Bose-Gas in einem anisotropen, 3-dimensionalen Gauß' schen Potential.

Contents

1	Introduction	1
2	Experiment Control	6
2.1	The CCD System	6
2.2	The General Control System	8
2.2.1	The hardware	9
2.2.2	The Software	9
3	Cold Atom Production	12
3.1	Doppler Cooling	13
3.2	Sub-Doppler Cooling	13
3.3	The Magneto-Optical-Trap	14
3.4	Experimental Setup	17
3.4.1	The Main Apparatus	17
3.4.2	The 2-D MOT System	17
3.5	Atom detection	22
3.5.1	The Photo-Diode	22
3.6	Loading of the 3D-MOT	24
3.7	Temperature and Density	28
4	Optical Dipole Trapping	33
4.1	The Dipole Potential	34
4.1.1	The classical point of view	34
4.1.2	The quantum description	38
4.2	Multilevel Atoms	42
4.2.1	Fine and Hyperfine interactions	44
4.3	Gaussian Beam Traps	47
5	The dipole laser setup	50
5.1	The Dipole-Laser	50
5.1.1	Power Stability and Noise Performance	51
5.2	Light Distribution	54
5.2.1	Beam Path	54
5.2.2	The Acusto-Optic Modulator	55
5.2.3	Fiber Coupling	55
5.2.4	Dipole Optics at the Trap	57
5.3	The Photomultiplier	58
5.3.1	Total detection efficiency	60

6	Laser Trapping of Rb	61
6.1	The Loading Cycle	61
6.1.1	Timing Sequence	61
6.1.2	Overlap of the Dipole Trap and MOT	62
6.2	Recapture Detection	63
6.3	Photomultiplier Detection	64
6.3.1	Free Atoms	64
6.3.2	Trapped Atoms	67
6.3.3	Loading Efficiency	67
6.3.4	Losses in the dipole trap	70
6.3.5	Trap oscillation frequencies	74
6.4	Sample Temperature	76
6.4.1	Imaging through a fixed aperture	76
6.4.2	Density of trapped atoms	82
6.5	Trap-State Spectroscopy	83
6.5.1	3D Harmonic Oscillator Model	83
6.5.2	Adaptation to the Gaussian Potential	85
6.5.3	Measurements	87
7	Outlook	98
7.1	Collective spin operators	98
7.2	Polarization states	99
7.3	Spin squeezing	99
8	Appendix A	102
9	Appendix B	107
10	Appendix C	114
11	Appendix D	116

1 Introduction

The lure of precise control over the quantum degrees of freedom has attracted scientists for much of the past century.

Starting with the invention of Isidor Isaac Rabi [1], who used radio-frequency resonance techniques on atomic and molecular beams in 1938, coherent control became possible. In 1949 Norman Ramsey [2] had the ingenious idea to separate the microwave interaction fields with a radiation free zone, allowing considerably longer measurement times. This first atom interferometer principle, based on the quantum interference between internal atomic states, serves now as a key element inside atomic clocks. The frequency of a microwave oscillator locked to the 9.2 GHz hyperfine transition of ^{133}Cs can now be determined to nearly 15 digits precision. It was well known that faster oscillators make better clocks. For even higher precision, Ramsey's method had to be transferred from the microwave regime to the higher frequency optical domain. However optical resonance techniques suffer from the Doppler broadening caused by the thermal motion of the atoms. More precise control over the external degrees of freedom was necessary. Optical cooling provided a solution.

Bose-Einstein condensation, precision spectroscopy and optical clocks are among the most spectacular applications of cold atom physics. Three Nobel prizes awarded in the last decade witness the the vast richness of new insights and research opportunities gained.

The earliest idea of optical cooling was proposed by Alfred Kastler in 1950, but not seriously considered before tunable laser sources were available. In 1975 Hänsch and Schawlow [3] realized that such light sources could exert considerable forces on atoms making them useful for cooling. First demonstrations 1978 by Neuhauser et al [4] with Ba^+ -ions and by Wineland and coworkers [5] with Mg^+ -ions confined in a trap, marked the beginning of a new era.

An intuitive picture of laser cooling is the transfer of energy and entropy from the ensemble of atoms or ions being cooled to the radiation field. The simplistic explanatory picture of energy and momentum transfer by absorption-emission cycles known as Doppler cooling was established, but it was challenged when experiments provided evidence of colder atomic samples than expected¹ [6]. Further experimental and theoretical investigation elucidated that the complex multi-level structure of alkali elements and the spatial polarization dependency of the light field plays an important role [7]. Several new cooling schemes were identified, common to all - the use of spontaneous scattering, and it was found that efficient optical cooling comes to halt at the single photon recoil level. Again a fundamental cooling limit seemed to be in place, the kinetic energy associated with the recoil of one photon. Soon it became clear that to avoid this recoil-limit², to achieve sub-micro Kelvin temperatures, the atoms would need to be decoupled from the light field once they are cold.

¹Doppler cooling is limited by the linewidth Γ of the optical transition. $k_B T = \hbar \frac{\Gamma}{2}$

²The recoil limit for alkali elements is in the range of $10^{-7} - 10^{-6}\text{K}$

Two optical cooling methods successfully surpassed the limit. One uses optical pumping into excitation free dark states around $v = 0$ called *velocity selective coherent population trapping (VSCPT)* [116]. The other one is based on velocity sensitive Raman transitions and was named *stimulated Raman cooling* [117]. With both it is possible to cool in 1, 2, or 3 dimensions, but cooling time increases significantly with dimensionality because of the probabilistic character how the steady state is reached.

Subsequently more passive cooling schemes were tested, not relying on optical fields. The most successful one is forced evaporation cooling, leading to phase space densities high enough to enter the quantum degenerate regime [8]. When the thermal de Broglie wavelength ($\Lambda = \sqrt{\frac{2}{2 \cdot \pi \cdot m \cdot k \cdot T}}$) of neighboring atoms is large enough they start to overlap and interfere. A large single wave function of the whole ensemble builds up, essentially leaving all the atoms in a precisely defined, macroscopic collective quantum state.

The discovery of micro- and nano-Kelvin samples of dilute atomic gases opened a new approach to long standing theoretical predictions [9]. Bose-Einstein condensates allow for unparalleled control over its properties and stand as a benchmark for our ability to create well defined sets of quantum states of photons and atoms.

Out of this, quantum state engineering emerged as a branch of quantum optics, relying entirely on the ability to cool to the ground state and to manipulate the internal states with sufficient precision [13].

The forces exerted by light can also bring about spatial confinement [9]. Arrangements using the scattering force combined with magnetic fields (Magneto optical trap) [10] or gradient laser beams with induced electric dipole moments (dipole traps) [11] became a central part of many quantum optics experiments and as well subject of intensive research.

Also atomic collisions lost some of their mysteries. The extremely low temperatures afforded by laser cooling largely reduces the range of energies participating in collisional interactions. In the ultracold regime atom-atom interactions can be characterized by a single parameter, the scattering length. This remarkably simplicity led to a detailed understanding about the quantum nature of their interactions [14]. Experiments confirmed theoretical predictions that with the help of external magnetic fields, atom-atom interaction strengths in alkali atoms can be tuned at will because these depend on the position of individual quantum levels [15]. Unprecedented studies of the transition from a non-interacting, dilute gas to a strongly-interacting quantum gas were within reach [16]. A seminal contribution was the realization of the Mott-insulator transition [17], which provided an entire lattice of (maximally) number squeezed atoms - an ideal starting point for quantum information applications. Recently the gap between solid state many body systems and dilute quantum gases had been bridged. Almost exactly 10 years after the first bosonic condensate evidence of fermionic super-fluidity was presented in 2005 [18], showing unambiguous proof of frictionless flow in quantum matter. Strongly correlated fermionic systems promise new prospects for the understanding of high temperature superconductivity [19], neutron stars and the simulation of crystal lattices [20], [21].

With the confinement of atoms and ions to the lowest quantum states [22], the spatial extend of the wave function becomes well defined and the strength and duration of the interactions controllable. Quantum information processing requires such a controlled environment with well understood couplings. Quantum states in cold atoms offer unmatched stability which

mark them out among the most promising physical systems for quantum computation implementations [23], [24], [25].

Parallel with developments in coherent manipulation of matter fields, capabilities in generation and control over light fields were perfectionized. A number of technological advances paved the way. Short term stability of laser sources improved by locking them to ultra-stable cavities [26], [27], extremely low loss dielectric mirrors allow the fabrication of high-Q reference cavities and cold atoms or ions serve as a long term frequency reference [28]. However what was long missing was an optical frequency counter, able to act as a clockwork mechanism. Harmonic frequency chains, available since the 1960, required vast resources and were too tedious to operate. A revolutionary solution was found 1999, using a mode-locked femtosecond laser producing a comb like spectrum of frequencies [29, 30]. Now both time- and frequency- domain properties of pulse trains can be optimized to a high degree. Exciting possibilities like full spectral phase control, even with few cycle light pulses [31] or real-time studies of sub-picosecond dynamics with absolute frequency precision [32], [33] promise an interesting future.

In the last years the quest for full control over larger and larger ensembles of cold atoms and photons has evolved into what is called ensemble- based quantum information and quantum interfaces. Quantum information storage and exchange is an integral part of full-scale quantum information systems. Long lived entangled objects shared over long distances promise the realization of distributed quantum networks and quantum secret sharing. Photons as information carriers can travel unaffected long distances and easily be detected, but they are hard to localize and store³. Atoms on the other hand excel at these tasks. Manipulation and storage can be done via long lived internal states with high precision. But mapping the quantum states of atoms onto light and vice versa in a reversible and coherent way poses a formidable challenge. Two strategies have emerged. The conceptually simpler one involves the coherent coupling of a single photon with a single, localized atom [118]. In practice this requires high-Q resonators, to reach the necessary coupling strength and sophisticated atom manipulation techniques [119, 120]. The second approach, in some sense, exchanges the role of atoms and photons. Instead of increasing the photon density by the number of round-trips inside a cavity, a large ensemble of atoms is used where the weak photon coupling is amplified by the large number of collectively interacting atoms. Strong interaction for atomic samples translates then into high on-resonance optical density, experimentally alleviating many of the stringent requirements of cavity-QED. First implementations, following the proposal of Kuzmich et al. [122], concentrated on the complete absorption of entangled light modes by V-type atomic level structures, thus creating entanglement in the excited states. In 1999, Hald and coworkers [121] succeeded in exciting cold cesium atoms with squeezed light, showing that macroscopic ensembles of atoms (10^6) can be entangled. Subsequent improvements, such as the use of Raman transitions between ground states to avoid spontaneous emission and electromagnetically induced transparency (EIT) for the controllable generation, storage and retrieval of single-photon pulses followed [123, 124]. Another milestone was the introduction of feedback into the quantum-light interface [126, 127]. Here a QND measure-

³With the best optical resonators available today, photons can be stored only for timescales on the order of some 10^{-5} seconds.

ment correlates fluctuations in the polarization of faint light pulses with spin-fluctuations in a collection of atoms. After a projective measurement, feedback is applied to the atoms conditioned on the measurement outcome. In two important proof-of-principle experiments, the versatility of the ensemble approach was demonstrated. For the first time, the quantum state of a light pulse has been deterministically teleported to an object of different nature, a macroscopic ensemble of atoms [125] and a quantum memory was implemented [128].

For the future much work remains before ensemble-based systems will become practical tools. Quantum information is more advanced in dealing with photonic qubits than with weak coherent states and lacking a large nonlinear response makes it difficult to achieve the high fidelities required for error correction and quantum repeater based networks. Up to now most of the break-through experiments have been done with room-temperature atomic ensembles, relying more on clever schemes than experimental complexity. Applying these concepts to cold, trapped atoms promise significant improvements. One reason is that the ratio of quantum- to classical component of the state information increases by reducing the sample size, while the higher particle density of cold atomic samples retains the overall interaction strength compared with gas cells. Also decoherence is reduced in cold atoms owing to the strongly reduced motional effects. Precise knowledge of the physical parameters of the cold samples is important as it will allow optimization of the atom-light interaction by maximizing the mode-matching. Although incoherent matter, with densities up to 1000 times higher than in conventional laser-light traps tightly confined samples are ideally suited for applications, where the light-atom interaction depends on collective enhancement effects.

Apart from QND applications, dense, mesoscopic atom samples allow efficient production of ultracold plasmas and ultra long-range Rydberg molecular states [133–135]. In the regime of mesoscopic sample sizes, fast dipole blockade-based Rydberg quantum manipulation becomes possible [129, 136]. At the same time, the tight confinement and high collision rates may produce phenomena which normally appear in the quantum degenerate regime and which are interesting beyond quantum information applications, such as hydrodynamic behavior [130, 137].

Such advanced applications of cold and dense atomic ensembles require sophisticated trapping and cooling schemes and accompanying diagnostic techniques.

This thesis is dedicated to the implementation and diagnostics of micron sized cold rubidium samples stored in a far-off-resonance dipole trap generated by strongly focused laser beams from a Yb:YAG disk laser at 1030 nm. It describes the design, set-up, and operation of the trap, the development and implementation of diagnostic tools, in particular spectroscopy of the trapped atoms, and the results of that characterization.

Cold atoms, produced in a double-stage magneto-optical trap, are transferred into a far-off-resonance dipole trap generated by strongly focused laser beams from a Yb:YAG disk laser system at 1030 nm. Samples, ranging from several 10^4 down to few atoms, with μK temperatures and densities up to $8 \cdot 10^{14}$ atoms/cm³, are stored for several seconds and their properties are characterized in detail.

The trapped atoms are efficiently detected by resonant excitation; atom numbers are obtained by a calibrated photodiode, and temperatures are extracted by time-of-flight imaging, either on a CCD-camera system or on a photomultiplier.

Energy-selective resonant excitation of the trapped atoms is made possible by to the strong AC Stark shift imposed by the high intensity of the trapping light. This allows for the spectroscopic investigation of energy distributions, atomic level shifts, and sample extensions, and thus for the determination of temperatures and heating rates, as well as thermalization studies. Due to the tight confinement with radial oscillation frequencies up to 80 kHz, the measured energy distributions depend strongly on the geometry of the confining potential.

Measured spectra are consistent with model calculations based on a non-interacting, thermal Bose-gas confined in an anisotropic, 3-dimensional, Gaussian potential.

The measurement tools which have been developed and demonstrated allow precise determination of parameters such as atom number, temperature, sample densities and cloud extensions, which are important for the optimization of QND-type interaction as well as for other QI applications.

The use of the set-up and the diagnostic tools for preparing an optimum sample for cold ensemble-based quantum information will be discussed as the outlook of the work.

2 Experiment Control

For quantum optics experiments, precise and if possible automatized control and actuation of all the electronic and electro-optical systems is of paramount importance. Core experiment control, photomultiplier system, camera system and data acquisition need to be synchronized and controllable in an easy way. The following section contains a description of the implementation in our experiment.

2.1 The CCD System

The system we use for imaging the atoms is a COHU 4912-5010 CCIR-monochrome CCD-Camera without IR-filter.

The 4912 monochrome Camera uses a 1/2-inch format interline transfer sensor with on-chip microlenses¹. This sensor offers lower dark current, image lag, and blooming than other types of sensors. It has 752 (H) x 582 (V) pixels with a pixel size of 8.6 (H) x 8.3 (V) micron and an eight step electronic shutter for exposure time control.

Operation of the camera can be either in continuous mode for imaging on a standard TV-monitor or in triggered mode with the help of a framegrabber².

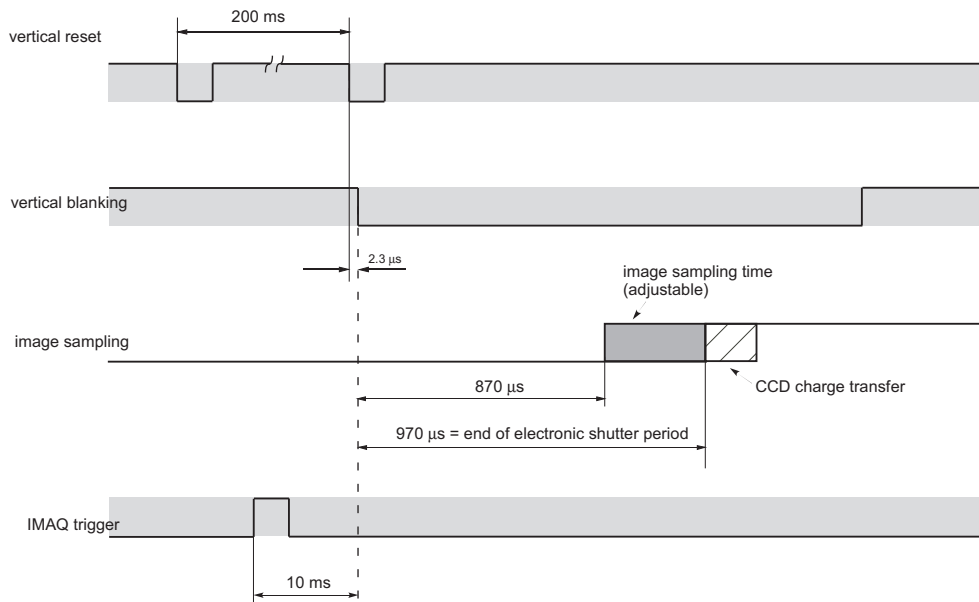
Standard video cameras are not built for taking precisely timed images due to the interlaced mode in which they deliver the pixel information (The video image consists of two consecutive fields with one comprised of all odd lines and the other one containing all even lines). For the purpose of taking snapshot pictures our camera can be operated in non-interlacing field mode, with the drawback that the vertical resolution is only 287 lines (half the full resolution). Progressive scan cameras avoid this drawback and deliver a full resolution image at once, however at higher system costs.

To get deterministic timing the camera can be asynchronously reset by application of a negative-logic TTL-pulse to the AUX-connector. This initiates a vertical-blanking interval $2.3 \mu\text{s}$ later, followed by the video output of the first field. The vertical reset pulse should be applied several multiples of the vertical-sync intervall (20 ms) in advance. This guarantees that the PLL in the camera has stabilized and the video fields delivered by the camera are uninterrupted.

The actual integration time or image sampling time is dependent on the electronic shutter setting and ranges from $100 \mu\text{s}$ to 20 ms.

¹Sony ICX249AL

²National Instruments PCI-1408 monochrome, 8-bit ADC, RS170/CCIR image acquisition board



(a) Timing sequence of the trigger pulses applied to the Cohu 4910 camera. In the example shown, the image sampling time is 100 microseconds.

Figure 2.1:

The end of the shutter period is always fixed at $970 \mu s$ (see 2.1) after the vertical blanking interval, the beginning is variable depending on the shutter setting.

For the expansion pictures of the atomic cloud the shutter was set to $1/10K = 100 \mu s$ or $1/4K$ which resulted in $230 \mu s$ actual integration time. The exact timing was calibrated with acousto-optically switched light pulses from a diode laser applied to the CCD chip. After the pixel information had been stored on the CCD-chip a charge transfer is initiated and the first video field is written to the output. The framegrabber board which requires a trigger pulse in advance digitizes then the video signal. Limitations of the locking circuitry on the framegrabber board when the camera is asynchronously reset required the development of an external genlock circuit to recover all clock signals from the video signal (for a detailed description see Appendix C)

A high quality photo-camera objective³ was attached to the camera with an adapter allowing back-focus adjustment.

The pixel size was calibrated by imaging a precision metal ruler and found to be $8.53 (H) \times 8.27 (V) \mu m$, which corresponds to 750×580 active picture elements.

The digitized images taken from the framegrabber are processed with a LabView⁴ program using Matlab⁵ code for data processing and analyzing.

³Nikon, $f=50 \text{ mm}$, $NA=0.42$

⁴Nationa Instruments Inc. LabView 7.0

⁵Mathworks Inc. Matlab R13

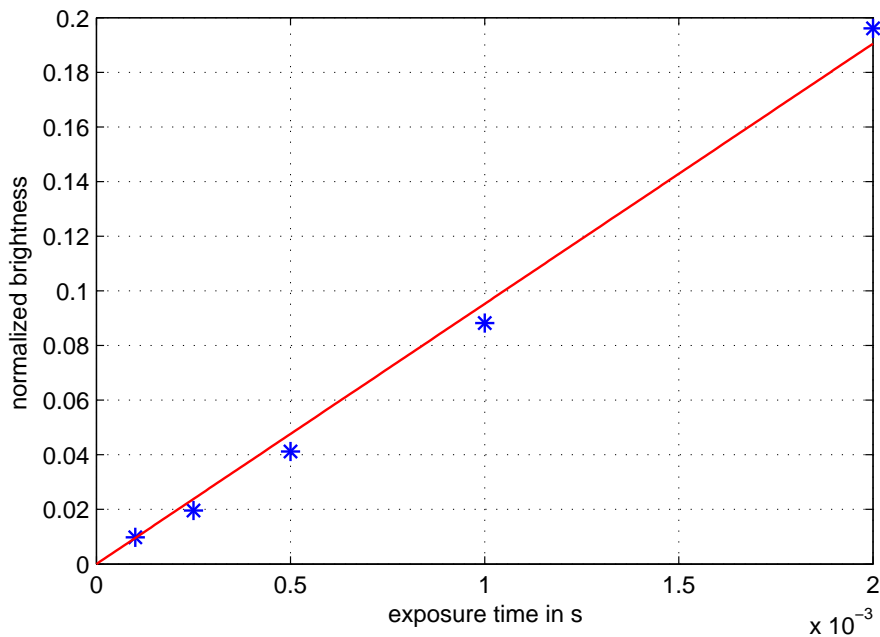
(a) Video signal transfer function measurement and linear fit confirming that $\gamma = 1$

Figure 2.2:

Gamma Calibration

Our camera features a continuous gamma adjustment between 0.45 and 1⁶. A gamma setting less than one results in a nonlinear response that favors black areas at the expense of white ones. For measurement purposes the transfer function should be linear ($\gamma = 1$) to achieve a proportionality between recorded intensity and video-signal amplitude.

For calibration (10.2) a laser beam was imaged onto the chip and the brightness values were recorded depending on different exposure times and gamma settings. The intensity values of 8×2 pixels were summed up and normalized. Each data point shows the average over 5 measurements. For a constant input intensity, the accumulated charge from each CCD-pixel is proportional to the exposure time. The output brightness signal is therefore proportional to the exposure time if $\gamma = 1$.

2.2 The General Control System

A typical experiment sequence can run over several seconds up to a minute with a time resolution of 100 microseconds. During this time a large number of optical and electronic

⁶The gamma transfer function relates the input intensity to the output signal level according to the power law:

$$Sig_{out} = I_{in}^{\gamma}$$

elements needs to be deterministically controlled and operated with high precision. This is not an easy task, taking the heterogeneity, number of channels required (analog inputs and outputs, digital inputs and outputs) and the flexibility in changing sequences into account. Several different systems such as a network of programmable synthesizers, data acquisition cards, pattern generators, real-time systems with dedicated hardware or reconfigurable logic devices (FPGA) may be used for the task of controlling an experiment. For our system we have chosen a combination of several data acquisition cards in conjunction with the software system LabView, all from National Instruments. Considering the system costs and the total flexibility in programming the cards, other options were ruled out.

2.2.1 The hardware

Basis of the timing system is a standard PC (1.3 GHz, 264 Mb RAM) equipped with a PCI-DIO-32HS high speed digital input/output (I/O) board. The system has 32 buffered TTL-logic channels, organized in 2 ports each having 16 channels. All channels are connected to a backplane by ribbon cable, so that the signals can be routed with BNC cables.

For analog voltage output a PCI-6713 8-channel, 12 bit, 1 Ms/s board is used which controls the frequency of the cooling laser, the MOT-magnetic field strength and the amplitudes of the repump, cooling and dipole lasers.

To read-in analog signals a AT-MIO-DE-10 ISA-board provides 16 single-ended or 8 differential inputs and is capable of digitizing with 12 bit resolution at up to 100 Ks/s. One channel was assigned to read in the signal from the calibrated photodiode for atom detection.

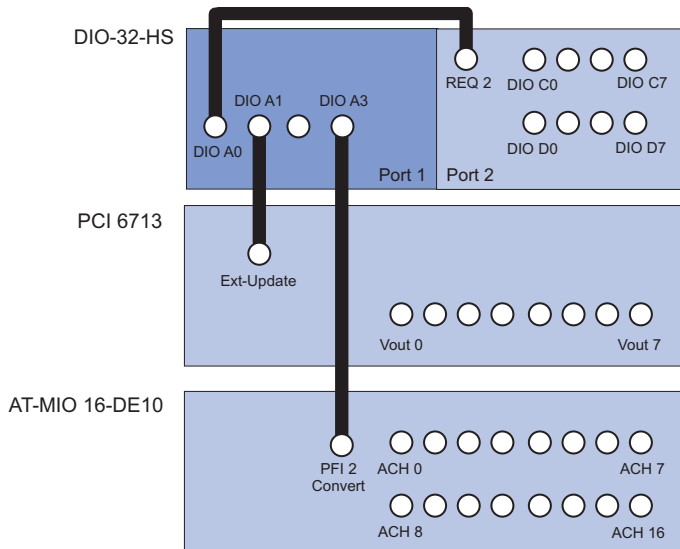
Deterministic timing requires that all internal clocks which govern data acquisition and generation are phase locked. Our system guarantees this by providing custom timebases specific for each card, generated by the high speed digital card. These custom timebases then update directly the ADC and DAC⁷ converters on the analog-input and -output boards thus bypassing all onboard clocks.

As can be seen from figure 8.3 the first port (the first 16 channels) of the DIO-32-HS are dedicated to the generation of the time bases of the data acquisition cards.. Update pulses are then sent to port 2 of the card which is programmed for digital pattern generation with handshaking in burst mode. With this configuration, the remaining 16 digital output channels of port 2 can be used for experiment control. Analogously DIO-1 and DIO-3 deliver update-clock pulses to the Ext-Update input on the analog-output card and to the PFI-2/Convert input on the AT-MIO card.

2.2.2 The Software

LabView was chosen for the ease of programming, the large range of supported hardware and instrument drivers and the hassle free operation in conjunction with the data acquisition (DAQ) hardware from the same manufacturer. LabView is not well suited to handle and process efficiently large amount of data so Matlab subprograms were included to implement

⁷Digital to analog converter (DAC) and analog to digital converter (DAC)



(a) Distribution scheme of the specific timebases to the DAQ boards on the backplane.

Figure 2.3:

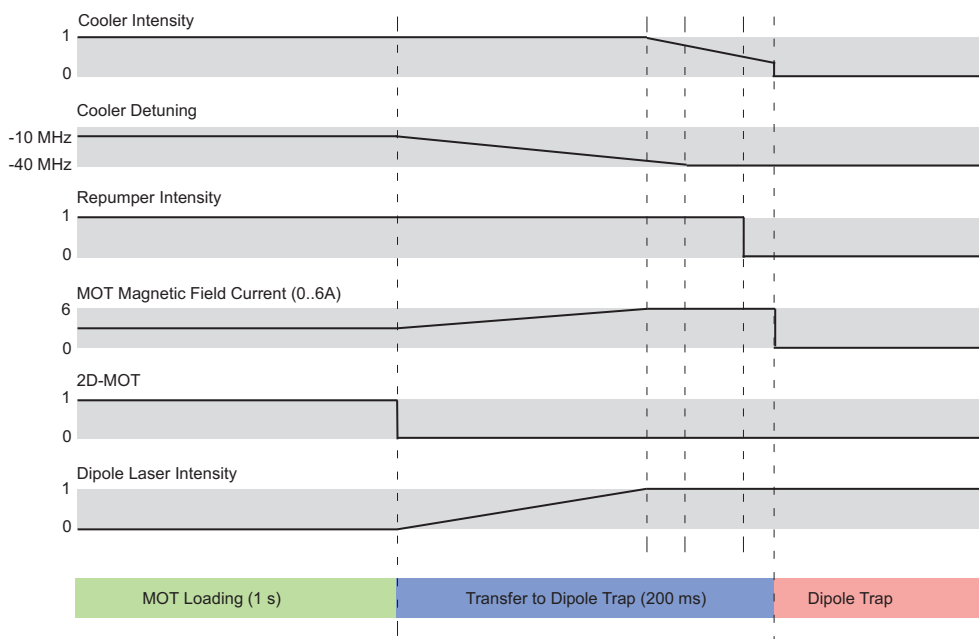
the numerically intensive parts of the control and data acquisition programs.

The software component of the timing system consists of two control programs: (i) a simpler one which is used for every day operation and optimization runs, that use software timing, and (ii) a hardware timed program for measurements where accurate, deterministic timing is required.

The hardware timed program is quite complex, as it involves Matlab scripts for parsing timing files, LabView code to control the I/O boards, and compiled Matlab modules to create the large channel state matrix that is sent to the DAQ boards. The LabView code loads the timing tables and calls a compiled Matlab script to generate the timebase array and channel state matrix which are both stored in RAM. The timebase matrix contains all logic states for each of the 3 timebases at each timestep and can have several million entries. The channel state matrix on the other hand is comparatively small, containing only the update values for all channels. This means only if a change of a logic state or voltage level occurs, not an entry at each timestep. This considerably reduces the amount of data stored in RAM and ensures that all the data can be transferred in time to the DAQ cards⁸. Apart from this, LabView handles the user interface and all communication with the DAQ-boards.

An ASCII-timing file defines durations of events and the associated channel states (logic or analog). Analog channels can be easily ramped which enables smooth transitions between different output levels eg. for continuously changing the frequency of a laser (see figure 9.4). Start and Stop-values are specified for each period and the program then interpolates all val-

⁸Some of the DAQ-cards are available with large onboard memory. In this case the transfer rate of the PC-bus system is not important.



(a) Channel state diagram for some selected analog and digital channels. The example shows the loading and transfer phase of the dipole trap. On the horizontal axis the time is shown (not to scale).

Figure 2.4:

ues between with adjustable resolution. Fully automatized measurement runs are possible by sequential calling of prepared timing files. The overall timing resolution which is equivalent to the duration of the shortest event can be set from $1 \mu\text{s}$ to 1ms and is limited by the DAQ-hardware. When analog channels are read in, the shortest timestep is $10 \mu\text{s}$ (for one channel acquisition). This resolution is sufficient for almost all control and measurement tasks. Whenever measurements require microsecond digital pulses⁹ on only one or two channels, a dedicated pulse generator¹⁰ triggered by a control pulse was used. In this case overall time resolution can be coarse and hence the amount of data processing limited, while still getting sub-microsecond resolution for short pulse sequences. There is no trade-off in precision when the resolution is reduced. Resolution in this case refers to the shortest time an event can last. Synchronization between different events, usually much more important, is precise to about 100ns , as all timebases are derived from a single clock¹¹.

⁹eg. parametric excitation for trap frequency measurements

¹⁰Quantum Composer Inc., Model 9518 digital delay-pulse generator controlled via GPIB

¹¹The limiting factor is the slew-rate of the analog output amplifiers stages in the PCI 6713 card.

3 Cold Atom Production

The production of cold and dense samples of atomic gases offer great benefits for quantum optical studies. The long interaction and coherence times made possible by reduction of the thermal motion are one of the main benefits.

This thesis is ultimately concerned about cooling and trapping of rubidium samples. Trapping refers to confinement of the sample in a small spatial region, whereas cooling refers to a reduction in momentum space.

In this chapter basic physical processes of the laser-cooling and the production of cold rubidium clouds are addressed.

A position dependent force is necessary to confine particles in a spatial region and analogously a velocity dependent force can reduce the velocity spread in momentum space. For laser cooling a velocity dependent force arises through near-resonant scattering of photons on moving atoms.

Each absorption of a photon leads to transfer of one recoil momentum to the atom in direction of the laser light. The associated gain in velocity is $v_{rec} = \frac{\hbar \cdot k}{m}$ with m the mass of the atom and k the wavenumber of the photon. The excited atom decays spontaneously back to the ground state and acquires another recoil. The time averaged momentum over many emissions is zero due to the randomness in the emission direction, whereas the momenta from absorption accumulate. As a result the force on an atom from a single laser beam is the product of the photon momentum times the scattering rate:

$$F_{sc} = \hbar \cdot k \cdot \frac{\Gamma}{2} \cdot \frac{I/I_{sat}}{1 + I/I_{sat} + (2\Delta/\Gamma)^2} \quad (3.0.1)$$

where I is the intensity of the laser beam, I_{sat} is the saturation intensity i.e. the intensity of resonant light at which the atom spends 1/4 of the time in the excited state, Γ is the linewidth of the excited state and $\Delta = \omega_L - \omega_A$ is the detuning between the laser and the atomic transition.

3.1 Doppler Cooling

This is the conceptually simplest laser cooling mechanism created by a velocity dependent force.

The principle is to illuminate an atom from all directions with light tuned slightly below an atomic absorption line. In the reference frame of an atom moving towards the laser beam the light is Doppler shifted closer to resonance, whereas the light in direction of the movement is shifted away from resonance. Thus, the atom predominantly scatters photons from the forward direction and is slowed down. For small velocities ($|k \cdot v| \leq \Gamma$) a friction force results $F_{\text{Dopp}} = -\alpha \cdot v$ which slows the atoms down. A lower limit on the width of the velocity distribution is set by the diffusion resulting from the stochastic nature of the scattering process.

This leads to a final equilibrium temperature T_{Dopp} which is proportional to the ratio of diffusion and friction coefficients (K_B is the Boltzmann constant):

$$T_{\text{Dopp}} = \frac{\hbar \cdot \Gamma}{2 \cdot K_B} \quad (3.1.1)$$

For ^{87}Rb the Doppler-Temperature is $144 \mu\text{K}$, other alkali elements show the same order of magnitude¹.

3.2 Sub-Doppler Cooling

Experimental results of temperatures below the Doppler-limit [6] proved the existence of a cooling mechanisms apart from Doppler cooling. They arise because the underlying assumption of a two-level system and fixed polarizations does not reflect the experimental situation in its full complexity.

The spatially dependent intensity of combined light fields such as a standing wave causes sinusoidally varying light shifts of the atomic energy-levels. A frictional force arises due to the presence of potential-wells where the moving atoms are most likely excited on top of the wells but decay back to the bottom of the potential valleys. The atoms thus move always towards a potential hill and convert kinetic into potential energy. This process was called Sisyphus cooling [7]. Contrary to Doppler cooling, the Sisyphus effect provides cooling when the laser is tuned above resonance ($\Delta > 0$). This mechanism only works for atoms which move from node to an anti-node or less in a natural lifetime ($v \leq \Gamma \cdot \lambda/4$). Therefore the force consists of a broad Doppler contribution causing heating, and a narrow range around $v = 0$ where cooling is provided.

If the atom has not enough kinetic energy left to climb the hills and remains stuck in the potential valley, the Sisyphus process ceases. Thus the final temperature is related to intensity and detuning:

$$K_B \cdot T \approx U_0 \propto \frac{I}{|\Delta|} \quad (3.2.1)$$

¹The proportionality of the Doppler temperature to the natural linewidth Γ suggests the use of narrow-band forbidden transitions in MOTs to achieve colder samples. [64, 65]

This would suggest an equilibrium temperature that can be made arbitrarily low by reducing the intensity or increasing the detuning but a lower limit arises when the recoil energy acquired from spontaneous emission cancels the energy loss from going from the top of the potential hill to the bottom.

$$U_0 \propto E_R = \frac{\hbar^2 k^2}{2m} \quad (3.2.2)$$

$$K_B \cdot T_R = \frac{\hbar^2 k^2}{m} = \frac{\hbar^2}{m\lambda^2} \quad (3.2.3)$$

At this point the atomic de Broglie wavelength is comparable with the laser wavelength so that a localization of the atomic wavepacket to the potential well becomes impossible. A full quantum analysis in 1D predicts a minimum temperature corresponding to a momentum of $\sim 6\hbar k$ [66]

A second mechanism called polarization gradient cooling is based on polarization state dependent optical pumping into nondegenerate magnetic sub-states. Two versions depending on the initial polarization state of the counterpropagating beams are distinguished:

- counterpropagating beams with perpendicular linear polarization: The resulting polarization vector changes periodically from linear through circular to opposite linear over a distance of $\lambda/4$. This leads to periodically varying light shifts of the magnetic sub-states and together with optical pumping to the Sisyphus-effect described before.
- counterpropagating beams with opposite circular polarization: This process is different and no Sisyphus effect occurs. In this case the resulting polarization vector is linear everywhere but rotates around the beam axis with a pitch of $\lambda/2$. For a moving atom, where initially all sub-levels are equally populated, the changing direction of the electric field causes a redistribution of population between the magnetic-substates. This motion-induced symmetry breaking between the atom-light interaction enhances the difference between the photon scattering rates and leads to a strong frictional force [8].

For a 3D-optical molasses², composed of 3 orthogonal pairs of counterpropagating beams as it is found in a MOT, the polarization vector is linear everywhere but the orientation is strongly position dependent. The six beams form an intensity lattice in space with a set of zero intensity points.

Optical Molasses provide cooling but not a spatial confinement. More precisely, the averaged force acting on the atoms is only a velocity dependent, strongly dissipative force.

3.3 The Magneto-Optical-Trap

Magneto-Optical-Traps are by far the most widely used type of trap to produce cold, neutral atoms clouds. Reasons for this are the relative simplicity of the experimental setup,

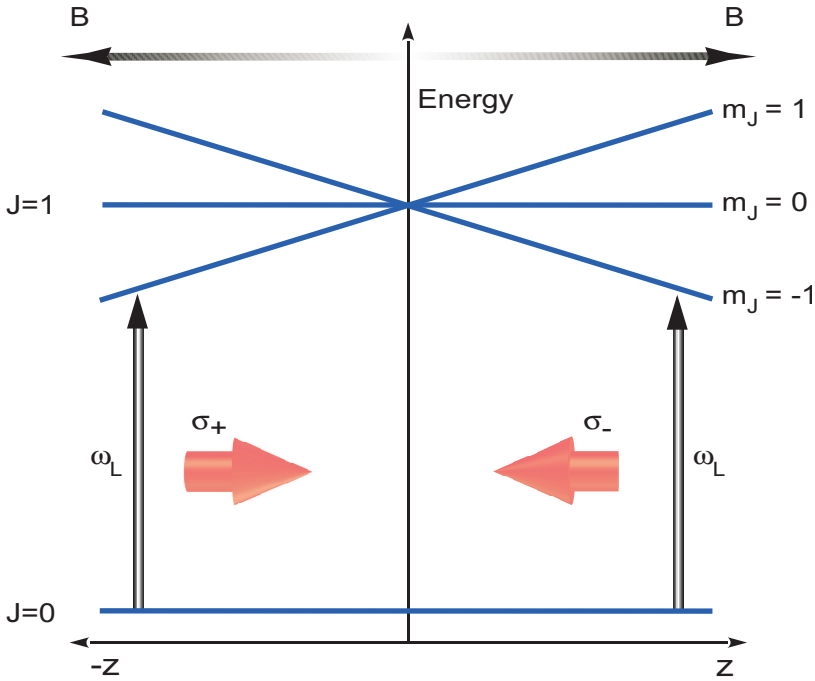
²A optical molasses is a pair of counterpropagating laser beams detuned below the atomic resonance which provide a velocity dependent damping force parallel to the beam direction. The force results in viscous damping but does not provide confinement in contrast to the magneto-optical trap.

the ability to trap atoms from a room-temperature thermal background and the fact that the confinement process provides cooling at the same time.

Starting from a 3-dimensional optical molasses, the principle of compensated scattering forces was extended by the use of a magnetic quadrupole-field. The magnetic field Zeeman-shifts the energy levels into resonance with a beam which pushes the atoms back to the origin from all sides.

We consider for simplicity a $J = 0 \rightarrow J = 1$ transition. The magnetic field produced by 2 coils in anti-Helmholtz configuration increases linearly from $z=0$ at the trap-center outwards ($B(z) = \beta z$). Proportional to the magnetic field strength the Zeeman shift causes a perturbation of the magnetic sub-levels with $m_J = 0, \pm 1$.

The resulting frequency shift for a transition from $|F, m_F\rangle$ to $|F', m_{F'}\rangle$ is then



(a) Shift of the magnetic sub-states inside a magneto-optical trap

Figure 3.1:

$$\Delta_B = (g_{F'} m_{F'} - g_F m_F) \cdot \frac{\mu_B |B|}{h} \quad (3.3.1)$$

where μ_B is the Bohr magneton, m_F the magnetic quantum number and g_F the Landè g-factor:

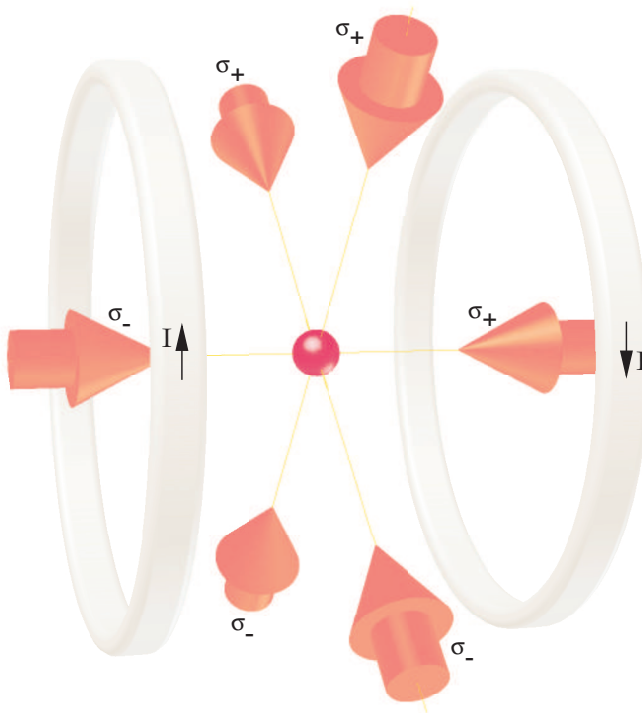
$$g_F = \frac{F(F+1) + J(J+1) - I(I+1)}{2F(F+1)} \cdot g_J \quad (3.3.2)$$

Figure 3.1 shows a pair of red detuned, counterpropagating laser beams, both right-hand circularly polarized. For cooling the laser beams are detuned below the unshifted reso-

nance ($\Delta > 0$). The beam in direction of the quantization axis (along z) drives σ_+ -transitions with $\Delta m_F = +1$ in the atom. On the other hand the beam going in direction $-z$ against the quantization axis excites σ_- -transitions with $\Delta m_F = -1$. If the atoms move away from the trap-center the sublevel which interact with the beam pointing towards the center gets closer to resonance. This leads to an imbalance in radiation pressure and to a force on the atoms towards the center exerted by the MOT beams. Thus, in addition to the frictional term, the atom experiences a restoring force $F = -\kappa z$. In the limit of small Zeeman shifts and small velocities the expression for the force on an atom inside a MOT can be written as

$$F_{\text{MOT}} = -\alpha \cdot v - \kappa \cdot z, \quad (3.3.3)$$

with α and κ denoting the damping and spring constant [11].



(a) Standard beam configuration for a 3D-MOT

Figure 3.2:

A two dimensional magneto-optic trap can be made by two pairs of counterpropagating beams and a linear quadrupole magnetic field which is constant along the 3rd orthogonal axis. The atoms are cooled and confined in two dimensions, and when loaded from background vapour, a constant beam of cold atoms is produced.

3.4 Experimental Setup

In this section the actual setup is described which generates a cold atomic beam from rubidium vapor inside the upper part of the vacuum chamber, and the transfer and storage of this beam to the lower UHV-part of the apparatus.

Detailed information about this setup can be found in the thesis of Matthias Schulz [60]. Here are mostly the changes described which were made to improve the previous setup.

3.4.1 The Main Apparatus

The main setup of the experiment consists of a double-MOT system with two superimposed crossed, far detuned dipole traps.

In the 2-dimensional MOT a cold beam of rubidium is produced which is transferred through a differential pumping stage to the lower, conventional MOT. With this arrangement, atoms can be quickly captured from background vapor in the 2d-MOT while maintaining a high loading rate into the 3d-MOT systems and keeping the background pressure below 10^{-10} mbar. A schematic of the optics setup is shown in figure 3.3.

The central part of the experiment consist of 2 fused silica glass cells mounted on a stainless steel vacuum vessel which contains the differential pumping stage and is connected to 2 ion-getter pumps³. Inside the lower part a 3d-MOT made of 6 counterpropagating beams collects the atoms from the cold rubidium beam.

Both beams constituting the dipole traps are placed in a horizontal plane intersecting the 3d-MOT center. Laser light generated by a Yb:YAG solid state laser⁴ is transported through photonic crystal fibers⁵ to the experiment. Beams diverging from the fiber-exits are first collimated and then focused into the trap center. Fluorescence light is collected by homemade high-aperture objectives and imaged onto a ccd-camera or calibrated photo diode. The high power laser light is separated from the fluorescence light by dichroic filters. As a second function the objective which focuses one of the dipole-beams is used to image the spatially filtered fluorescence light to a cooled photomultiplier.

The glass-cell design allows easy optical access which is a key requirement for multiple-beam, all-optical traps. In vertical direction, a pushing beam from the top and a detection beam from the bottom are passing along the atomic beam axis. Access for a probe beam for the future spin squeezing experiments is provided by a dichroic beam splitter.

All beams are delivered by optical single-mode fibers. This avoids long beam paths and eases stray-light shielding as well as guarantees clean gaussian mode profiles.

3.4.2 The 2-D MOT System

The cooler beam, delivered by an optical single-mode fiber, is first expanded to a beam diameter of 16 mm, collimated and then split in 2 fractions by a polarizing beam splitter (PBS).

³Leybold 30 l/s and Varian Star Cell 60 l/s

⁴VersaDisk-1030 from ELS Elektronik Laser System GmbH, Germany

⁵LMA-25 from Crystal Fibre A/S, Denmark

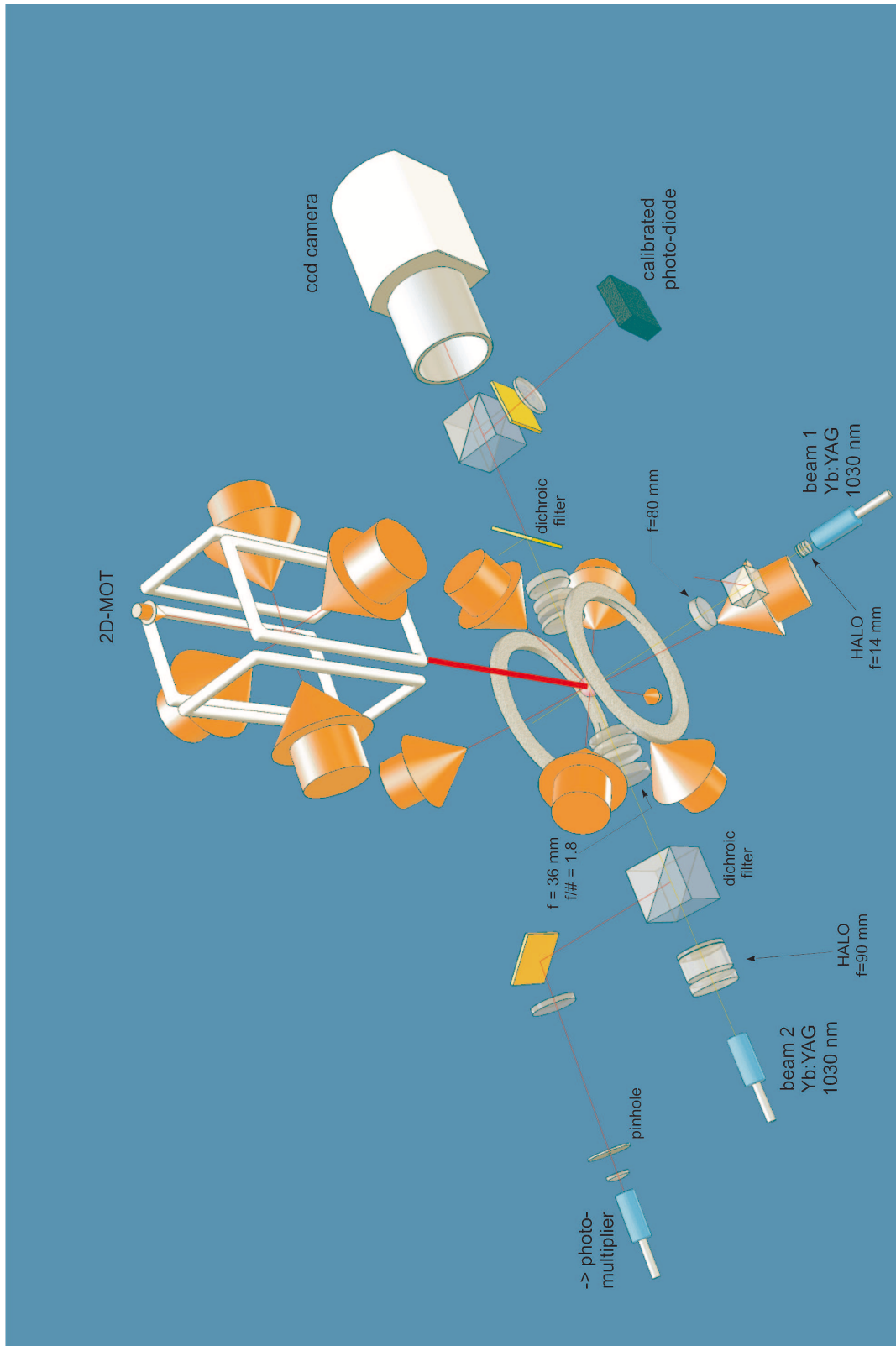
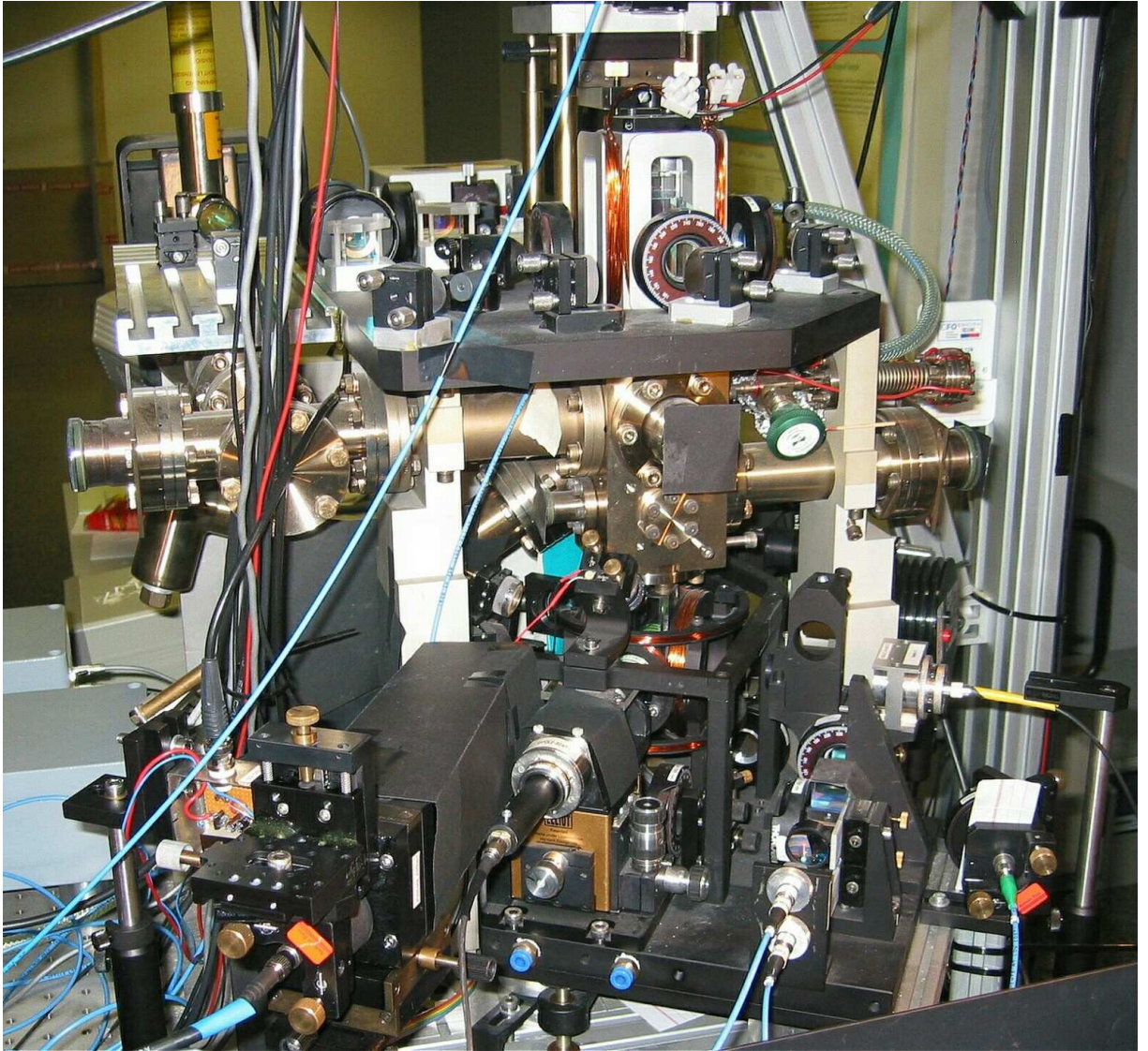
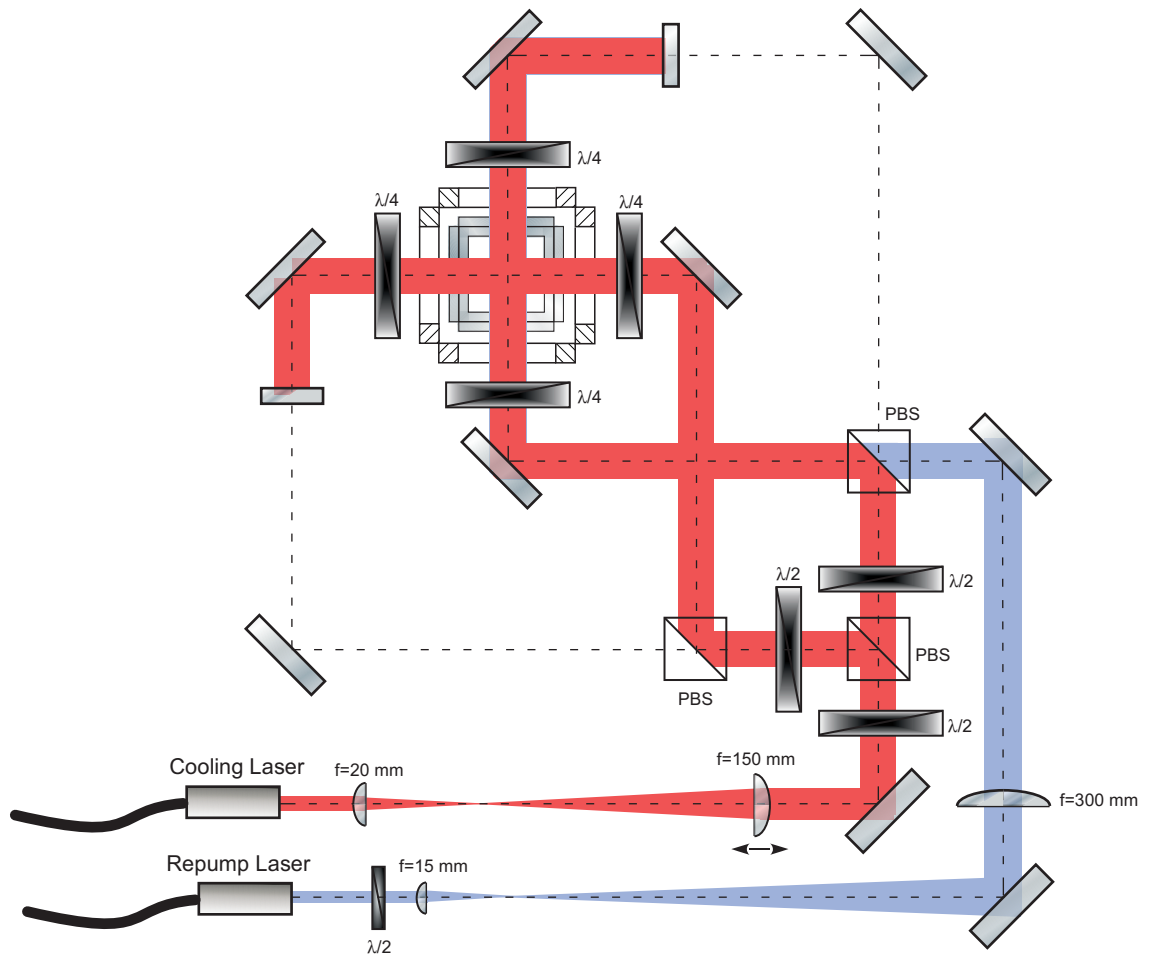


Figure 3.3:



(a) Photo of the trapping assembly.

Figure 3.4:



(a) Scheme of the optical elements of the 2D-MOT setup. The cooler laser path is red colored, the repump laser path light-blue.

Figure 3.5:

Both beams pass quarter-wave-plates to get the desired circular polarization before they cross the cell. After cell transmission both beams are back-reflected so that they counterpropagate. A second quarter-waveplate, which is passed twice acts as a half-waveplate and changes the polarization to the opposite circular state.

Originally this setup was built for 4 independent counterpropagating beams without backreflection which allowed a more balanced adjustment of the individual beam intensities at the expense of lower power.

For backreflection geometries, all beams passing the cell are recycled so that the total optical power required to saturate the cooling transition is reduced by a factor of 2. In our experiments the advantage of having more optical power available which increases the loading rate was preferred. Combined beam power was up to 20 mW which translates into an intensity of 5 mW/cm^2 or about 2 times saturation intensity⁶.

The repumper beam, also originating from a single-mode fiber is expanded to the same beam diameter as the cooler beam and overlapped with one of the cooler beams on a free port of a PBS.

6

- $I_{Sat}^{87\text{Rb}}(F = 2 \rightarrow F' = 3) = 3.576 \text{ mW/cm}^2$ for unpolarized atoms
- $I_{Sat}^{87\text{Rb}}(F = 2, m_F = 2 \rightarrow F' = 3, m_{F'} = 3) = 1.669 \text{ mW/cm}^2$ for the cycling transition

3.5 Atom detection

Atom detection in our experiment is based on the quantitative measurement of fluorescence light emitted by excited atoms. Three different detection devices are in use:

1. A triggerable ccd-camera provides spatial and temporal information of the fluorescence light intensity and serves to image the atom cloud
2. A calibrated photo-diode (PD) is used to determine the atom number
3. Low light levels are detected with a photomultiplier system (PMT)

An overview over the detection channels is shown in figure 3.3. Information about the CCD-camera system can be found in 2.1 and the photo-multiplier system is described in ??

3.5.1 The Photo-Diode

Fluorescence light detection of atoms in a magneto-optical trap is theoretically quite complicated. Moving atoms are subjected to rapid changes of the polarization direction and intensity of the trapping light. A simplification to estimate the scattering rate can be made by averaging over the different polarization directions assuming isotropic pump light. Any contribution from the $F = 1 \rightarrow F' = 2$ repump transition is neglected.

In the case of dipole-trapped atoms the polarization vector of the dipole light defines a quantization axis. Together with optical pumping into specific magnetic sub-states, optimized detection geometries can be exploited.

Assuming an isotropic emission pattern, the fraction of fluorescence light detected by an optical system is simply the covered solid angle multiplied by the detection efficiency.

The solid angle is calculated as follows:

Imaging objective: $f/\# = 1.8$	
clear aperture:	23.0 mm
distance of entrance aperture to focal point:	33.5 mm
fraction of collected light:	$\frac{(23\text{mm})^2 * \pi}{4 * 4 * \pi * (33.5\text{mm})^2} = 0.027$

The measured losses in the optical system are:

element	number of elements in beam path	total transmission
silica cell	1	0.96
4-lens objective	1	0.965
dichroic filter	2	0.9025
polarizing cube	1	0.5
focusing lens	1	0.99
interference filter	1	0.80
total transmission		0.331

For a saturation intensity of 3.58 mW/cm^2 ($F = 2 \rightarrow F' = 3$ cycling transition) the scatter-

ing rate⁷ calculates to:

$$R_{Sc} = \frac{\Gamma}{2} \cdot \frac{6 * I_0 / I_{Sat}}{1 + 4(\frac{\Gamma}{\Delta})^2 + 6 * I_0 / I_{Sat}} \quad (3.5.1)$$

The natural line width Γ of the $5^2S_{1/2} \rightarrow 5^2P_{3/2}$ dipole transition is $2\pi \cdot 6.065$ MHz (FWHM). Intensity of the MOT beams during experiments is set to $I_0 = 0.7 * I_{Sat}$, detuning Δ during the MOT loading phase is 10 MHz and reduced to 3 MHz for recapture⁸ measurements.

$$R_{Sc} = \frac{\Gamma}{2} * 0.667 = 1.25 \cdot 10^7 \text{ photons/s/atom} \quad \text{for } \Delta = 3 \text{ MHz}$$

$$R_{Sc} = \frac{\Gamma}{2} * 0.257 = 4.84 \cdot 10^6 \text{ photons/s/atom} \quad \text{for } \Delta = 10 \text{ MHz}$$

The optical power equivalent to a photon flux of 1 photon/s at 780 nm is $2.55 \cdot 10^{-19}$ W.

$$\text{scattered power/atom} = 3.18 \cdot 10^{-12} \text{ W/atom} \quad \text{for } \Delta = 3 \text{ MHz}$$

$$\text{scattered power/atom} = 1.23 \cdot 10^{-12} \text{ W/atom} \quad \text{for } \Delta = 10 \text{ MHz}$$

The responsivity of the photo diode (Thorlabs DET110) is $\eta = 0.5$ A/W at 780 nm. Resulting photo-currents are:

$$I_{PD} = 0.5 \text{ A/W} * 3.18 \cdot 10^{-12} \text{ W/atom} = 1.59 \text{ pA/atom} \quad \text{for } \Delta = 3 \text{ MHz}$$

$$I_{PD} = 0.5 \text{ A/W} * 3.18 \cdot 10^{-12} \text{ W/atom} = 0.617 \text{ pA/atom} \quad \text{for } \Delta = 10 \text{ MHz}$$

Measured on the oscilloscope⁹ with 10 M Ω input impedance the photo voltage calculates to:

$$U_{PD} = 1.59 \mu\text{V/atom} \quad \text{for } \Delta = 3 \text{ MHz}$$

$$U_{PD} = 0.617 \mu\text{V/atom} \quad \text{for } \Delta = 10 \text{ MHz}$$

Taking into account the transmission of all optical elements and the fraction of light collected by the imaging optics¹⁰, the calibrated photo voltage is:

$$\begin{aligned} U_{PD} &= 14.2 \text{ nV/atom} \quad \Delta = 3 \text{ MHz and } I/I_{Sat} = 0.7 \\ U_{PD} &= 5.5 \text{ nV/atom} \quad \Delta = 10 \text{ MHz and } I/I_{Sat} = 0.7 \end{aligned} \quad (3.5.2)$$

⁷this expression is valid for illumination with 6 beams as it is during normal MOT operation, I_0 refers to the single beam intensity

⁸atoms are transferred from the MOT into the dipole trap for some variable time and then recaptured back into the MOT during which fluorescence is detected

⁹Tektronix 3200B

¹⁰ $\eta_{total} = T * \eta = 0.331 * 0.027 = 8.93 \cdot 10^{-3}$

For computer controlled measurements, data acquisition is more conveniently done by the analog input board¹¹. First a home built low noise transimpedance amplifier was connected close to the photo diode which converts the photo-current to a voltage. Input impedance was measured to be 1.025 M Ω .

The low level photo-voltage is then further amplified by a offset-drift compensated variable-gain voltage amplifier¹². The switchable gain amplifier provides a large dynamic range for the measurements and keeps the signal level high enough for optimal A/D conversion conditions.

The voltage multiplication factors of the amplifier gain stages can be calculated according to the formula

$$U_{out} = U_{in} \cdot 10^{\left(\frac{Gain}{20}\right)} \quad (3.5.3)$$

where the gain value is in dB. For our measurements the 20 dB gain setting was used which results in a voltage multiplication factor of 10.

The final calibration values for the photo-diode measured with the FEMTO amplifier and the analog-input board gives:

$$\begin{aligned} U_{PD} &= 14.6 \text{ nV/atom} \quad \text{at } \Delta = 3 \text{ MHz and } I/I_{Sat} = 0.7 \\ U_{PD} &= 5.6 \text{ nV/atom} \quad \text{at } \Delta = 10 \text{ MHz and } I/I_{Sat} = 0.7 \end{aligned} \quad (3.5.4)$$

3.6 Loading of the 3D-MOT

Fast production of cold and dense samples of atoms is a key requirement for many atom optics experiments. High loading rates, although not of essence for small atom number experiments, provide quick turnaround times when running sequences, eg. for parameter optimization. An efficient method is the generation a cold atomic beam from a 2D-MOT system which loads a conventional MOT [69, 70].

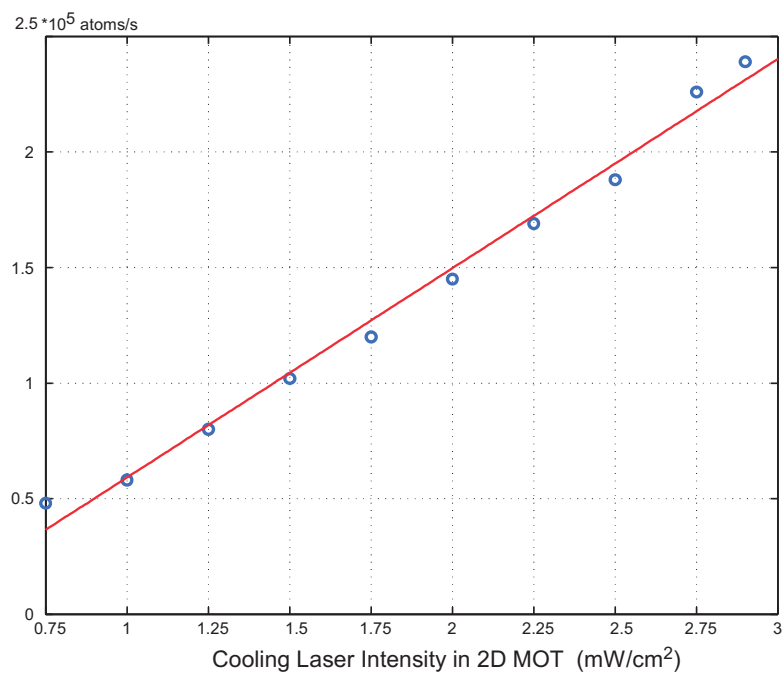
In previous work, a system with limited laser power was used, where the cooling laser was shared between the 2D and 3D-MOT [60] Here we implement a master-slave diode laser system, where the full undivided power of the slave laser (25 mW after the optical fiber) is available as cooling light for the 2D-MOT, resulting in 2 times saturation intensity. Optical power is important as the 3D-MOT loading rate is proportional to the 2D-MOT beam intensity up to several times saturation intensity. In our setup the loading rate is still limited by available cooling laser power which can be seen from the measurement in fig.3.6

To quantitatively describe the dynamics of loading and loss processes in a magneto-optical trap a common rate equation model can be used:

$$\frac{dN}{dt} = L_0 - \gamma \cdot N - b_0 \cdot N^2 \quad (3.6.1)$$

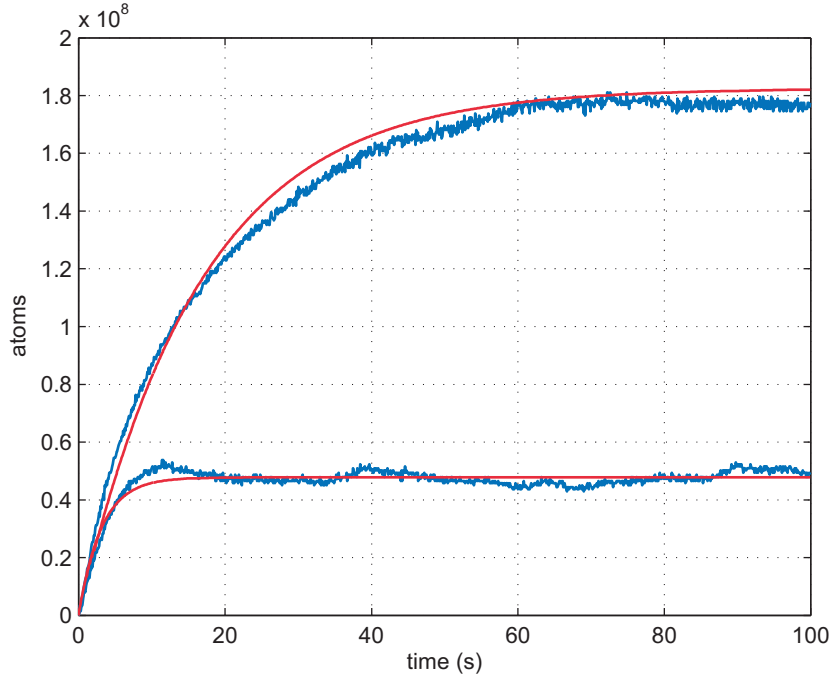
¹¹National Instruments AT-MIO-DE-10

¹²FEMTO DHPVA-100



(a) Dependence of the 3D-MOT loading rate on the 2D-MOT beam Intensity

Figure 3.6:



(a) Loading of the 3D-MOT with and without dipole light present.

Figure 3.7:

Here L_0 is the loading rate from the 2D-MOT, γ the atom loss coefficient due to collisions with the hot background atoms and the last contribution b_0 ¹³ comes from collisions between cold atoms. This leads to a density dependence in the MOT-population decay.

The solution to the equation above is [68]:

$$N(t) = \frac{k}{2b_0} \cdot \left[\tanh \left(\frac{1}{2} \cdot k \cdot t - \frac{1}{2} \cdot \ln \left(\frac{\gamma - k}{\gamma + k} \right) \right) - \frac{\gamma}{k} \right]$$

$$k := \sqrt{4L_0b_0 + \gamma^2}$$

with the final steady state number N_0 given by:

$$N_0 = \frac{\sqrt{4L_0b_0 + \gamma^2} - \gamma}{2b_0} \quad (3.6.2)$$

¹³In the low-density MOT-regime, the atom density distribution is Gaussian: $n(r,t) = n_0(t) \cdot e^{-(r^2/\omega^2)}$. In this case the atom number dependent loss constant b_0 in equation 3.6.2 can be related to the density dependent dipolar loss coefficient β via $b_0 = \frac{\beta}{(2\pi)^{3/2}\omega^3}$ [68].

Figure 3.7 shows the loading behavior of the 3D-MOT from the cold atom beam without the presence of the dipole light (upper curve) and with 5W of dipole light (lower curve). The disturbance of the MOT-cooling processes by the large light induced level-shifts can be seen clearly from the difference in the steady state atom numbers. In case where the dipole light is on, measured steady state numbers underestimate atom numbers in the MOT. Atoms in the region of the dipole light are shifted out of resonance and therefore not detected. The volume of the dipole trap is however much smaller than the MOT-volume so that the unaccounted atom number is $\max.10^6$. The graph shows that the initial loading rate¹⁴ is not affected by the dipole light but the loss rate is several times higher.

The table below shows the loss rate, loading rate and steady state atom number estimated from a fit¹⁵ to the data shown in figure 3.7:

$$\begin{array}{ll} \gamma = 0.06 s^{-1} & \gamma = 0.32 s^{-1} \\ L_0 = 1.2 \cdot 10^7 \text{ atoms/s} & L_0 = 1.5 \cdot 10^7 \text{ atoms/s} \\ N_{SS} = 2 \cdot 10^8 \text{ atoms} & N_{SS} = 5 \cdot 10^7 \text{ atoms} \end{array}$$

Standard operating parameters are:

3D-MOT: magnetic field gradient of 18 G/cm, detuning $\Delta = 4.5$ MHz and beam intensity of 1.1 mW/cm^2

2D-MOT: magnetic field gradient of 10 G/cm, detuning $\Delta = 10$ MHz and beam intensity of 4.5 mW/cm^2

The overall loading efficiency improved by a factor of 30 from the previous setup mainly by the higher power available from the slave laser system and the addition of a 1 mm diameter pushing beam along the 2D-MOT axis. For optimal loading results the pushing beam power was set to $110 \mu\text{W}$ and adjusted in a way that it passes through the differential pumping stage aperture ($d=2$ mm) but misses the atom cloud of the 3D-MOT.

With the atom loss rate it is possible to get an estimation of the background pressure in the lower cell. Since no pressure measurement device has been installed inside the vacuum apparatus and the current readings from the ion-getter pumps are unreliable in the UHV region, there is no other method available to determine the pressure.

A theoretical model developed by S. Bali et al. [72] predicts the loss rate from collisions of room-temperature He atoms¹⁶ with cold ^{87}Rb atoms to be $\gamma_c/n_p = 2.3 \cdot 10^{-9} \text{ cm}^3/\text{s}$. From this a background gas density of $n_p = 2.6 \cdot 10^7 \text{ atoms/cm}^3$ is inferred. The residual background gas pressure then calculates to:

$$p = n_p \cdot K_B \cdot T = 1 \cdot 10^{-9} \text{ mbar} \equiv 8.1 \cdot 10^{-10} \text{ torr} \quad (3.6.3)$$

An independent estimation of the background pressure based on a semiempirical scattering model [114] gives a slightly lower value of $9 \cdot 10^{-10} \text{ mbar}$.

¹⁴The slightly higher value of the loading rate is not a systematic effect

¹⁵The fit of equation 3.6.2 to the data points without quadratic term is good and shows that this term is negligibly small.

¹⁶At UHV conditions He is one of the main residual components together with H_2 . H_2 which has a higher collisional cross section would lead to a lower background pressure for the measured lifetime. The stated value is therefore a upper limit to the pressure.

Compared to the upper cell, where atom density is determined by the Rb vapor pressure at room temperature ($3 \cdot 10^{-7}$ mbar), the differential pumping stage maintains a pressure difference factor of ≈ 300 .

From the steady state atom number also the maximum capture velocity of the 3D-MOT can be calculated [71]. Atoms which are faster can not be trapped by the light forces. In our case the maximal capture velocity is 18 m/s. This value is consistent with loading rate measurements carried out by other groups [74, 75] where it was shown that with higher capture velocities (larger size of the light fields) loading rates increase significantly¹⁷.

3.7 Temperature and Density

For proper loading efficiency into the dipole trap the atoms have to be prepared sufficiently cold. Although with standard MOT operation procedures sub-Doppler temperatures are readily obtained, knowledge of the sample temperature and density is helpful for optimizing the loading process into the dipole trap.

For exactly counterpropagating trapping beams the atom cloud is elliptical due to the factor of 2 between the magnetic field gradient in axial (z) and radial (x,y) direction of the MOT coils. The analysis of Townsend et al. [78] showed that for small atom numbers, where the MOT operates in the temperature limited regime, the cloud radii are related to the sample temperature via the equipartition theorem:

$$\frac{1}{2} \kappa_{ii} r_i^2 = \frac{1}{2} K_B T \quad (3.7.1)$$

Here κ_{ii} denotes the spring constant tensor which is proportional to the magnetic field gradient ($\kappa \equiv 2\kappa_{xx} = 2\kappa_{yy} = \kappa_z$), r_i is the cloud radius along the axis $i = \{x, y, z\}$, K_B is the Boltzmann constant and T the sample temperature.

If the temperature is isotropic then the density distribution $n(r)$ has to obey Eq. [76, 77]:

$$K_B T \cdot \nabla[\ln n(r)] = F_{total}, \quad (3.7.2)$$

where F_{total} is the sum of all spatially dependent forces acting on the atoms. According to the Walker-Sesko-Wieman (WSW) model [115] the total force can be expressed as $F_{total} = F_{spring} + F_{absorption} + F_{reradiation}$.

If only the conservative contributions $F_{spring} + F_{reradiation}$ are considered, spherically symmetric solutions to eq. 3.7.2 can be constructed. But no physically reasonable solution can be found when the nonconservative absorptive force is included as for most density distributions $\nabla \times F_{absorption} \neq 0$ ¹⁸.

¹⁷An atomic flux of 10^{10} atoms/s can be produced but with atomic velocities up to 100 m/s and the mean velocity centered around 40 m/s.

¹⁸If an absorptive contribution to the force is included the constant temperature approximation breaks down. Reabsorption of multiple scattered photons lead to increased momentum diffusion which causes an atom number dependent temperature $T \sim N^{1/3}$ [79].

In the simplified case where $F_{total} = -\kappa_{ii}r_i$, Eq. 3.7.2 leads to a Gaussian density distribution

$$n(r_i) = n_{max} \cdot e^{-\left(\frac{\kappa_{ii}^2 r_i^2}{2K_B T}\right)} \quad (3.7.3)$$

A time-of-flight method first applied by Lett et al. [75] was chosen for temperature measurements. Here the trapped atoms are released and allowed to expand freely. After variable time delay they are resonantly illuminated and imaged onto a CCD-camera. The density distribution of the expanding cloud translates into an intensity distribution on the CCD-camera and a 1-dimensional Gaussian¹⁹ is fitted to the data²⁰. By comparison with a Maxwell-Boltzmann velocity distribution the temperature is obtained.

$$g(x) = \frac{1}{\sqrt{2\pi\sigma_x^2}} e^{-\left(\frac{x^2}{2\sigma_x^2}\right)} \quad (3.7.4)$$

$$f(v) = \frac{1}{\sqrt{2\pi}v_{rms}} e^{-\left(\frac{mv^2}{2v_{rms}^2}\right)} \quad v_{rms} = \sqrt{K_B T/m} \quad (3.7.5)$$

and with

$$x_{final} = x_0 + v_{rms} \cdot t \quad (3.7.6)$$

follows that

$$\sigma_x^2(t) = \sigma_x^2(0) + \frac{K_B T}{m} t^2 \quad (3.7.7)$$

Rearranging the last Eq. for the temperature gives

$$T = \frac{m}{K_B} \left[\frac{\sigma_x^2(t_{final}) - \sigma_x^2(t_{initial})}{t_{final}^2 - t_{initial}^2} \right] \quad (3.7.8)$$

For the fit the initial cloud extension $\sigma_x(0)$ and the temperature T are adjusted.

With the determination of the initial atom number N from the photo-diode signal and the volume V of the cloud

$$V = \pi^{3/2} \sigma_x \sigma_y \sigma_z \quad (3.7.9)$$

the maximum number density $n = N/V$ can be estimated.

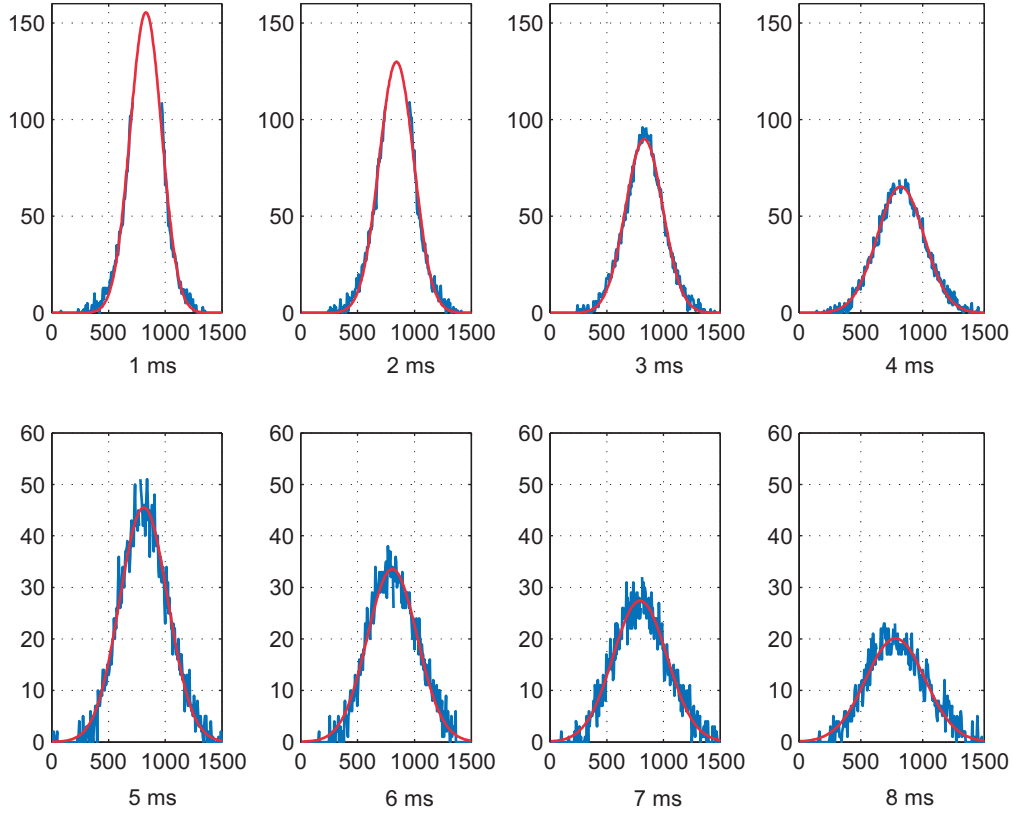
Figure 3.9 shows a temperature estimation fit from measured data points. The temperature of the sample $19 \pm 1.5 \mu K$ is one order of magnitude below the Doppler temperature of $144 \mu K$ and at the lower limit of what can be reached in a rubidium MOT. Measured number densities are in the range of several 10^{10} atoms/cm³.

A way to achieve optimal loading conditions for the 3D-MOT is to align the system so that an optical molasses [75] can be sustained. This requires careful beam alignment and compensation of residual magnetic fields. With such an optimized MOT system large atom clouds can be trapped.

Figure 3.10 shows a 1d-density profile of a large atom cloud. Operating parameters were

¹⁹A 2-dimensional Gaussian fit confirmed the results of the 1-d fit

²⁰The data represent a 1 dimensional intensity profile along the horizontal z-axis.



(a) Single shot atom density profiles after ballistic expansion for several expansion times.

Figure 3.8:

$\Delta = -20$ MHz, $\frac{I}{I_{Sat}} = 1.7$ and $\frac{dB}{dz} = 0.25$ Gauss/cm. For the stated parameters, a cloud with more than $N = 2 \cdot 10^6$ atoms is affected by radiation trapping which gradually changes the density profile from Gaussian to top-hat for increasing atom numbers [76].

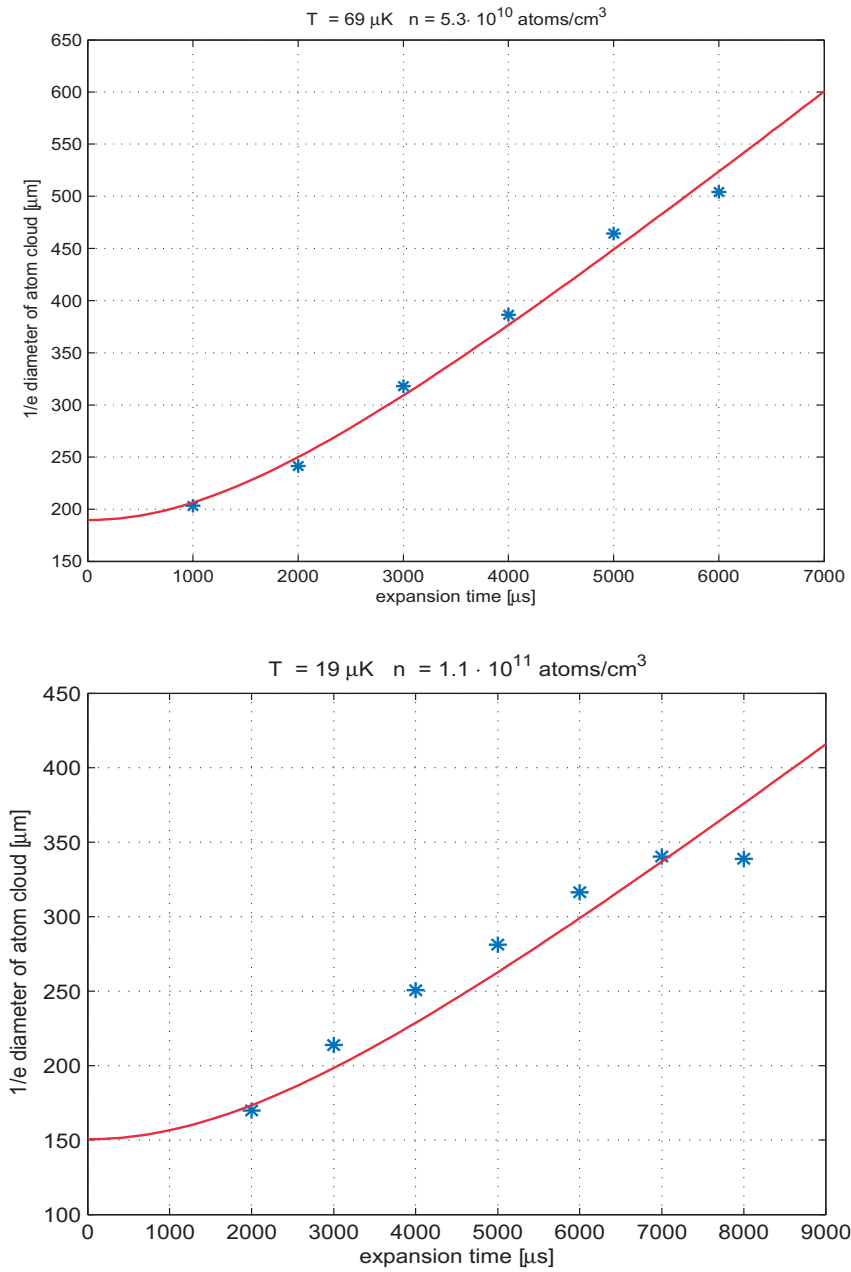
The measured MOT-intensity distribution²¹ was fitted to a top-hat profile [80] which is indicative for large, density limited atom clouds [81].

$$n(r) = n_{max} \cdot \frac{1}{1 + e^{(r-r_c)/r_T}} \quad (3.7.10)$$

Typically for a MOT the maximum density n_{max} is limited by radiation trapping to $n_{max} \leq 10^{11}$ atoms/cm³. Here r_c denotes the radius where the density reduces to half the maximum density and r_T is the distance range over which the density decreases to $\frac{n_{max}}{e}$. With the half-width radius of $r_c = 2.3$ mm from the fit and a maximum density of $5 \cdot 10^{10}$ atoms/cm³ the total atom number is roughly $2 \cdot 10^9$ atoms²².

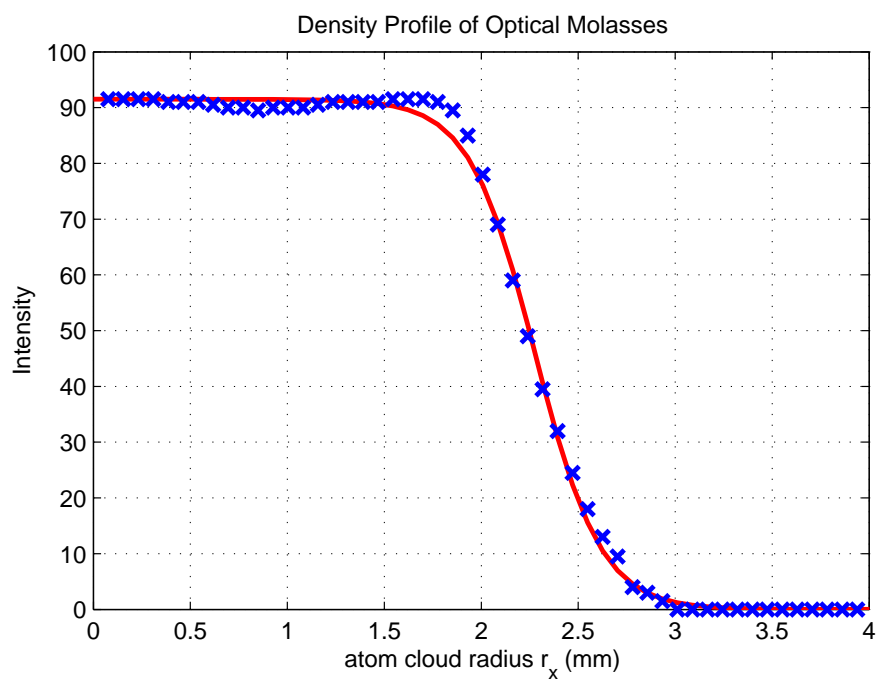
²¹This intensity distribution is a projection onto the x-direction.

²²If the cloud is approximated as an isotropic sphere with radius r_C and constant density



(a) Typical Temperature fit (top) and a fit showing a temperature close to the lower limit for a Rb-MOT cloud (bottom)

Figure 3.9:



(a) Top-hat density profile fitted to a large MOT cloud. The estimated cloud diameter is 4.6 mm and the number of trapped atoms is roughly $2 \cdot 10^9$.

Figure 3.10:

4 Optical Dipole Trapping

With the great advances in the field of laser cooling in the last 30 years, the ultralow temperature region became experimentally accessible. The first relevant progress was achieved with trapped, charged particles [4, 5]. The strong Coulomb forces acting on ions in an electric or electromagnetic field makes it possible to reliably store them. Ion traps laid the basis for many highlights in quantum optics eg. single trapped ions [34], ground state cooling [22], precision spectroscopy [35], time- and frequency standards [36], crystalline ordered states and quantum information processing [38–40]. Many methods first pursued with ion traps were later adapted for trapped neutral atoms. Among the peculiar advantages of charged-particle traps is a confining potential which is independent of the internal atomic state., This makes them universally suitable for a large range of experiments and which opens the possibility to confine ions to regions below one optical wavelength. Combined with a state detection efficiency close to 100% [41] , these systems represents formidable tools for fundamental investigations.

For neutral atoms the interaction mechanisms are weaker. Trapping requires substantial cooling of the atomic sample and often the trapping mechanism is connected with the cooling process, like in a magneto-optical trap.??

Three different interactions may be used for trapping neutral atoms, each one offering specific advantages:

- Magnetic traps rely on the state-dependent interaction between an atom with magnetic moment and an inhomogeneous magnetic field. No light forces are involved in the process, thus avoiding limitations caused by unwanted optical excitation, optical heating or light-assisted collisions. These advantages made magnetic traps the preferred tool for storing ultracold, degenerate quantum gases. The main disadvantage is the state dependency of the confining force, restricting severely the combination of trapping and internal dynamics. Apart from this, the necessity of bulky coil assemblies is limiting optical access to the trapped sample.
- Traps using the optical scattering force of near resonant light are the most ubiquitous. The strong dissipative damping forces of slightly detuned laser light are able to capture atoms from a thermal background without any pre-cooling. The attainable trap depths of a few Kelvin allow for reliable storage of atomic samples. (See chapter 4.) In these traps, however, atomic densities and temperatures are limited by the presence of the near resonant radiation. With strong dissipation and highly perturbed internal dynamics any possibility of coherent control of internal atomic states is ruled out.

- Optical dipole traps show the weakest interaction so far discussed. Confinement depends on the interaction between an atomic multipole moment and an inhomogeneous electromagnetic field. The typical trap depths are much shallower compared with traps relying on the scattering force. This requires a sufficiently cold sample for capturing. In most of the cases, atoms are loaded from a magneto-optical trap where they are cooled down to the μK regime. Due to the far detuning ($|\Delta| \sim 10^7 \cdot \Gamma$) of the trapping light optical excitation and hence dissipation can be very low, providing an almost conservative trapping potential.

All light-induced processes present in radiation force traps eg. photo association, optical heating, radiative escape and light assisted collisions are strongly reduced. Furthermore it is possible to have a state independent trapping potential, allowing coherent manipulation as well as taking advantage of the full set of internal states.

Light fields can be structured with great flexibility, thus allowing for the the implementation of more complicated trap geometries. Multiple-well potentials and optical lattices can be realized, which are ideally suited for quantum information purposes [20, 42].

Any trapping process implies the conservation of energy, dictating that kinetic energy has to be exchanged with potential (internal) energy. This results in a position dependent shift of the atomic levels inside the trap, considerably complicating interpretations of spectroscopic measurements. For real atoms one also has to take into account the large number of atomic states [44] affected and the time dependency of the level shifts caused by the atomic motion inside the trap.

4.1 The Dipole Potential

This section gives a description of the physical concepts of atom trapping with far detuned laser light. The first part treats the atom and light fields classically, leading to an intuitive picture of the dipole interaction. A quantum mechanical description including dressed states [43] complements the sub-section.

4.1.1 The classical point of view

Unlike permanent magnetic dipole moments of atoms used for magnetic trapping, permanent electric dipole moments are forbidden by the inversion symmetry requirement of atomic wave functions.¹ However induced dipole moments, produced by mixing states with opposite parity, can be used.

An oscillating electric field $\mathbf{E}(\mathbf{r}, t) = \boldsymbol{\varepsilon} \cdot \mathbf{E}(\mathbf{r}) \cdot e^{-i\omega_L t} + c.c$ induces an atomic dipole moment

¹The operation of inversion leaves the Hamiltonian of a particle in a centrally symmetric field $\mathcal{H} = \frac{p^2}{2m} + U(r)$ unchanged. This implies that the wave function of a stationary state is conserved. Therefore each state of a particle in a centrally symmetric field is characterized by a definite parity. The wave functions $\psi_{Elm} = R_{El} \cdot Y_{lm}(\Theta, \phi)$ transform under inversion ($x \rightarrow -x; y \rightarrow -y; z \rightarrow -z$) or in spherical coordinates ($r \rightarrow r; \Theta \rightarrow \pi - \Theta; \phi \rightarrow \phi + \pi$) according to their l quantum number $Y_{lm}(\pi - \Theta, \phi + \pi) = (-1)^l \cdot Y_{lm}(\Theta, \phi)$. Thus the parity of a state is solely determined by l .

$\mathbf{p}(\mathbf{r}, t) = \boldsymbol{\varepsilon} \cdot \mathbf{p}(\mathbf{r}) \cdot e^{-i\omega t} + \mathbf{c.c.}$, where $\boldsymbol{\varepsilon}$ is the polarization unit vector, ω_L is the driving frequency and $\mathbf{p} = \boldsymbol{\alpha} \cdot \mathbf{E}$. The proportionality factor $\boldsymbol{\alpha}$ named polarizability is complex valued and frequency dependent. In the Lorentz model the atom is described by an elastically bound electron with charge e , mass m_e and oscillating with an eigenfrequency ω_A corresponding to the atomic transition frequency. The equation of motion for the driven system is then

$$\frac{d^2x}{dt^2} = \Gamma \cdot \frac{dx}{dt} + \omega_A^2 \cdot x = -\frac{eE_0}{m_e} \cos(\omega_L \cdot t) \quad (4.1.1)$$

and analogous for the time dependent dipole moment $p(t)$

$$\frac{d^2p}{dt^2} = \Gamma \cdot \frac{dp}{dt} + \omega_A^2 \cdot p = -\frac{e^2E_0}{m_e} \cos(\omega_L \cdot t) \quad (4.1.2)$$

Integration of this equation leads to $p(t) = p_0 \cdot e^{-i\omega_L t}$ with

$$p_0 = \frac{e^2 \cdot E_0}{m_e} \cdot \frac{1}{(\omega_A^2 - \omega_L^2) + i \cdot \Gamma \cdot \omega_L} \quad (4.1.3)$$

The atomic polarizability $\boldsymbol{\alpha}$ and the classical radiative damping rate Γ follows as

$$\boldsymbol{\alpha} = \frac{e^2}{m_e} \cdot \frac{1}{(\omega_A^2 - \omega_L^2) + i \cdot \Gamma \cdot \omega_L}, \quad \Gamma = \frac{e^2 \omega_L^2}{6\pi \epsilon_0 m_e c^3} \quad (4.1.4)$$

In the driving field E the interaction potential is given by

$$U_{dip} = -\frac{1}{2} \langle \mathbf{p} \cdot \mathbf{E} \rangle = -\frac{1}{2\epsilon_0 c} \cdot \text{Re}(\boldsymbol{\alpha}) \cdot \mathbf{I}, \quad \mathbf{I} = 2 \cdot \boldsymbol{\varepsilon}_0 \cdot c |E|^2 \quad (4.1.5)$$

\mathbf{I} denotes the field Intensity, the angular brackets time averaging over the rapidly oscillating terms and the factor of $\frac{1}{2}$ accounts for the reduced strength of the dipole moment, which is an induced and not a permanent one.

The gradient of the dipole potential constitutes a conservative force proportional to the intensity gradient of the field.

$$\mathbf{F}_{dip} = -\nabla U_{dip} = -\frac{1}{2\epsilon_0 c} \cdot \text{Re}(\boldsymbol{\alpha}) \cdot \nabla \mathbf{I}(\mathbf{r}) \quad (4.1.6)$$

At the same time the imaginary part of the polarizability gives rise to a dissipative interaction. Radiation is absorbed from the driving field and spontaneously reemitted. The rate of this process, the scattering rate, computes to

$$R_{sc} = \frac{\langle \dot{\mathbf{p}} \mathbf{E} \rangle}{\hbar \omega} = \frac{1}{\hbar \epsilon_0 c} \cdot \text{Im}(\boldsymbol{\alpha}) \cdot \mathbf{I}(\mathbf{r}) \quad (4.1.7)$$

These classical formulas are valid within a few percent for the D-lines of the Alkali atoms Na, K, Rb and Cs as long as excitation is low and saturation effects are avoided. For dipole traps this condition is usually fulfilled because of the large detuning commonly used.

Under these assumptions the following expressions for the dipole potential and the scattering rate can be derived [131]:

$$U_{dip} = -\frac{3\pi c^2}{2\omega_A^3} \cdot \left(\frac{\Gamma}{\omega_A - \omega_L} + \frac{\Gamma}{\omega_A + \omega_L} \right) \cdot I(\mathbf{r}) \quad (4.1.8)$$

$$R_{sc} = \frac{3\pi c^2}{2\hbar\omega_0^3} \cdot \left(\frac{\omega_L}{\omega_A} \right)^3 \cdot \left(\frac{\Gamma}{\omega_A - \omega_L} + \frac{\Gamma}{\omega_A + \omega_L} \right)^2 \cdot I(\mathbf{r}) \quad (4.1.9)$$

In the optical domain ($\omega_L = 2\pi \cdot 10^{14}$) the laser frequency is relatively close to the atomic resonance at ω_A . This implies that the detuning $|\Delta| = |\omega_L - \omega_A| \ll \omega_A$ is small compared to the resonance frequency, which leads to an important simplification.

The term $\frac{\Gamma}{\omega_A + \omega_L}$ resonant at $\omega_L = -\omega_A$ can be neglected and furthermore one can set $\frac{\omega_L}{\omega_A} \sim 1$. With this so called *rotating wave approximation* (rwa) the previous two equations reduce to:

$$U_{dip} = -\frac{3\pi c^2}{2\omega_A^3} \cdot \left(\frac{\Gamma}{\Delta} \right) \cdot I(\mathbf{r}) \quad (4.1.10)$$

$$R_{sc} = \frac{3\pi c^2}{2\hbar\omega_A^3} \cdot \left(\frac{\Gamma}{\Delta} \right)^2 \cdot I(\mathbf{r}) \quad (4.1.11)$$

Both dipole potential and scattering rate are proportional to the intensity and fulfill

$$R_{sc} = \left(\frac{\Gamma}{\hbar \cdot \Delta} \right) \cdot U_{dip} \quad (4.1.12)$$

As the optical potential scales with $\frac{1}{\Delta}$ and the scattering rate with $\frac{1}{\Delta^2}$ it is possible to reduce unwanted scattering by increasing the detuning Δ .

Dipole traps with large detunings but still operating within the rotating wave regime are designated FORT, far off resonant traps.

For Rb specific values ($\Gamma \simeq 2\pi \cdot 5.9$ MHz and $\omega_A \simeq 2\pi \cdot 10^{14}$ Hz) the electron motion in the classical oscillatory model 4.1.1 is weakly damped. Under these conditions, the modulus of the time dependent, induced dipole moment is retarded in phase with respect to the driving field and the dipole potential can be written as:

$$U(t) = -\mathbf{p} \cdot \mathbf{E} = -|p_0| \cdot E_0 \cdot \cos(\omega_L t) \cdot \cos(\omega_L t + \phi) \quad (4.1.13)$$

Time averaging over the fast optical oscillations leads to

$$U_{dip} = \langle -\mathbf{p} \cdot \mathbf{E} \rangle = -|p_0| \cdot E_0 \cdot \frac{\cos(\phi)}{2} \quad (4.1.14)$$

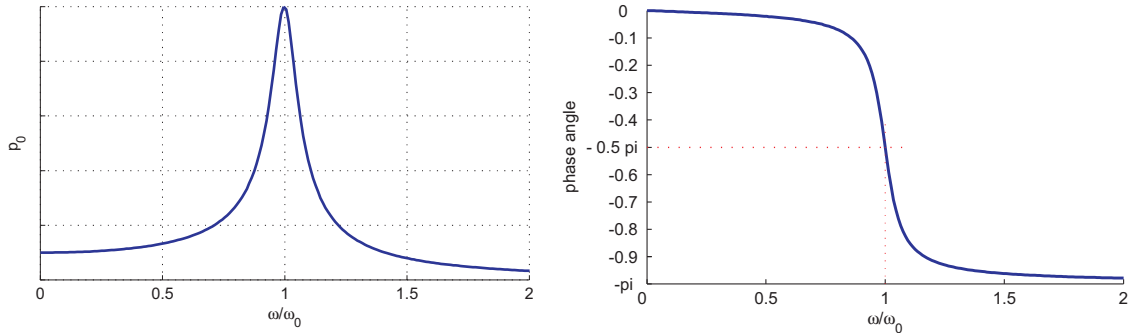


Figure 4.1:

Figure 4.1 shows the amplitude and phase retardance depending on the driving frequency ω .

According to the detuning two operating regimes can be distinguished:

- $\Delta < 0$ “red detuned case“
in this case the driving laser frequency ω is below the atomic resonance frequency ω_A and the phase lag $\phi < \pi/2$. The $\cos(\phi)$ term in 4.1.14 is positive resulting in a potential energy which is always negative. The dipole is attracted towards a minimum of the potential energy and hence to a maximum of the laser field intensity.
- $\Delta > 0$ “blue detuned case“
The $\cos(\phi)$ term in 4.1.14 is negative resulting in a potential energy which is positive. The dipole is repelled from the maxima of the laser field.

4.1.2 The quantum description

Although the classical model works well under certain conditions, it doesn't give a physical account for all effects² of the dipole force especially at high intensities. When the atom-field coupling strength is large compared with the radiative damping rate Γ the atomic system cannot be treated separately from the field. Instead the energy levels of the joint system, atoms and laser photons need to be considered. Spontaneous emission is now fully included as the coupling of the dressed states to the empty modes of the electromagnetic spectrum. This leads to population transfers between dressed states at well defined rates.

For simplicity we assume a two level system with ground state $|g\rangle$ and excited state $|e\rangle$ in a monochromatic laser field without atom-light interaction [45].

The atomic Hamiltonian \mathcal{H}_A is the sum of the kinetic and internal energies with

$$\mathcal{H}_A = \frac{\mathbf{p}^2}{2m} + \hbar\omega_A \sigma_z \quad (4.1.15)$$

²fluctuations of the dipole force, photon correlations or spectral distribution of the emitted light

ω_A designating the atomic resonance frequency and the atomic transition operators

$$\begin{aligned}\sigma^+ &= |e\rangle\langle g| \\ \sigma^- &= |g\rangle\langle e| \\ \sigma_z &= |e\rangle\langle e| - |g\rangle\langle g|\end{aligned}\quad (4.1.16)$$

Assuming the atom at rest and the ground state energy to be 0 leads to

$$\mathcal{H}_{sd} = \hbar\omega_A |e\rangle\langle e| \quad (4.1.17)$$

The photon energy is given by

$$\mathcal{H}_{\mathcal{L}} = \hbar\omega_L \left(\mathbf{a}^+ \mathbf{a} + \frac{1}{2} \right) \quad (4.1.18)$$

a^+ and a are the creation and annihilation operators and ω_L the laser field frequency. The basic states of the field are the photon number states $|n\rangle$.

For detunings small compared to the atomic transition frequency $|\Delta| \ll \omega_A$ the eigenstates of the system $\mathcal{H}_{sd} + \mathcal{H}_{\mathcal{L}}$ form a manifold, where the states $|g, N+1\rangle$ and $|e, N\rangle$ are close to each other. The energy difference between these two levels is $\hbar\Delta$.

Atom Light Interaction

The electrical field of the laser mode at the position of the atom³ with appropriate choice of the coordinate origin equals to

$$\mathbf{E}(r) = \sqrt{\frac{\hbar\omega_L}{2\varepsilon_0 V}} \vec{\epsilon} \cdot (\mathbf{a} + \mathbf{a}^+) \quad (4.1.19)$$

Here V is the mode-volume, ε_0 the permittivity constant and $\vec{\epsilon}$ the polarization unit-vector.

Considering only electrical dipole coupling as the interaction mechanism, the interaction Hamiltonian takes the form :

$$\mathcal{H}_I = -\mathbf{d} \cdot \mathbf{E}(\vec{r}) \quad (4.1.20)$$

$$\mathbf{d} = d_{eg} \cdot (|e\rangle\langle g| + |g\rangle\langle e|), \quad d_{eg} = \langle e|\mathbf{d}|g\rangle = \langle g|\mathbf{d}|e\rangle \quad (4.1.21)$$

which gives :

$$\mathcal{H}_I = g \cdot (|e\rangle\langle g| + |g\rangle\langle e|)(\mathbf{a} + \mathbf{a}^+) \quad (4.1.22)$$

with a coupling constant :

$$g = -\sqrt{\frac{\hbar\omega_L}{2\varepsilon_0 V}} \vec{\epsilon} \cdot d_{eg} \quad (4.1.23)$$

³The extend of the electronic wavepacket is small compared to the laser wavelength, so that the spatial variation of the electric field over the atom can be neglected.

Under the assumption $|\Delta| \ll \omega_A, \omega_L$ and with the neglect of non-resonant contributions the interaction term 4.1.22 simplifies to :

$$\mathcal{H}_I = g(|e\rangle\langle g| \mathbf{a} + |g\rangle\langle e| \mathbf{a}^\dagger) \quad (4.1.24)$$

The interaction couples the states

$$\langle e, N | \mathcal{H}_I | g, N+1 \rangle = g\sqrt{N+1} \quad (4.1.25)$$

More intuitively it is the process of absorption of a laser photon by the ground state with $N+1$ photons in the radiation field which ends up in the excited state with N photons. Nonresonant coupling between the states separated by $\pm 2\hbar\omega_L$ is neglected.

Remark: For a coherent state laser mode [46] with photon number $\langle N \rangle = |\alpha|^2$ the electrical field operator $\mathbf{E}(\mathbf{r})$ can be replaced by the expectation value $\langle \mathbf{E}(\mathbf{r}) \rangle$,

$$\langle \alpha e^{+i\omega_L t} | \mathbf{E}(\mathbf{r}) | \alpha e^{-i\omega_L t} \rangle = E_0 \cdot \cos(\omega_L t), \quad E_0 = 2\sqrt{\frac{\hbar\omega_L}{2\varepsilon_0 V}} \cdot \vec{\varepsilon} \cdot \sqrt{\langle N \rangle} \quad (4.1.26)$$

which leads to a coupling strength of

$$\hbar \cdot \Omega = -d_{eg} \cdot E_0 \quad (4.1.27)$$

with Ω called on-resonance Rabi-frequency.

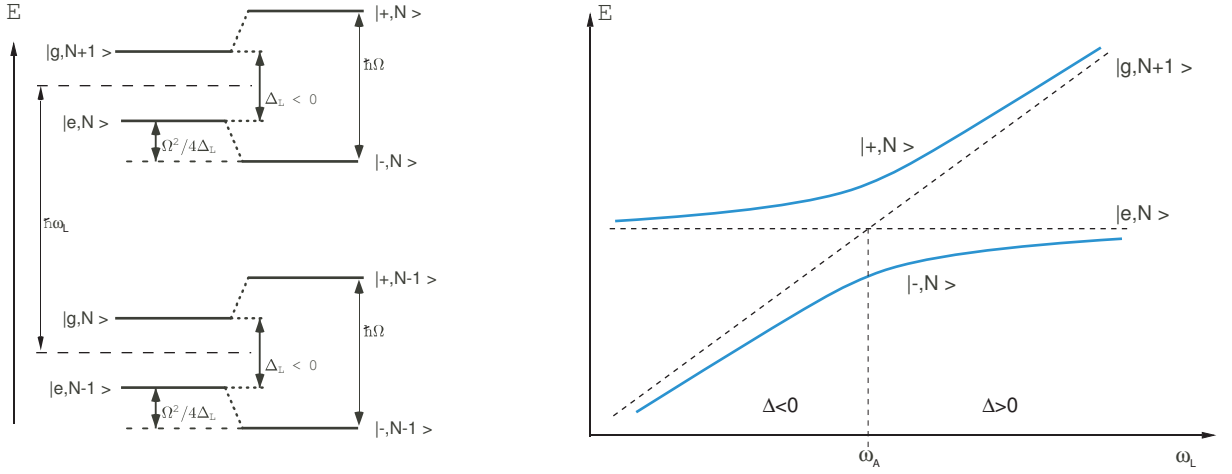
When the two states $|g, N+1\rangle, |e, N\rangle$ are coupled by the laser field, the resulting new states $|1, N\rangle, |2, N\rangle$. the so called dressed states, are linear combinations of the unperturbed ones. They are formed by a unitary rotation of the basis states by a so called mixing angle θ .

$$\begin{pmatrix} |1, N\rangle \\ |2, N\rangle \end{pmatrix} = \begin{pmatrix} \sin(\theta) & \cos(\theta) \\ \cos(\theta) & -\sin(\theta) \end{pmatrix} \begin{pmatrix} |g, N+1\rangle \\ |e, N\rangle \end{pmatrix}, \quad \tan(2\theta) = -\frac{\Omega}{\Delta} \quad (4.1.28)$$

The energy separation between pairs of dressed states with the generalized Rabi frequency Ω_R is :

$$\hbar\Omega_R = \hbar\sqrt{\Omega^2 + \Delta^2} \quad (4.1.29)$$

The dipole interaction leads to new stationary states and wavefunctions, different from the uncoupled one.



(a) left: uncoupled and coupled states of the atom-field system; right: energies of the dressed states depending on the photon energy

Figure 4.2:

In the weak excitation limit $|\Omega| \ll |\Delta_L|$ the perturbed energies are⁴ :

$$\begin{aligned} E_+ &\approx \frac{\hbar}{2} |\Delta| \left(1 + \frac{\Omega^2}{2\Delta^2} \right) = -\hbar \left[\frac{\Delta}{2} + \frac{\Omega^2}{4\Delta} \right] \\ E_- &\approx \hbar \left[\frac{\Delta}{2} + \frac{\Omega^2}{4\Delta} \right] \end{aligned} \quad (4.1.30)$$

The physical consequences of this result are of great practical importance. The optically induced shift of the ground state is exactly the opposite of the excited state shift and can be identified as the dipole trapping potential (8.0.9). In most cases the light field is not homogenous producing a spatial variation of the light shift $\Delta E(\vec{r})$. The force resulting from this change of the atomic internal energy in the varying light field is called the dipole force.

The sign of the dipole force can be understood in the following way. Image 4.3 shows the dressed states $|+, N\rangle$ and $|-, N\rangle$ depending on the position inside the light field. Outside the high intensity region, the dressed states can be identified as the uncoupled ones $|g, N+1\rangle$ and $|e, N\rangle$ (10.2), inside the region the level shift follows the intensity distribution. If the detuning Δ is negative, the state $|-, N\rangle$ coincides with $|g, N+1\rangle$ outside the light field. Therefore it has less contribution from the excited state and is more populated than $|+, N\rangle$ (red disks represent the population). The net force resulting from the population difference hence attracts the atoms towards the intensity maximum. For positive detuning ($\Delta > 0$) the same reasoning applies with $|g, N+1\rangle$ and $|e, N\rangle$ exchanged, leading to a repulsion of atoms

⁴This result can be derived from second order time independent perturbation theory of non-degenerate states.

The interaction Hamiltonian \mathcal{H}_I causes an energy shift given by $\Delta E_i = \sum_{j \neq i} \frac{|\langle j | \mathcal{H}_I | i \rangle|^2}{E_i - E_j}$. Applying the Hamiltonian from 4.1.20 $\mathcal{H}_I = -\mathbf{d} \cdot \mathbf{E}(r)$ and taking into account that the energy difference of the ground and excited state is $E_i - E_j = (N+1)\hbar\omega_L - \hbar\omega_A - N\hbar\omega_L = \hbar(\omega_L - \omega_A) = \hbar\Delta$, we can write with help of 4.1.28 $\Delta E = \pm \frac{|\langle e, N | \mathcal{H}_I | g, N+1 \rangle|^2}{\hbar\Delta} = \pm \frac{\hbar\Omega^2}{4\Delta}$

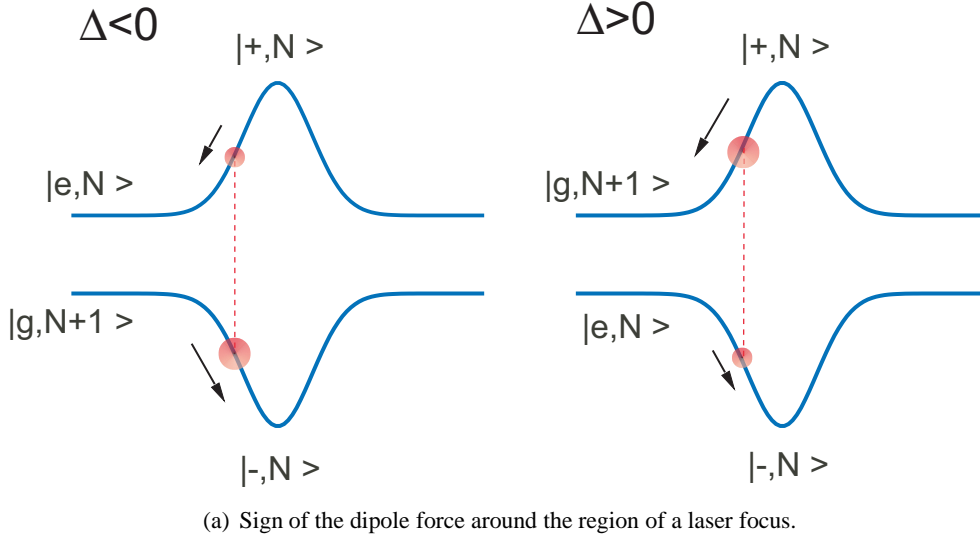


Figure 4.3:

from intensity maxima. Finally, if $\Delta = 0$, both dressed states are superpositions of equal amounts of ground and excited states and the net force vanishes.

4.2 Multilevel Atoms

The derivation of the energy level shift in the previous chapter assumed a two level system. In reality many atomic levels are coupled by the radiation field, depending on the orientation of the dipole moment and the light polarization. Rewriting 4.1.20 in a slightly different way gives the standard expression for the dipole hamiltonian.

$$\mathcal{H}_I = -e\vec{r} \cdot \vec{\mathcal{E}} \quad (4.2.1)$$

with \vec{r} the position vector of the electron, $\vec{\mathcal{E}}$ the polarization vector of the light and e the elementary charge unit. Expressed in terms of atomic transition operators $\sigma_{ij} = |i\rangle\langle j|$ between the possible levels $|i\rangle$ in the ground state and $|j\rangle$ in the excited state, we can write

$$e\vec{r} \cdot \vec{\mathcal{E}} = \sum_{i,j} e|i\rangle\langle j|\vec{r} \cdot \vec{\mathcal{E}}|i\rangle\langle j| = \sum_{i,j} \mu_{ij} \sigma_{ij} \quad (4.2.2)$$

with $\mu_{i,j} = e\langle i|\vec{r} \cdot \vec{\mathcal{E}}|j\rangle$ denoting the electric-dipole transition matrix element. The value of this dipole matrix element depends on the specific ground and excited state wavefunctions and is complicated to calculate.

In a spherical coordinate system with unit vectors

$$u_+ = \frac{1}{\sqrt{2}}(e_x + ie_y), \quad u_- = \frac{1}{\sqrt{2}}(e_x - ie_y) \quad u_0 = e_z \quad (4.2.3)$$

the factor $\vec{\mathbf{r}} \cdot \vec{\mathbf{E}}$ can be written as

$$\mathbf{r} \cdot \mathbf{u}_q = \sqrt{\frac{4\pi}{3}} \cdot r \cdot Y_1^q(\theta, \phi) \quad (4.2.4)$$

where

$$Y_l^m(\theta, \phi) = \sqrt{\frac{2l+1}{4\pi} \cdot \frac{(l+m)!}{(l-m)!}} \cdot P_l^m(\cos(\theta)) e^{im\phi} \quad (4.2.5)$$

is the spherical harmonics function [47] and $q = 0, \pm 1$ specifies the polarization state.

In general atomic wavefunctions for stationary states can be expanded in the form

$$\psi = R(r) \cdot Y_l^m(\theta, \phi) \quad (4.2.6)$$

⁵ which allows the factorisation of the matrix element in a radial r dependent part and an angular part

$$\mu_{ij} = \|\mu\| \cdot c_{ij} \quad (4.2.7)$$

The reduced matrix element $\|\mu\|$ depends only on the orbital wavefunction (Wigner-Eckard theorem [51]), whereas the coupling strength coefficients c_{ij} takes into account the laser polarization and the electronic and nuclear angular momenta.

In a simple case without fine- and hyperfine interactions and with n, l, m denoting the principal, orbital, and magnetic quantum number and $q = 0, \pm 1$ specifies the linear or circular light polarization state 4.2.7 may be written as

$$e \langle i | \vec{\mathbf{r}} \cdot \vec{\mathbf{E}} | j \rangle = e \langle n', l', m' | \vec{\mathbf{r}} \cdot \vec{\mathbf{E}} | n, l, m \rangle = e \langle n', l', m' | r | n, l \rangle \langle l', m' | \sqrt{\frac{4\pi}{3}} \cdot Y_1^q | l, m \rangle \quad (4.2.8)$$

The evaluation of the angular contribution of the matrix element involves integrals of products of spherical harmonics and is conveniently done within the framework of irreducible tensor operators [48].

$$\langle l', m' | \sqrt{\frac{4\pi}{3}} \cdot Y_1^q | l, m \rangle = (-1)^{l'-m'} \sqrt{\max(l, l')} \cdot \begin{pmatrix} l' & 1 & l \\ -m' & q & m \end{pmatrix} \quad (4.2.9)$$

The element in brackets is a 3j-symbol, which can be evaluated with standard software [49] or [48].

⁵This is valid under the assumption of an arbitrary centrally symmetric electrostatic potential for each electron created by the nucleus and the rest of the electrons. Since angular momentum is conserved for motion in an arbitrary centrally symmetric field, the stationary states can be characterized by the square of the angular momentum and the z-component.

4.2.1 Fine and Hyperfine interactions

The formulas presented so far do not include fine- or hyperfine interactions. Spin-orbit interaction and the coupling of the nuclear spin I to the total angular momentum J leads to a splitting of the principal energy levels and in atomic elements commonly used for laser-cooling the useful transitions for cooling and optical pumping are in most cases between specific hyperfine sub-states

Calculation of the geometrical contribution to the dipole matrix element involves the expansion of the atomic state F dependent eigenfunctions in the spin, orbit (S,L) basis and recoupling of all subsequent Clebsch-Gordan coefficients [50].

Analogous to eq. 4.2.8 the two hyperfine sublevel $|F, m_F\rangle$ and $|F', m'_F\rangle$ couple via the dipole interaction, resulting in a reduced double bar matrix element $e\langle F', m'_F || r || F \rangle$ which is independent of the magnetic sub-states and a coupling coefficient that only depends on the magnetic quantum numbers.

$$e\langle F', m'_F | \vec{r} \cdot \vec{\epsilon} | F, m_F \rangle = e\langle F' || r || F \rangle \cdot (-1)^{F''-1+m_F} \sqrt{2F+1} \cdot \begin{pmatrix} F & 1 & F' \\ m_F & q & -m'_F \end{pmatrix} \quad (4.2.10)$$

The symmetry properties of the 3j-symbol ensure that its value vanishes unless $m'_F = m_F + q$, which reflects the selection rule $\Delta m = 0, \pm 1$ and the fact that the light couples only to the angular momentum and not the electronic or nuclear spin.

Further simplification of the reduced matrix element by factoring out the F and F' dependence gives

$$e\langle F' || r || F \rangle = e\langle J' || r || J \rangle \cdot (-1)^{F''+J+1+I} \sqrt{(2F+1)(2J'+1)} \cdot \left\{ \begin{matrix} J' & J & 1 \\ F & F' & I \end{matrix} \right\} \quad (4.2.11)$$

The 6 quantum numbers inside curly braces is a Wigner 6j-symbol. They are a generalization of Clebsch-Gordan coefficients and Wigner 3j-symbols that arise in the coupling of three angular momenta [48, 49].

Again the matrix element in the J -basis can be expanded in the (L,S) basis resulting in a second 6j-symbol and a only L dependent fully reduced matrix element.

$$e\langle J' || r || J \rangle = e\langle L' || r || L \rangle \cdot (-1)^{J+L'+1+S} \sqrt{(2J+1)(2L'+1)} \cdot \left\{ \begin{matrix} L' & L & 1 \\ J & J' & S \end{matrix} \right\} \quad (4.2.12)$$

Numerical values of the reduced transition matrix elements $e\langle L' || r || L \rangle$ are calculated from radiative lifetime measurements of the involved states. The radiative decay time constant or Einstein A coefficient is given by [52]

$$\frac{1}{\tau} = A_{ij} = \frac{\omega_0^3}{3\pi\epsilon_0\hbar c^3} \cdot \frac{2J+1}{2J'+1} \cdot |\langle J || r || J' \rangle|^2 \quad (4.2.13)$$

Finally the full dipole matrix element in the (L,S,I) basis can be expressed as

$$\mu_{ij} = e \langle L' || r || L \rangle \cdot X \cdot \left\{ \begin{array}{ccc} L' & J' & S \\ J & L & 1 \end{array} \right\} \left\{ \begin{array}{ccc} J' & F' & I \\ F & J & 1 \end{array} \right\} \begin{pmatrix} F & 1 & F' \\ m_F & q & -m'_F \end{pmatrix} \quad (4.2.14)$$

$$X = (-1)^{1+L'+S+J+J'+I-m'_F} \cdot \sqrt{(2F+1)(2F'+1)(2J+1)(2J'+1)}$$

An important symmetry property of the dipole operator is that all excited state hyperfine sublevels $|F', m'_F\rangle$ decay with the same rate constant Γ .

The relative strength of a transition from $F \rightarrow F'$ is obtained by summing up all transitions from the single ground state sublevel to the excited state levels belonging to a particular F' energy.

$$S(F, F') = (2F'+1)(2J+1) \cdot \left\{ \begin{array}{ccc} J' & J & 1 \\ F & F' & I \end{array} \right\}^2 \quad (4.2.15)$$

All line strength coefficients sum up to 1

$$\sum_{F'} S(F, F') = 1. \quad (4.2.16)$$

With the possibility to calculate dipole matrix elements for arbitrary hyperfine transitions the energy shift of the electronic ground state $|g\rangle_i$ and associated with it the dipole potential $U_{dip,i} = \Delta E_i$ ⁶ can be written in the form

$$\Delta E_i = \frac{3\pi c^2 \Gamma}{2\omega_{Aij}^3} \cdot I \cdot \sum_j \frac{|c_{ij}|^2}{\Delta_{ij}} \quad (4.2.17)$$

Here the sum has to include all coupled excited states $|e\rangle_j$. The line strength coefficients $|c_{ij}|^2$ can be calculated with eq. 4.2.14 and $\Delta_{ij} = (\omega_L - \omega_{Aij})$ is the detuning of the laser field from transition $i \rightarrow j$.

For practical calculations however formula 4.2.17 is tedious to apply because of the large number of levels to be considered. In case of large detuning of the laser field compared to the hyperfine-splitting energies $\hbar\Delta_{HFS}$, $\hbar\Delta'_{HFS}$ a more simplified formula can be derived as shown in the following.

Rb like other alkali elements has a fine structure split excited state D-line doublet $^2S_{1/2} \rightarrow ^2P_{1/2}, ^2P_{3/2}$ as well as hyperfine split ground- and excited states. For laser detunings $\Delta \gg \Delta'_{HFS}$ the excited hyperfine-states remain unresolved and the optical potential and scattering rate of a specific $|^2S_{1/2}, F, m_F\rangle$ ground state is [131]

$$U_{dip} = \frac{\pi c^2 \Gamma}{2\omega_A^3} \cdot I \cdot \left(\frac{2 + q \cdot g_{FMF}}{\Delta_{2,F}} + \frac{1 - q \cdot g_{FMF}}{\Delta_{1,F}} \right) \quad (4.2.18)$$

⁶In case of negligible saturation ($\Omega \ll (\Delta^2 + \Gamma^2)$) the trapping potential can be identified with the ground state energy shift. If excited states are significantly populated, a mean trapping potential can be estimated by summing up contributions from all populated levels weighted by their occupation probability.

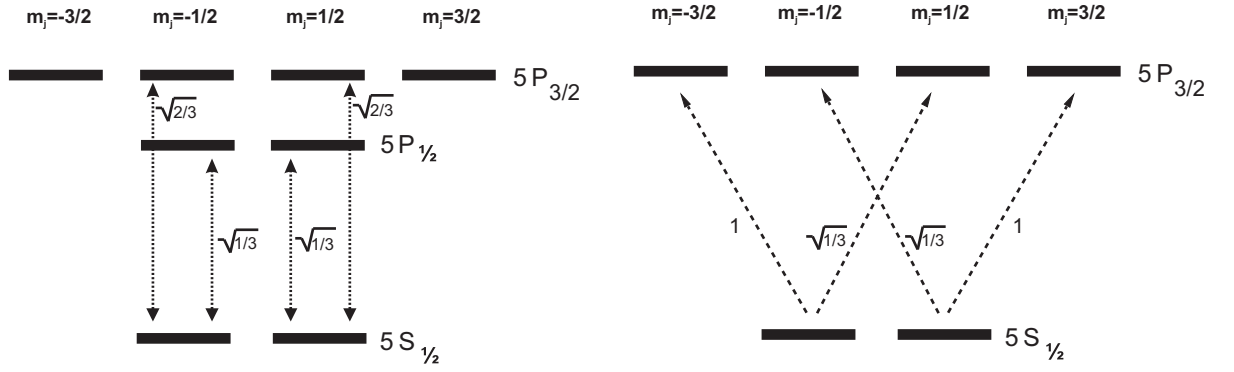
(a) Clebsch-Gordan coefficients for π and σ -transitions in a $J=1/2 \rightarrow J'=1/2, 3/2$ system.

Figure 4.4:

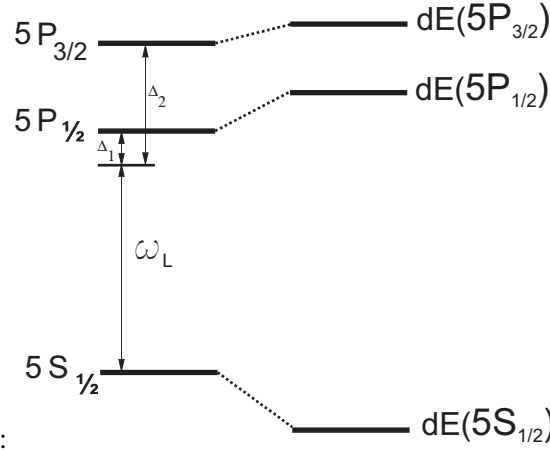


Figure 4.5:

(b) Energy level shifts of the D1 and D2 transition in Rb for negative detuning.

$$R_{sc} = \frac{\pi c^2 \Gamma^2}{2\omega_A^3} \cdot I \cdot \left(\frac{2 + q \cdot g_F m_F}{\Delta_{2,F}^2} + \frac{1 - q \cdot g_F m_F}{\Delta_{1,F}^2} \right) \quad (4.2.19)$$

Here, both detunings $\Delta_{1,F}$ and $\Delta_{2,F}$ are taken relative to the center of the hyperfine-split $^2P_{3/2}$ and $^2P_{1/2}$ states, g_F denotes the Landè g-factor

$$g_F = \frac{F(F+1) + J(J+1) - I(I+1)}{F(F+1)} \quad (4.2.20)$$

and $q = 0, \pm 1$ the laser polarization. the two terms inside the brackets can be understood as the contributions of the two resolved $J'=1/2$ and $J'=3/2$ excited states D-lines with coupling strengths of $1/3$ for the D1 and $2/3$ for the D2 line, respectively.

Care must be taken by selecting the polarization of the dipole laser light. Circularly polarized light ($q = \pm 1$) leads to magnetic sub-level dependent energy shifts [53] as well as optical pumping to the outermost Zeeman sub-states. For linear polarization ($q = 0$) combined with a detuning exceeding the ground state hyperfine splitting the trapping potential becomes independent of the particular hyperfine and magnetic sub-states.

4.3 Gaussian Beam Traps

As position dependent intensity distributions lead to an optical potential and a dipole force, which in case of red detuning is attractive towards the maximum of the intensity, a single focused laser beam is sufficient to trap atoms. This idea, first proposed by Ashkin [10] and later demonstrated by Chu and coworkers [12] proved highly successful due to its robustness and simplicity. For blue detuned traps the situation is different. Here a spatial region has to be fully surrounded by the repulsive light fields, which is more difficult to achieve. Combinations of light sheets [54] or hollow-beam arrangements (Laguerre-Gaussian-modes) [55, 57] have been invented to store and guide atoms. But the most successful application proved to be optical lattices [56], were combinations of red detuned standing wave light fields create a periodic array of microtraps.

Optical potential of a single beam trap

Laser beams launched from a Fabry-Perot Cavity (a typical laser resonator) propagate as Gaussian beams to a good approximation⁷. In practical terms, most lasers are designed to emit a TEM₀₀ -field mode.

The intensity of a Gaussian beam propagating along z is given at any point by

$$I(r, z) = I(z) \cdot e^{-\left(\frac{2r^2}{\omega(z)^2}\right)} = I_0 \cdot \frac{1}{1 + \left(\frac{z}{z_0}\right)^2} \cdot e^{-\frac{2r^2}{\omega(z)^2}} \quad (4.3.1)$$

whereby $z = 0$ is the location of the beam waist or focus.

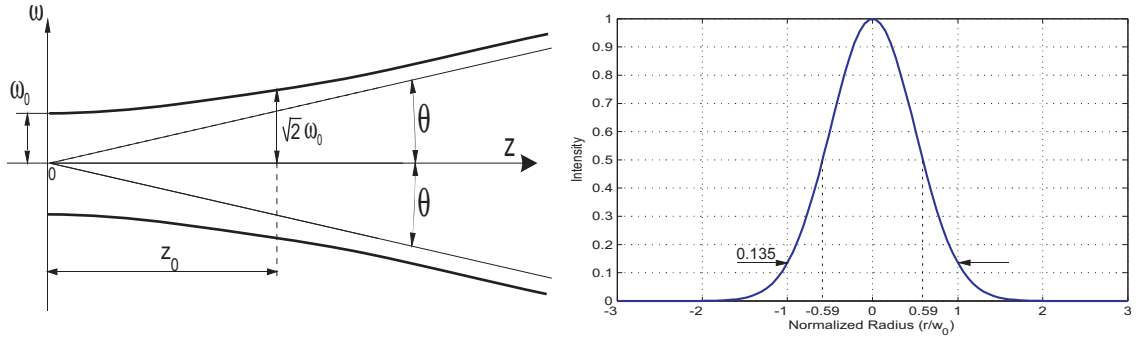
The max. intensity I_0 is related to the optical power P as

$$I_0 = \frac{2P}{\omega_0^2 \pi} \quad (4.3.2)$$

The Gaussian-beam radius $\omega(z)$ is defined as the radial beam coordinate where the intensity is $1/e^2 \approx 13.5\%$ of the on-axis value

$$\omega(z) = \omega_0 \sqrt{1 + \left(\frac{z}{z_0}\right)^2} \quad (4.3.3)$$

⁷As the Fourier-transform of a Gaussian field distribution is itself a Gaussian, it remains Gaussian at every point along its path of propagation throughout the optical system.



(c) (left:) axial profile of a Gaussian beam, (right:) radial profile

Figure 4.6:

$$I(r = \omega, z) = 1/e^2 \cdot I(\omega, z = 0).$$

the beam waist radius is

$$\omega_0 = \omega(z = 0),$$

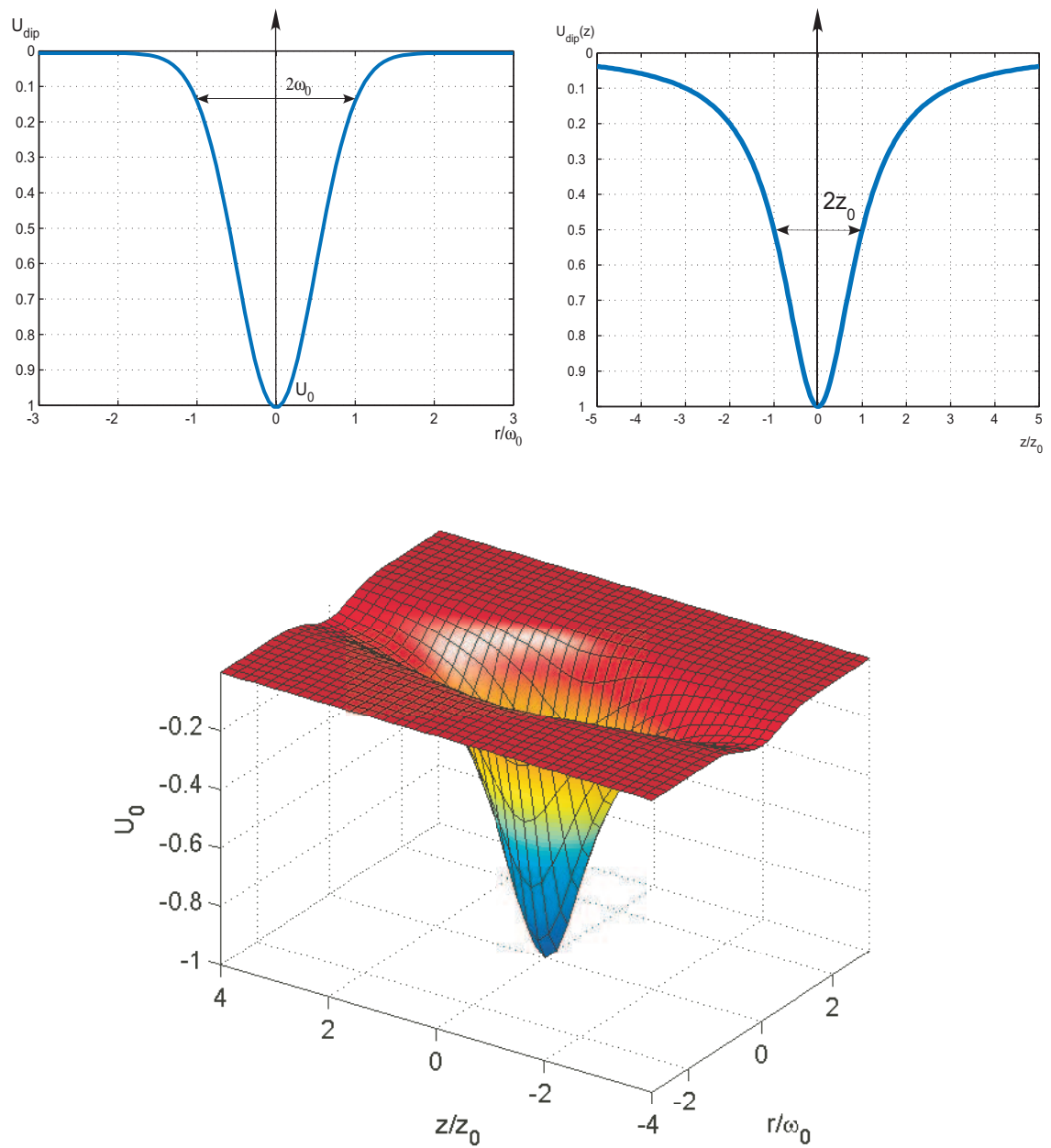
and the Rayleigh range z_0 is the distance at which the on-axis intensity drops to half the peak value $I(z_0) = \frac{I_0}{2}$.

$$z_0 = \frac{\pi \omega_0^2}{\lambda} \quad (4.3.4)$$

Given the expression for the spatial intensity distribution 4.3.1 and the optical potential ?? it is straightforward to calculate the ground state trapping potential.

$$U_{dip} = U_0 \cdot \frac{1}{1 + (\frac{z}{z_0})^2} \cdot e^{-\frac{2r^2}{\omega_0^2(1 + (\frac{z}{z_0})^2)}} \quad (4.3.5)$$

$$U_0 = \frac{\pi c^2 \Gamma}{2 \omega_\lambda^3} \cdot I_0 \cdot \left(\frac{2 + q \cdot g_F m_F}{\Delta_{2,F}} + \frac{1 - q \cdot g_F m_F}{\Delta_{1,F}} \right) \quad (4.3.6)$$



(a) Optical potential of a single Gaussian beam (bottom) and radial and axial dependence (top).

Figure 4.7:

5 The dipole laser setup

The dipole-laser setup is a completely new design compared to the previously used one which was constructed around a tunable Ti:Sa ring laser system operated around 810 nm¹. The diode-pumped Yb:YAG solid state laser system² in use now emits light which is much further detuned (250 nm) requiring a major reconstruction of the optical setup.

The first part of this section presents the laser system followed by a description of the beam delivery to the photonic-crystal fibers and output optics. The last part is dedicated to the photo-multiplier system and low light detection.

5.1 The Dipole-Laser

There are several considerations when choosing a laser system for atom trapping. Most important are wavelength, output power, mode spectrum quality, beam shape and noise properties.

The diode-pumped disk laser system from ELS Elektronik-Laser Systems provides high output power of up to 23 W at 1030 nm with a perfect Gaussian beam profile.

The active lasing element is a 240 μm thin disc of Yb:YAG crystal which acts as a high reflector for the linear laser cavity at one side. A parabolic mirror in front of the disk reflects pump-laser light 24 times on the disc thereby multiplying the absorption length.

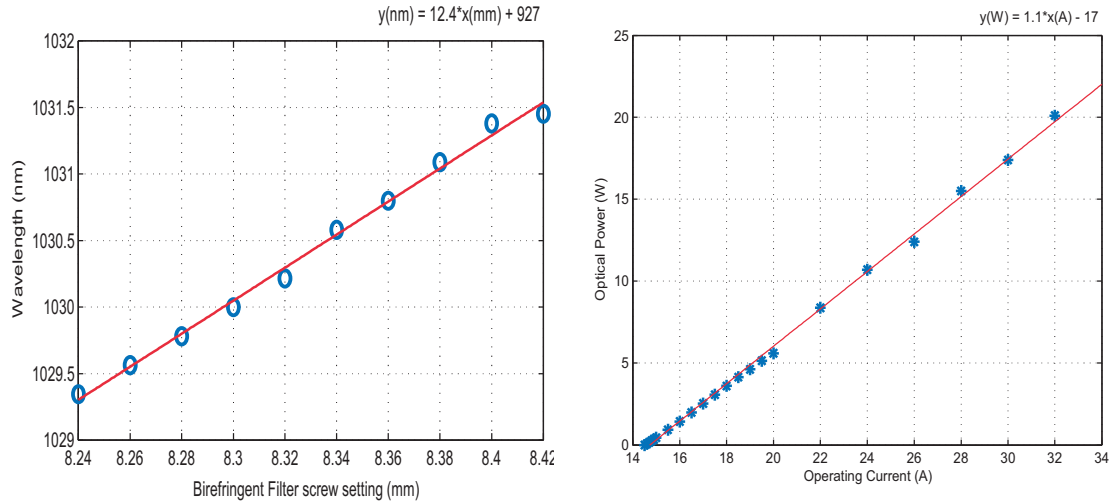
As the Yb:YAG crystal gain curve allows lasing between 1000 and 1060 nm, a birefringent filter in the laser cavity allows selection of a specific frequency. The filter can be adjusted with a manual fine pitch screw. Selected modes have a separation of 0.254 nm or 71.8 GHz. The alignment of the filter at the Brewster angle selects a single linear polarization state from the otherwise random polarization.

For single frequency operation, an intracavity etalon is installed, which reduces the emission linewidth to less than 5 MHz but accompanied by a power drop of 30% compared to multi frequency TEM₀₀ operation. For the far-detuned laser the linewidth is not critical. More important is longitudinal mode stability resulting in mode-hop free operation. Intensity stability and noise reduction is achieved by two servo circuits for the pump power control eliminating low frequency current noise and high frequency (20-50 KHz) noise originating from relaxation oscillations.

Optical output power is linear with the diode current starting at the lasing-threshold at 15 A (5.1).

¹Coherent 699

²ELS Elektronik-Laser Systems VersaDisk 1030



(a) Wavelength dependence on the birefringent filter setting (left) and optical output power vs. drive current (right)

Figure 5.1:

5.1.1 Power Stability and Noise Performance

Fluctuations in the intensity and position of the trapping beams are a source of heating and limit the lifetime of trapped atom samples [82] while drifts in the power stability changes trapping conditions and thus lead to an increased spread for repetitive measurements.

Figure 5.2 shows the fractional output power stability $\varepsilon(t) = \frac{P(t) - \langle P(t) \rangle}{\langle P(t) \rangle}$ over one hour operating time. The laser was operated in current regulation mode³. The measured power stability is 0,9% r.m.s.

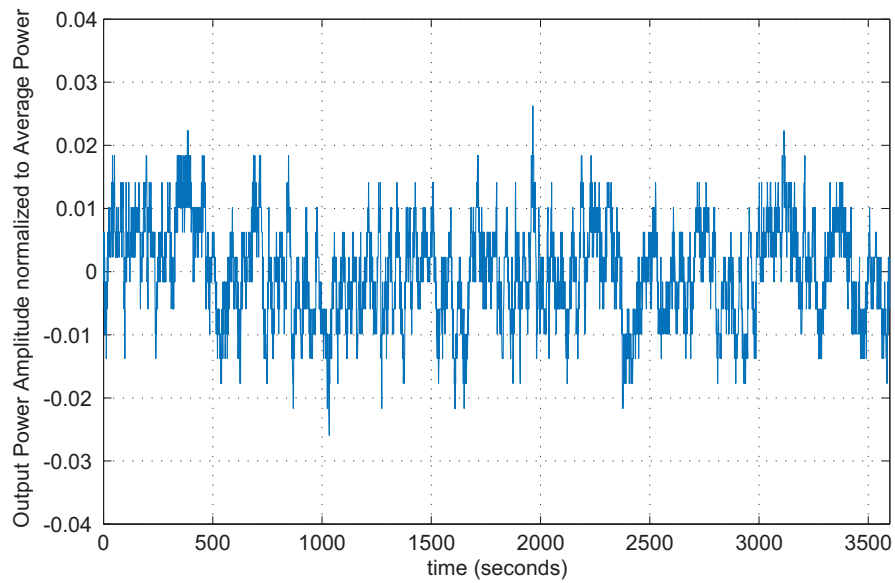
To see the effects of the different operating modes and the time-scales of the intensity variations a long term measurement with high time resolution was made. A comparison of the Allan deviation of the fractional power stability for current and power regulation modes is shown in 5.3. Both operating modes show minima for averaging times of 0.6 and 300 seconds with a peak power instability of 0.5% for 10 seconds.

In figure 5.4 the power spectral density (psd) relative to the carrier of the intensity fluctuations is shown. The bandwidth is 1 Hz and the frequency ranges from 0 to 50 KHz. This is equivalent to a measurement of the Relative Intensity Noise (RIN) [83] spectrum and confirms the noise specifications from the manufacturer⁴.

Fluctuations in the intensity of the laser beams causes exponential heating for the trapped atoms. Long heating time constants require stringent limits for the noise power spectra of the laser.

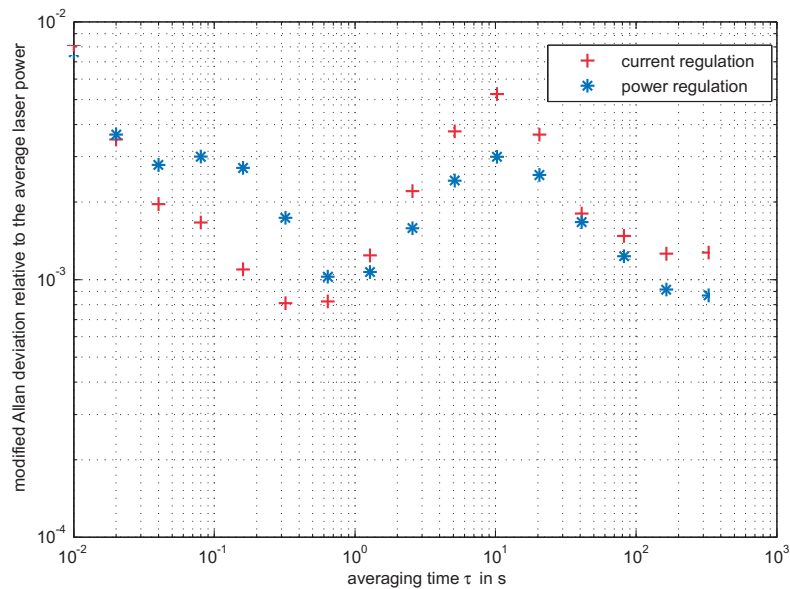
³According to the manufacturer power regulation mode is not a recommended operating mode.

⁴RIN measurement of VersaDisk 1030, 5-100KHz, ELS GmbH



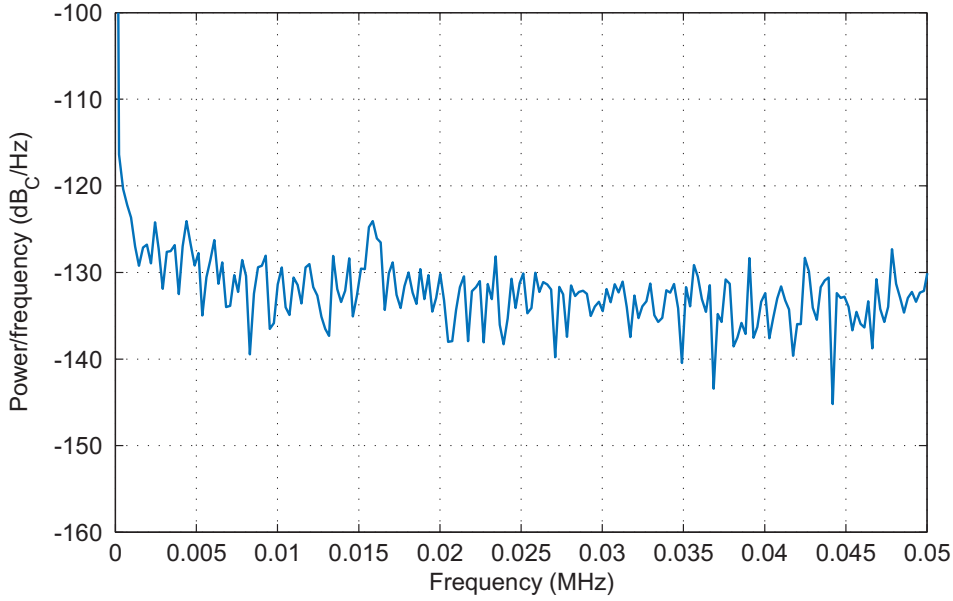
(a) Optical output power fluctuation normalized to the average power level of the ELS disc-laser over 1 hour. For the measurement 10000 data-points were recorded.

Figure 5.2:



(a) Intensity stability curves for power regulation mode and current regulation mode.

Figure 5.3:



(a) Relative intensity noise (RIN) spectrum of the VersaDisk 1030 laser in the range of 0-50 kHz.

Figure 5.4:

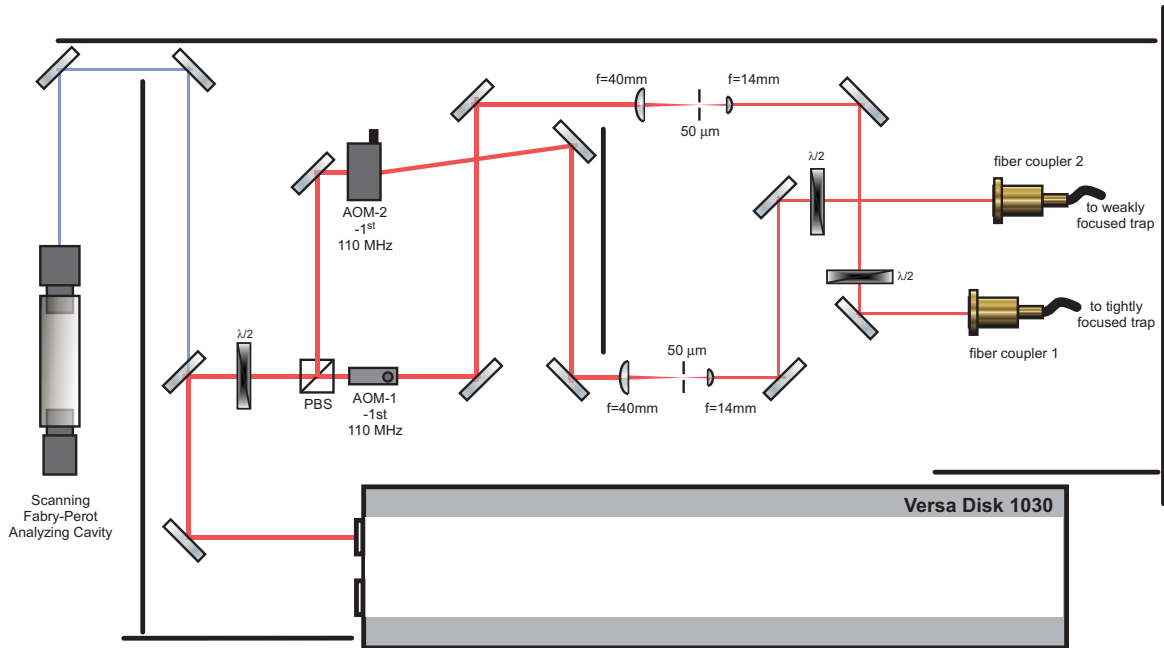
In Ref. [82] it was shown that the heating rate constant $\Gamma = \frac{\langle \dot{E} \rangle}{\langle E \rangle}$ is given by:

$$\Gamma = \pi^2 v_{trap}^2 S_{\epsilon}(2v_{trap}) \quad (5.1.1)$$

where v_{trap} is the trap frequency and $S(2v_{trap})$ the power spectrum of the fractional intensity noise evaluated at $2 \cdot v_{trap}$. From equation 5.1.1 can be seen that the heating rate is proportional to the laser light Intensity ($I \sim v_{tr}^2$) and is a parametric process, sensitive to the noise at twice the trap oscillation frequency.

According to this formula $\sqrt{S_{\epsilon}(2v_{trap})} = 1.3 \cdot 10^{-6} \text{Hz}^{-1/2}$ is required to achieve a 10 sec. heating time constant for our tight trap with 75 KHz trapping frequency. The measured fractional intensity noise of our laser system is $\epsilon_0 = 9.5 \cdot 10^{-3}$ (rms, 0-250 KHz) which leads to a heating time constant of $\tau = 1/\Gamma = 0.05$ seconds. This shows that external intensity stabilization of the dipole laser is necessary to reduce the significant heating in tight dipole traps.

Position fluctuations are another source of heating, but unlike intensity fluctuations the heating rate is sensitive to the noise power at the trap oscillation frequency. Great care had been taken to select mechanical components in the beam delivery path. High stability optics mounts and massive bases prevent beam pointing instabilities and long-term drifts as much as possible.



(a) Scheme of the dipole-laser beam distribution and fiber-coupling set-up.

Figure 5.5:

5.2 Light Distribution

5.2.1 Beam Path

Our setup distributes the dipole light coming from the ELS-VersaDisk laser over 2 symmetric beam paths allowing independent switching and intensity control of the beams for the tight and shallow dipole trap.

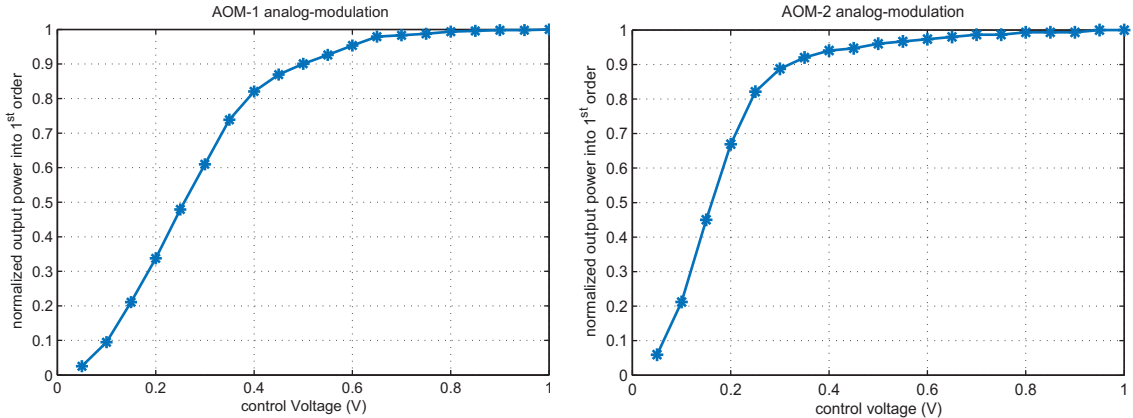
The linear polarized laser beam is split by a polarizing beam splitter into variable amounts set by a half-wave plate. After passing an acousto-optic modulator⁵ the diffracted beams pass a spatial filter which serves two purposes: The $f=40\text{mm}/f'=14\text{mm}$ lens combination acts as a telescope while the $50\ \mu\text{m}$ pinhole filters unwanted spatial frequencies in the focal plane. Thereby its main function is to act as a mode cleaner for the distorted transversal beam profile of the diffracted beam from the AOM. Any deviation from a perfect Gaussian mode profile would result in increased heating of the fiber coupler and ends of the the photonic-crystal fibers.

The second function is to reduce the beam diameter from 2.2 mm to 0.75 mm which is the matched spot diameter for the high power fiber couplers⁶. The $f=40\text{mm}/f'=14\text{mm}$ lens combination acts as a telescope while the $50\ \mu\text{m}$ pinhole filters unwanted spatial frequencies in the focal plane.

Right after the spatial filter are two mirrors for alignment of the beams with respect to the

⁵Crystal Technology Inc. Model 3110-125

⁶Schäfer+Kirchoff 60SMS-A11



(a) Transmission of the acousto-optic modulators in beam-path 1 and 2 with respect to the applied control voltage.

Figure 5.6:

optical axis of the fixed mounted fiber couplers⁷. Half wave plates in front of the couplers provide a means for setting an arbitrary linear polarization state. Total combined transmission for the AOM, spatial filter and the fiber is around 60%.

For monitoring the longitudinal mode spectrum of the laser, a small percentage of light is coupled into a scanning Fabry-Perot cavity with a free spectral range (FSR) of 800 MHz and finesse of 310.

5.2.2 The Acousto-Optic Modulator

We use a Crystal Technology Inc. Model 3110-125 TeO₂ acousto-optic modulator which has a very high diffraction efficiency of 90% at 1030 nm when supplied with 2W of RF-power by a 110 MHz source⁸. The input aperture is large enough that the laser beam can be used without the need of a telescope. Intensity modulation with a RF-contrast of 35 dB can be achieved by applying a control voltage (0-1V) to the analog input of the RF-source. A spline interpolation and linearization of the transfer functions (see figure 5.6) allow the convenient setting of power levels within the experiment-control program. When used for switching purposes, the rise-time and the modulation bandwidth are limited by the modulator to 200 ns and 300 MHz, respectively.

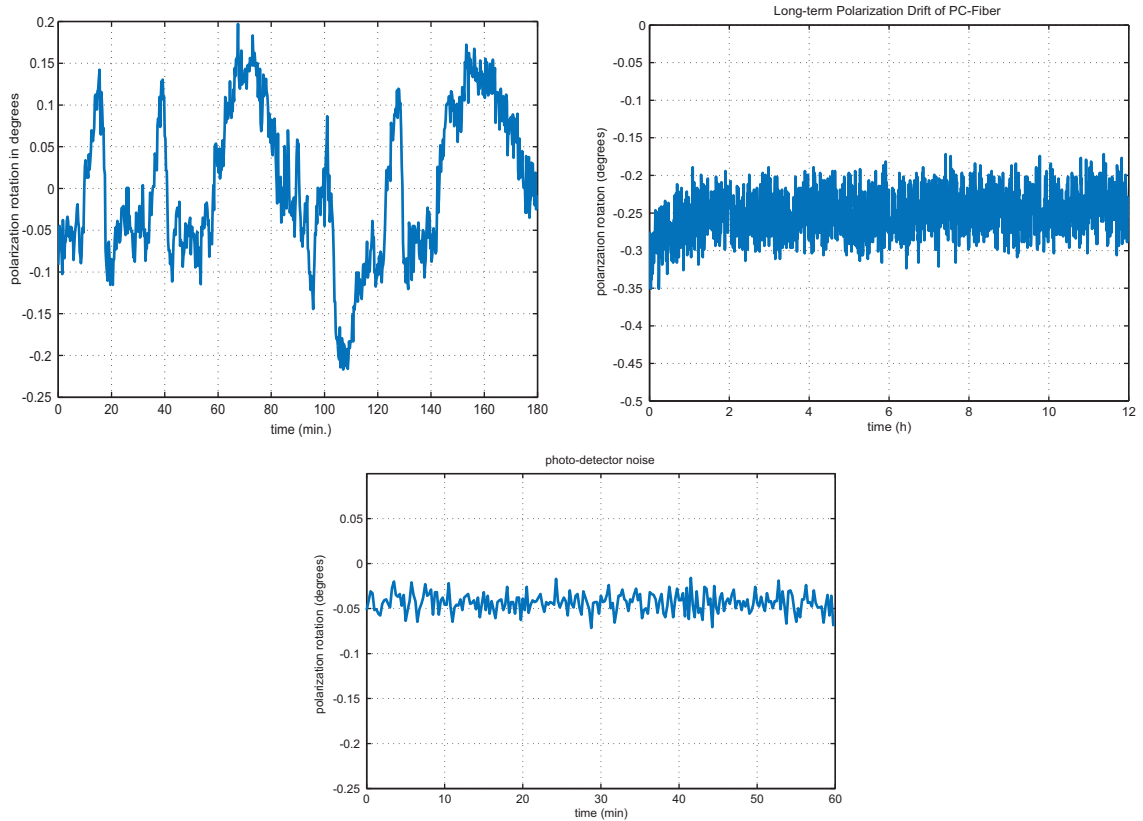
5.2.3 Fiber Coupling

Due to the high levels of optical power (up to 15 W) being incident on the single-mode fiber facet the coupling is not a trivial task. A coupling optics specially matched to the fiber and high mechanical stability components are necessary.

The incoming beam with a diameter of 0.78 mm is focused to a spot size of 19.6 μm with

⁷For stability reasons the fiber couplers are fixed

⁸Crystal Technology Inc. 1110AF-AIFO-2.0



(a) Polarization drift caused by transmission of linearly polarized light through 2m of LMA-25 photonic-crystal fiber (upper graphs). For comparison, the noise from the detector system with the laser shut (bottom)

Figure 5.7:

the Schäfter+Kirchoff 60SMS-A11 fiber coupler. This spot diameter matches the mode-field diameter of the photonic crystal fiber (PCF)⁹ ($19.8 \pm 2 \mu\text{m}$). The large core size of $25 \mu\text{m}$ allows transfer of more than 10 W of laser power while maintaining a single transversal mode at the output¹⁰. This is contrary to standard (step-index) single mode patch cords where the max. power would be limited to around 3W due to their smaller core size.

Coupling efficiency is as high as 80% for low power levels and degrades slightly to 75% at higher power settings. For test purposes 13.5W of light was coupled into the fiber for several hours resulting in stable 10W power after the output-coupler. Care must be taken when changing the beam power as the coupling has to be optimized for a certain power level¹¹. Due to substantial heating of the AOMs and fiber couplers at high power levels, coupling efficiency is only optimal for a specific power setting.

⁹LMA-25 from Crystal Fibre A/S

¹⁰Although the cladding has a sixfold symmetry, the mode profile is similar to a Gaussian fundamental mode of a conventional fiber.

¹¹The fiber facet can easily be burned when the coupling is not optimal

The LMA-25 fiber is a solid core photonic crystal fiber with symmetrically arranged holes in the cladding and exhibits very low birefringence. However bending and thermal expansion can cause stress-induced birefringence which lead to uncontrollable changes of the polarization state. Since no data were available for the polarization stability of our 2 m fiber we measured the drift behavior over time (see figure 5.7). The measurements showed that as long as the fiber is not touched and temperature remains stable, the polarization rotation remains within 0.35 over 3 h.

On both ends the fiber is equipped with angle-polished FC connectors to minimize etalon effects and back-reflection from the fiber facets.

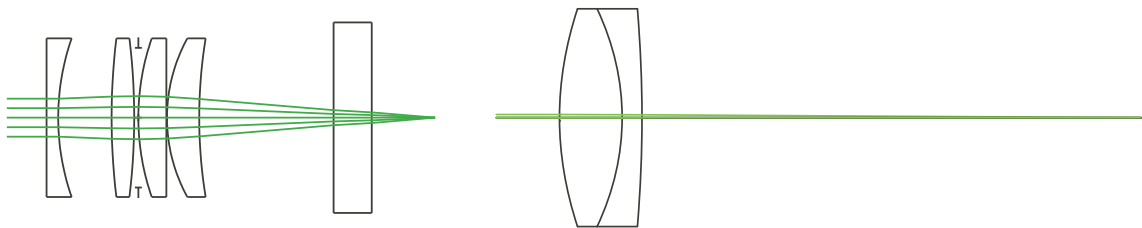
5.2.4 Dipole Optics at the Trap

After transfer of the dipole trap light to the trap assembly by the fiber, the laser light is collimated and focused into the center of the vacuum cell. The different waist sizes of the strongly focused trap ($\omega_0 = 5.5\mu\text{m}$) and the orthogonally placed weak trap ($\omega_0 = 56\mu\text{m}$) require two different sets of optics.

For beam path 2 (strongly focused trap) an $f=90$ mm triplet-lens objective¹² collimates light coming from the PCF fiber to 6.1 mm diameter. After passing a dichroic mirror, the home-built 4-lens objective (see chapter ?? for full details) focuses the light into the center of the cell.

The whole assembly of fiber-collimator and focusing optics is mounted on a X-Y-Z flexure stage¹³ providing precise and stable positioning of the dipole beam axes within ± 1 mm from the center position.

On beam path 1, light from the fiber is collimated with an $f=14$ mm objective¹⁴ to 0.9 mm diameter and focused into the cell with a doublet lens system of 80mm focal length¹⁵ (see figure 5.8). Here the optical elements are mounted directly to the trap assembly for maximum stiffness.



(a) 4 element imaging optics for the tight dipole trap with $f=35.8$ mm (left) and doublet-lens with $f=80$ mm focal length for the shallow trap (right). The beam waist sizes of the dipole-beams are $\omega_0 = 5.4\mu\text{m}$ and $\omega_0 = 56\mu\text{m}$

Figure 5.8:

¹²LINOS High Power HALO 038908

¹³Elliot Scientific Martock Gold

¹⁴LINOS High Power HALO 038900

¹⁵LINOS NIR doublet 322396

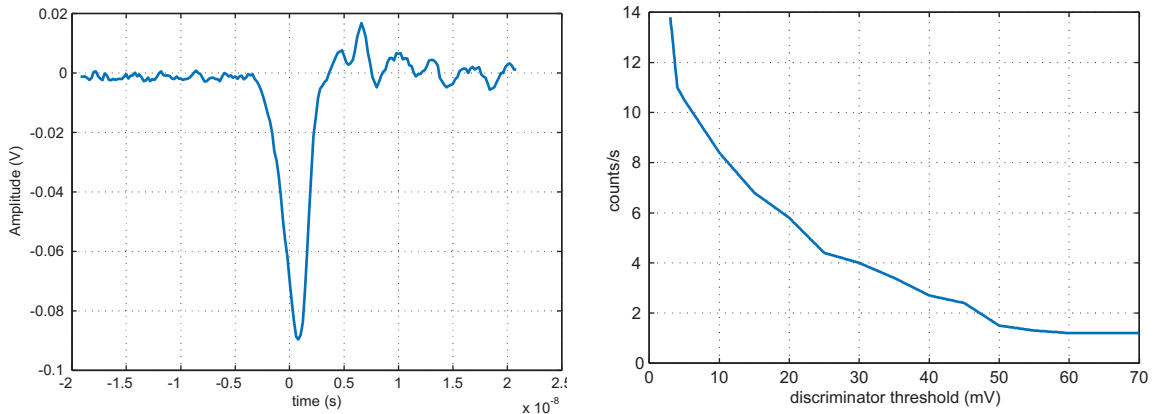
5.3 The Photomultiplier

Detection of low numbers of atoms requires highly sensitive detectors. The systems of choice include intensified CCD-cameras, photomultipliers and avalanche photo-diodes, the latter ones when no spatial information is required.

For integrated detection of all atoms with high efficiency we use a photomultiplier that contains a peltier-cooled 51mm diameter Ga:As:Cs-O tube¹⁶. The photo cathode is sensitive between 185 and 930 nm and quantum efficiency is 10% at 780 nm. Operating Voltage is 1600V where current amplification reaches $1 \cdot 10^6$.

Pulses from the photomultiplier are pre-amplified by a factor of hundred¹⁷ and shaped for processing in a dedicated pulse-counter¹⁸ (see figure 5.9). Readout of the pulse-counter is done via GPIB and LabView.

Anode dark counts from thermionic emission are reduced by cooling to -30° and measured to be 9 cts/s for -10mV discriminator threshold and 1600V operating voltage (5.9).



(a) Photomultiplier pulse after amplification by a factor of 100 and pulse shaping (left). Average dark counts/s vs. discriminator threshold of the pulse counter (right).

Figure 5.9:

Fluorescence light from the atoms is imaged with the same objective¹⁹ as the dipole beam to ensure that the imaged atoms coincide with the trapped ones. Reflected by a dichroic mirror which transmits the dipole light, the collimated fluorescence light is focused by a $f=200$ mm doublet through a $200 \mu\text{m}$ pinhole and collimated again by a 25 mm lens. For alignment purposes the pinhole and the 25 mm lens are independently adjustable with translation stages. This spatial filter assembly is necessary to suppress stray-light from reflections of the optical components. After this the light is coupled²⁰ into a multi-mode fiber patch-cord²¹ which

¹⁶Burle C31034A-02

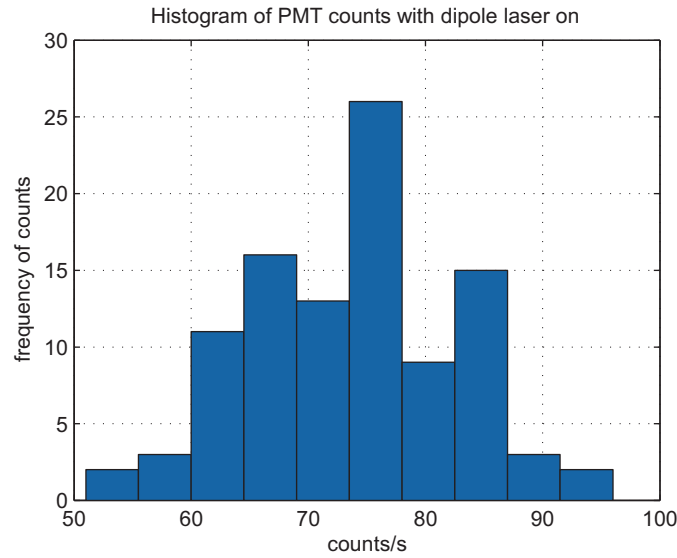
¹⁷EG&G VT120

¹⁸Stanford Research Systems gated photon-counter SR400

¹⁹ $f=36$ mm, 4 lens

²⁰Thorlabs F260 FC-B

²¹Thorlabs NA=0.22, $62.5 \mu\text{m}$ core, FC-connectors



(a) Histogram of the background count rate when the dipole laser is on. The dipole laser light has no measurable effect on the count rate.

Figure 5.10:

goes to the photomultiplier. Behind the output coupler²² an interference band-pass filter with 85% transmission blocks all contributions from the dipole-laser light. Measured total transmission of the detection channel to the photo-cathode is 60%.

Figure 5.10 shows the count rate distribution²³ of background counts when the detection channel is open and the dipole laser is in on (3W). Blocking the dipole laser has no effect on the stray-light rate as the photocathode is not sensitive to the dipole laser light. This is important for detecting atoms in the trap which would otherwise be impeded by the trapping light.

The imaging system detects light from a region of $18\mu\text{m}$ around the trap center in radial direction which is emitted within the numerical aperture of the objective ($\text{NA}=0.27$).

²²Schäfer & Kirchoff 60FCA6-3

²³The distribution fits a normal distribution with $\mu = 74$ cts/s and $\sigma = 9$ cts/s

5.3.1 Total detection efficiency

Losses in the detection system:

Element	Number of Elements	Transmission
solid angle		0.02
cell window	1	0.96
4-lens objective	1	0.965
dichroic filter	1	0.95
gold mirror	1	0.97
focusing lens	1	0.98
filter assembly+fiber		0.6
PMT quantum efficiency		0.1
total fraction of light detected		$1 \cdot 10^{-3}$

During detection of atoms while they are in the dipole trap, the resonant excitation leads to rapid heating and trap loss. Furthermore the repulsive light-shift of the excited state forces the atoms out of the high intensity regions²⁴. Effectively the atoms are accelerated away from the trap center until they decay back to the ground state thus gaining kinetic energy.

For an excited state population of 1% during detection the calculated count rate per atom is 400 cts/s. Background count rate with the vertical detection laser and dipole laser on amounts to about 300 cts/s. The increase in count rate to the case where the detection channel is open but the detection laser is off (75 cts/s, see figure 5.10) shows that the major contribution to the stray-light background comes from the resonant detection laser.

With this system it should be in principle possible to detect single atoms from the background. Using APD²⁵ detectors instead of a photomultiplier would increase the quantum efficiency to 60%²⁶ and result in a 6 times higher count rate per atom for the trade-off of increased detector dark counts²⁷.

²⁴This depends on the wavelength of the trapping laser. For certain wavelengths ground and excited state lightshifts are the same (magic wavelengths)

²⁵Avalanche photo detector

²⁶Perkin Elmer SPCM-AQR data sheet

²⁷The best SPCM-modules have max. 25 dark counts/s

6 Laser Trapping of Rb

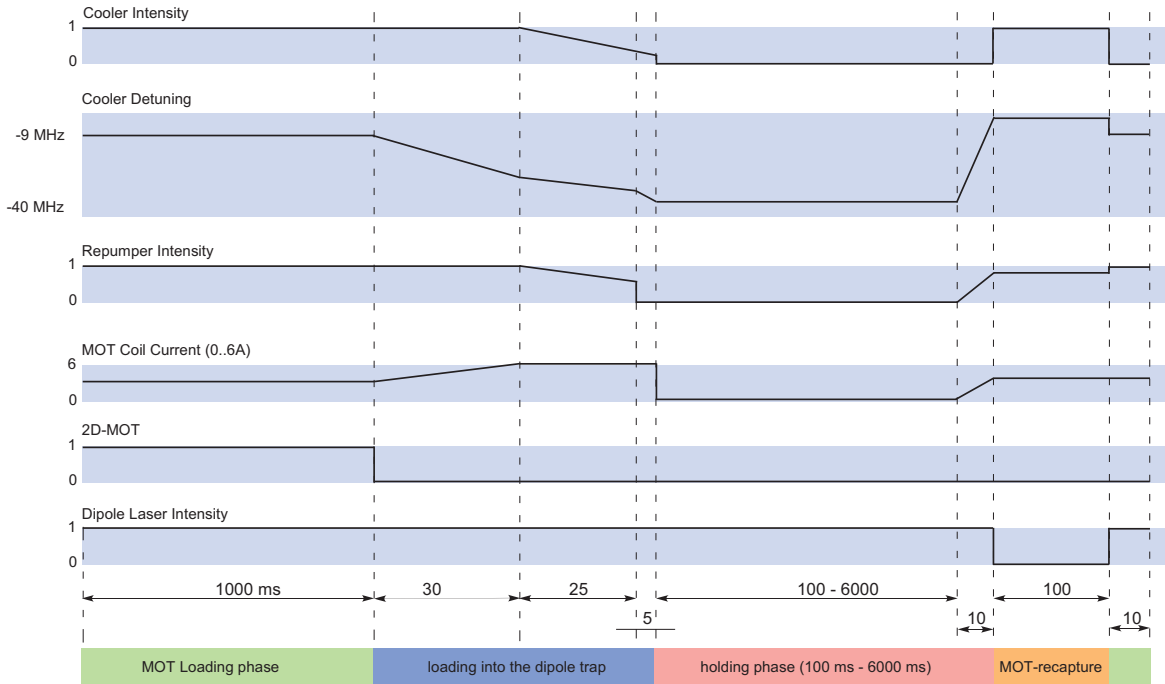
Trapping atoms with dipole forces induced by far-detuned laser light has been the subject of study for many years. More recently the all-optical production of Bose-Einstein Condensates (BEC) [84–86] or degenerate Fermi gases [89] and the possibility to store all magnetic-spin states simultaneously [87, 88] caused increased attention. In most of these cases large samples of cold atoms are transferred from a MOT into a far-off-resonance (FORT) dipole trap. Still, efficient loading of the FORT is challenging as not all aspects of the loading and loss processes are fully understood. Key factors for maximum loading are the suppression of excited state collisions by reduction of the repump light and increased detuning of the MOT lasers [90]. Geometrical effects such as the trap volume and the overlap position also play an important role [91]. Although not vital for the tight trap, maximum trapping efficiency will be important for the spin-squeezing experiments with the shallow trap [106].

This chapter presents the main experimental findings of production, detection and spectroscopic characterization of cold, dense and mesoscopic trapped atom clouds. First the experimental cycle is described followed by an outline of the detection process for free and trapped atoms. Characterization of the trap and the trapped atom samples starts with the investigation of the loading- and loss processes in the dipole trap and continues with trap-oscillation frequency, temperature and density measurements. In the final section measured data are presented and compared to a mathematical model for calculating trap population spectra, taking into account the realistic gaussian-beam trapping-potential.

6.1 The Loading Cycle

6.1.1 Timing Sequence

A typical dipole-trap loading cycle (depicted in Fig.6.1) starts by accumulating atoms in the MOT for 1 second, which provides a cloud of $\sim 10^7$ atoms at a temperature of $\sim 50\mu K$. In the next 30 ms the cooler light is detuned to -30 MHz and the MOT quadrupole-coil current increased to 6A, thereby compressing the atom cloud. A second compression stage lasting 25 ms follows, during which the cooling light is detuned further and at the same time reduced in intensity. The repump intensity is also reduced while the coil current remains at 6A. The last part of the dipole loading phase is employed to optically pump the atoms to the lower hyperfine ground state by switching off the repump light for several ms. This



(a) Timing sequence of a loading and recapture cycle

Figure 6.1:

inhibits hyperfine-changing collisions which otherwise would be a dominant loss channel of the FORT [143]. During the whole loading and transfer process the dipole light is on¹.

After the MOT light fields and magnetic field are extinguished the dipole light provides the sole trapping potential. This phase, which we refer as to the holding phase, lasts usually from 100 ms up to several seconds.

When a recapture measurement is done, during which atoms are captured back into the MOT for fluorescence detection, the MOT light fields are switched on and tuned close to resonance while the dipole light is turned off. This starts with a period of 10 ms where parameters are changed and allowed to settle for following detection interval. In the next 100 ms fluorescence is recorded on the photodiode. Finally all parameters are set back to initial conditions and the MOT cooling light is shut off, preparing the trap for the next cycle to begin.

6.1.2 Overlap of the Dipole Trap and MOT

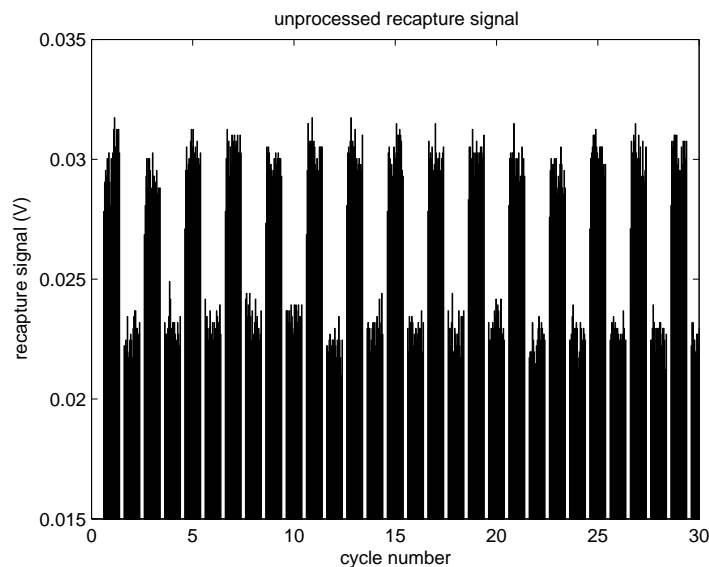
Loading efficiency is strongly dependent on the spatial overlap between the MOT atoms and the dipole beam center. At first thought one would expect best results for coinciding trap centers. Experiments however showed that optimum loading occurs when MOT and FORT

¹Although the dipole light disturbs the loading process of the MOT, it resulted more practical to keep it on, in order to avoid strong thermal lensing effects caused by the coupling of the high-power dipole light into the PC-fibers.

are slightly displaced by an amount that depends on the ratio of the trapping potential to the atom temperature [90]. This implies that for each setting of the dipole laser power the MOT position has to be adjusted for optimum loading efficiency. Additionally the compression of the MOT by ramping up the magnetic field gradient during the last loading stages may cause the MOT center to shift.

Basic alignment is done by imaging the MOT cloud and the attenuated dipole beam directly onto the CCD-camera. Then the MOT is shifted around by precisely moving the quadrupole and compensation coils until their trap centers coincide. This procedure is repeated for an orthogonal direction. After increasing the dipole beam power to normal operating levels (several Watts), fine adjustment follows by maximizing the recapture signal while changing the MOT position.

6.2 Recapture Detection



(a) Raw recapture signal from the photodiode after 100 ms of holding time in the dipole trap. Every second cycle is a background measurement. The signal corresponds to about 50000 atoms.

Figure 6.2:

Recapture detection is straight-forward since the only diagnostic element needed is a photodiode for fluorescence detection. After a variable holding phase, the atoms are recaptured into the MOT and their fluorescence is recorded. Figure 6.2 shows a raw-data graph of sev-

eral measurement cycles where recapture alternates with background detection. This measurement gives reliable data as long as loading from the background can be neglected. Also the atom number has to be sufficiently large since the MOT beams generate considerable stray-light at the cell windows².

6.3 Photomultiplier Detection

Fluorescence detection with the photomultiplier in photon counting mode provides a highly sensitive means of gaining information about important trap parameters.

In contrast to the recapture method, the detection on the freely released atoms allows determination of their total number, which in conjunction with the trapping time gives information about loss processes. This is referred to as lifetime measurements. Furthermore, determination of atom-loss rates while modulating the trapping potential reveals trap-oscillation frequencies.

Atom temperatures can be inferred by monitoring the fluorescence decay over time which is connected to the time dependent density distribution, and trap state occupation can be measured by doing spectroscopy on the trapped sample, i.e. exciting the atoms with variable laser frequency while the atoms are trapped.

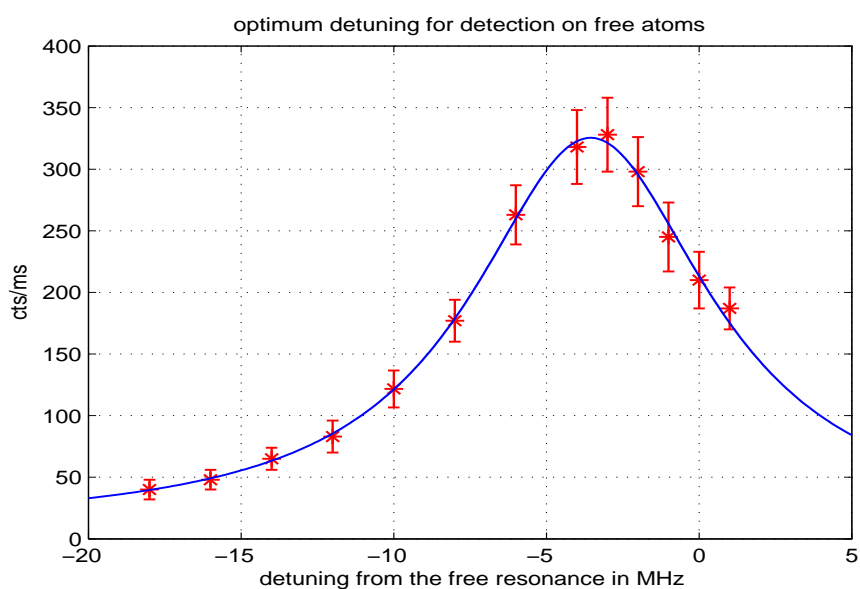
All these measurements will be explained in detail later in this chapter. First the differences between detection of free and trapped atoms with the photomultiplier are described.

6.3.1 Free Atoms

For the detection of free atoms that have been released from the dipole trap, these atoms are illuminated for a short time (in the ms. range) with the single retro-reflected MOT-beam. The large beam diameter ensures that all atoms are illuminated, and the intensity is $\sim 0.7 * I_{Sat}$. Since the laser beam is orthogonal to the detection channel, stray light is minimized. Figure 6.3 shows the detuning for detection with the single MOT-beam pair. Optimum detuning is around 3.5 MHz to the low-frequency side of the free-atom resonance. Because the MOT-beam pair constitutes a one dimensional optical molasses, atoms are effectively cooled when the detuning $\Delta \approx -\frac{\Gamma}{2}$ and remain longer inside the detection region. The fit to the data points is a Lorentzian lineshape centered at $\Delta = -3.55$ MHz and with a full width of 9 MHz³. Purely saturation broadening with $I = 0.7 * I_{Sat}$ gives a calculated linewidth of 7.8 MHz. Taking the transient nature of the detection process and cooling/heating processed into account these values are satisfactorily consistent.

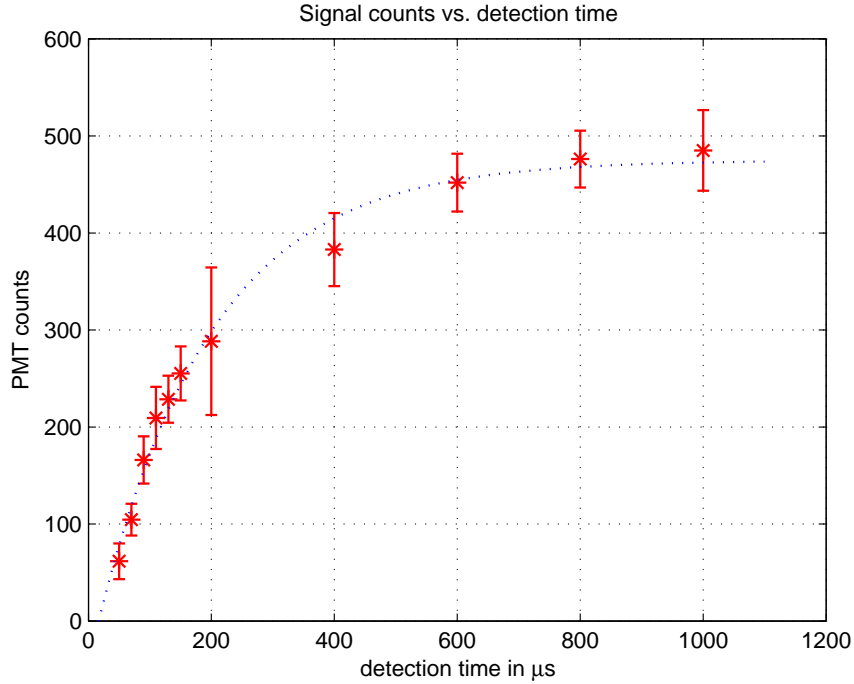
²The photodiode detection limit is about 8000 atoms, set by the stray-light level of the MOT beams. The photodiode had to be removed from the optimal position in order to make place for the spin-squeezing probe beam. At the optimal position the detection limit is about 1000 atoms [60].

³For a thermalized sample with combination of homogeneous line-broadening and Doppler-broadening mechanisms the line-shape function is a Voigt-profile. For cold atoms, Doppler-broadening can be neglected and a broadened Lorentzian lineshape function assumed.



Photomultiplier count rate of free atoms released from the dipole trap vs. detuning of the detection laser. Detection time is 1 ms, holding time 300 ms. The fit to the data points is a Lorentz-lineshape function centered at -3.55 MHz and with a full width of 9 MHz. Doppler broadening can be neglected. Stars represent the mean value and error bars the standard deviation of 20 independent measurements.

Figure 6.3:



(a) Saturation of the PMT-signal counts at longer integration times. The dashed line shows a fit of an exponential loss-model to the data. Detuning of the detection beam is -4 MHz. Each data point represents the mean value of 20 measurements, error bars indicate the standard deviation.

Figure 6.4:

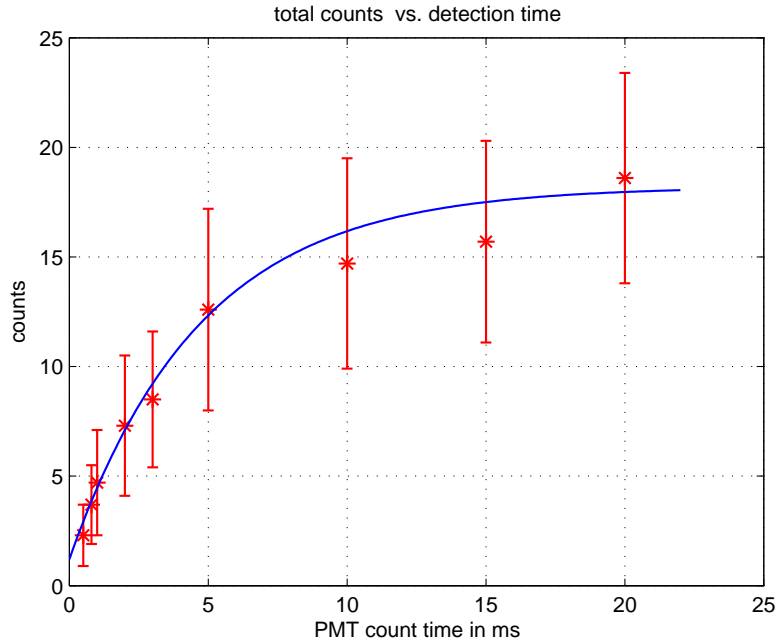
Influence of the detection time

As detection is a lossy process, signal to noise ratio is optimized for a certain detection time. Assuming a constant heating rate caused by the near-resonant beam leads to exponential atom loss and therefore signal loss over time. Dark counts of the photomultiplier increase linearly in time, which favors short detection times.

Figure 6.4 shows that the total photomultiplier counts saturate around 1 ms gate time when a detection beam detuning of -4 MHz is used. A longer detection window does not increase the signal. Atom number, and proportional to it the number of scattered photons, decrease exponentially. The time constant of the exponential loss model

$$sig(t) = c \cdot (1 - e^{-t/\tau}) \quad (6.3.1)$$

evaluates to $\tau = 185 \mu s$, where t is the the PMT integration time and $sig(t)$ the accumulated signal counts.



Fluorescence detection of trapped atoms: Total photomultiplier counts vs. gate time. The solid line shows a fit of the exponential loss model with time constant $\tau = 7.4$ ms (see eq.6.3.1). Holding time is 100 ms, probe beam detuning +18 MHz, the trapping potential is 200 MHz. Repumper light was added to increase the count rate.

Figure 6.5:

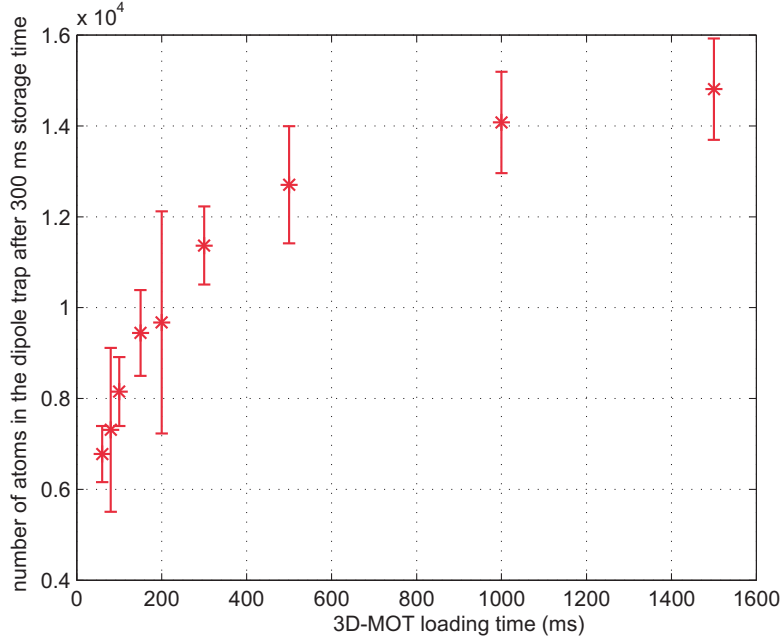
6.3.2 Trapped Atoms

When the atoms are trapped in a sufficiently deep trap, the detection time can be significantly extended. A trapped atom scatters photons until it has gained enough energy to escape the trapping potential. On the other hand, in contrast to the free-atom case, the strong light shift causes spatially dependent transition frequencies, so that the detection laser excites only part of the atoms.

In the example displayed in Figure 6.5 saturation of the signal counts occurs around 20 ms, which is 20 times the free atom equivalent, and the exponential time constant is $\tau = 7.4$ ms. The probe beam detuning was set to +18 MHz and repumper light was added to avoid optical pumping.

6.3.3 Loading Efficiency

Loading atoms from the MOT into the dipole trap is a complex physical process. Efficiency is dictated by the flux into the trapping region and the capture probability inside this region [90]. A simplified picture, which ignores all effects of collisional processes, is the following. Atoms enter the trapping region with an energy according to a Maxwell-Boltzmann velocity distribution corresponding to the 2D-MOT temperature and are slowed down by the



(a) Atom number in the dipole trap after 300 ms holding time vs MOT loading time. It can be seen that the number of atoms in the dipole trap saturates for longer loading times. Fluorescence is recorded over 1 ms with the photomultiplier system.

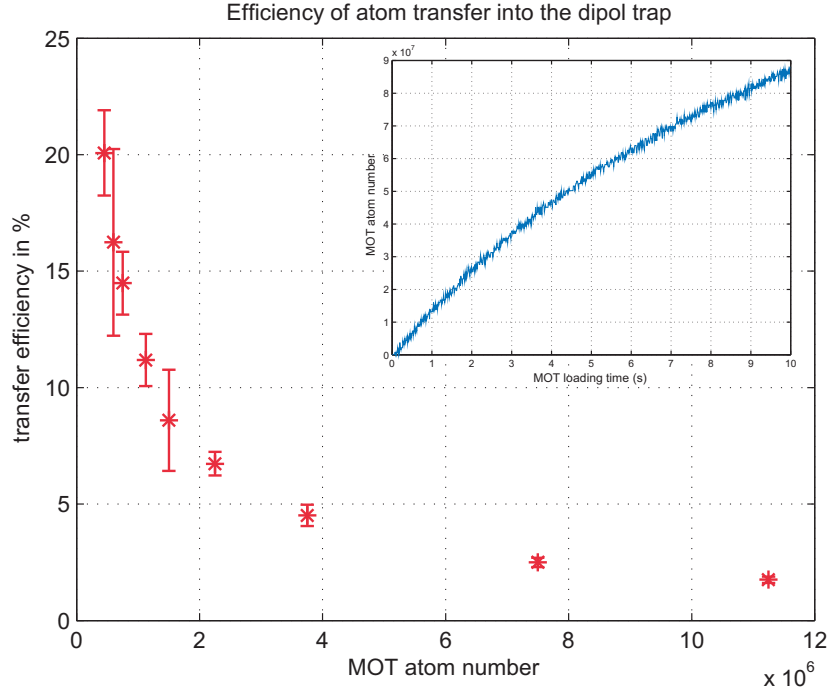
Figure 6.6:

dissipative light forces of the 3D-MOT. If the reduction in kinetic energy over half an oscillation period in the dipole trap is large enough that the energy is reduced below the rim of the potential, then the atom remains trapped.

Influence of the MOT size:

The small volume of the dipole trap ($V \sim 10^{-8} \text{ cm}^3$) would require in principle only a very small MOT with loading times less than 0.1 seconds. However cloud overlap and a limited loading efficiency make longer loading times favorable. Also the atom density in the MOT changes with the MOT size. First, the density increases linearly with atom number up to $\sim 10^4$ atoms while later it becomes independent of it and is only determined by intensity, detuning and magnetic field gradient [78]. Figure 6.6 shows the number of atoms in the tightly focused dipole trap after 300 ms holding time as a function of the MOT loading time, which is proportional to the MOT atom number (inset in Figure 6.7). It can be seen that the atom number in the dipole trap saturates for longer loading times. Figure 6.7 shows the transfer efficiency dependent on MOT atom number. The transfer efficiency is defined as

$$\eta_{transfer} = \frac{N_{dipole}}{N_{MOT}} * 100\%,$$



(a) Transfer efficiency of the dipole-trap loading process depending on the MOT atom number. Atom numbers in the dipole trap were adjusted for the trap losses during the 300 ms holding time. Each data point shows the average value of 20 measurements, error bars indicate the standard deviation. The inset shows the MOT atom number increase with MOT-loading time.

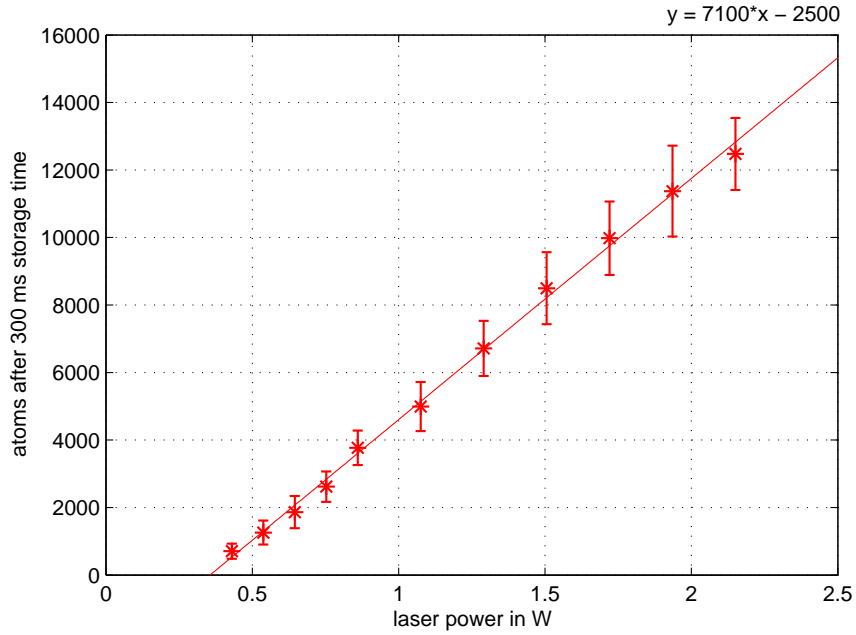
Figure 6.7:

where N_{dipole} is the atom number in the dipole trap at the end of the loading phase into the dipole trap and N_{MOT} is the MOT atom number at the end of the loading phase. Atom numbers in the dipole trap were determined by detecting the fluorescence of the excited atoms with the photomultiplier after 300 ms of holding time. A holding time of at least 100 ms is necessary to allow MOT atoms to leave the detection region. The dipole trap atom numbers are corrected for the losses during the holding time⁴. Generally, for larger dipole beam waist sizes by otherwise constant trapping potential, transfer efficiencies increase and can exceed 40% [90].

Role of the trap laser intensity

Increasing the intensity of the dipole laser translates directly into an increased potential depth. Higher capture velocities and reduced collisional loss probabilities lead to an increase in the number of trapped atoms. Measurements with CO_2 lasers indicate that a saturation power exists where atom numbers only marginally increase with increasing laser

⁴Losses were determined in a separate measurement under identical trapping conditions.



(a) Atom number in the dipole trap after 300 ms holding time vs. trap laser power. $N(300 \text{ ms}) = 7100 \cdot \text{atoms/W laser power}$. The offset on the x-axis can be attributed to atom loss during the 300 ms trapping time. Each data-point shows the average value of 20 measurements, error bars indicate the standard deviation.

Figure 6.8:

power [91]⁵. For our small and tight trap we did not observe this effect. Figure 6.8 shows the number of atoms in the dipole trap linearly increasing with laser power. The offset is due to the losses during the 300 ms holding time, which leads to a reduction of the initial atom number to about 7.5%.

6.3.4 Losses in the dipole trap

Several processes contribute to the loss of captured atoms: heating due to spontaneous emission, intensity fluctuations, collisions between the trapped atoms or with background gas constituents. Collisional processes dominate normally. Furthermore, in very deep traps ($\frac{U}{k_B T} \geq 10$) intensity fluctuations of the trap laser limit the lifetime considerably [82].

Atom loss from a FORT is well described by the differential equation [90]

$$\frac{dN}{dt} = -\gamma \cdot N - \beta' \cdot N^2 \quad (6.3.2)$$

⁵In the theoretical model of the authors this is the case when $\frac{U}{k_B T} > 4$, where U denotes the trapping potential and T is the average temperature of the trapped atoms.

where N is the atom number, γ is the loss rate due to background gas collisions⁶ and β' is the density-related loss coefficient due to collisions between the trapped atoms.

The volume-independent density loss rate coefficient β is then obtained by multiplication of the measured rate coefficient β' with the atom cloud volume V .

$$\beta = \beta' \cdot V \quad (6.3.3)$$

This volume depends on the atom temperature and the geometry of the confining potential. A model [90] can be derived under the assumption that the maximal cloud radius r and length z are determined by the condition that the potential energy $U(r, z)$ equals the average thermal energy $K_B T$.

For a single Gaussian beam trap with waist ω_0 and Rayleigh range z_R this leads to

$$\begin{aligned} z_c &= \frac{\sqrt{(1-\eta)\eta}}{\eta-1} \cdot z_R \\ r_c &= -\frac{\sqrt{-2\log(1-\eta)}}{2} \cdot \omega_0 \end{aligned} \quad (6.3.4)$$

with $\eta := \frac{K_B T}{U_0}$ and U_0 as the maximum of the trapping potential. Approximating the atom cloud volume as a cylinder gives

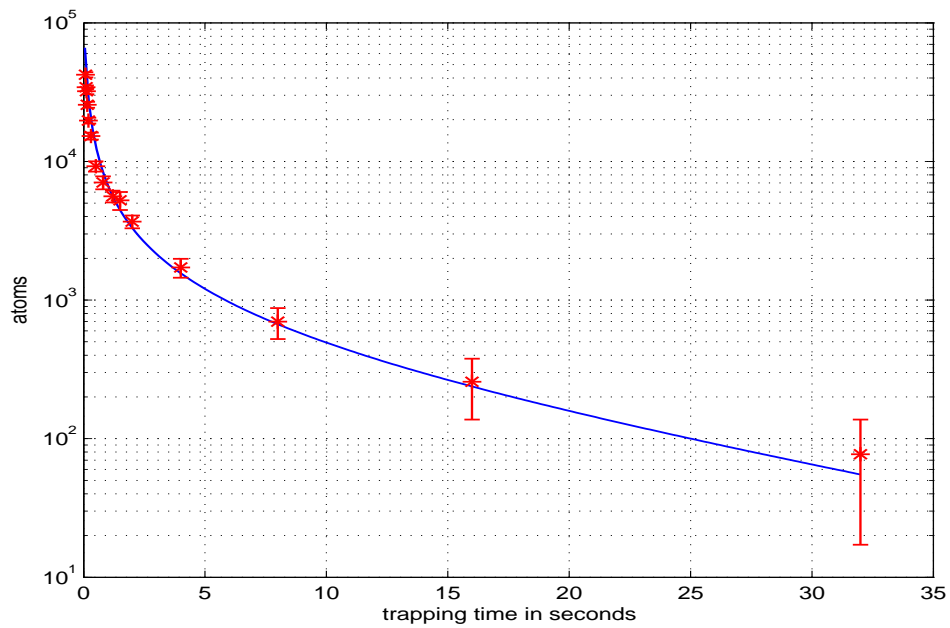
$$V = 2\pi r_c^2 z_c = \pi \log\left(\frac{1}{1-\eta}\right) \sqrt{\frac{\eta}{1-\eta}} \omega_0^2 z_R \quad (6.3.5)$$

Ground state trap loss collisions include hyperfine-changing and elastic collisions [14]. In case of hyperfine-changing collisions, atoms are lost if during the collision process the exit channel lies on a lower hyperfine level than the entrance channel. The energy difference of $h \cdot 6.8$ GHz for ^{87}Rb is much larger than the trapping potential of -70 MHz/W and is then distributed as kinetic energy over the colliding partners. This can be avoided by optical pumping of the atoms to the lowest energetic state, the hyperfine ground state ($F=1$), during the last 5 ms of the dipole loading phase.

Figure 6.9 shows a trap loss measurement and corresponding fit to the solution of eq. 6.3.2. The strong deviation from the purely linear loss model, especially for short holding times, shows that density-dependent two- and three-body collisions contribute strongly to the trap loss for tightly confined atom samples. Using the approximate volume of eq.6.3.5 and the parameters of the fit in figure 6.9, the density dependent loss coefficient is calculated as $\beta \sim 1.6 \cdot 10^{-15} \text{ cm}^3 \text{ s}^{-1}$. From this value we conclude that the losses occur primarily due to inelastic spin-dipole relaxation, where rate coefficients in the range of $[0.4 - 0.7] \cdot 10^{-15} \text{ cm}^3 \text{ s}^{-1}$ are predicted⁷ [146, 147]. Elastic collisions contribute not significantly as the deep trapping potential of -19 mK reduces the probability of cold atoms to escape.

⁶thermal Rb vapor and vacuum contaminants like He, Ne, Ar and H

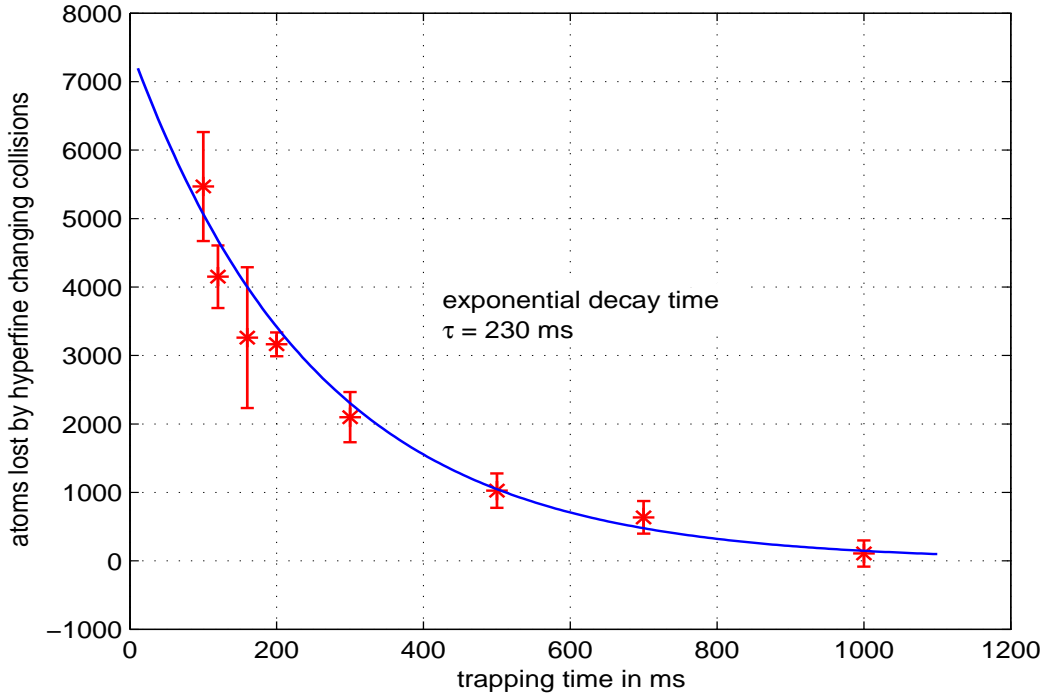
⁷In ^{87}Rb the coincidence between the singlet and triplet scattering lengths lead to a strong suppression of elastic spin exchange collisions.



Trap-loss measurement of atoms prepared in the lowest hyperfine ground state. The solid line shows a fit to the solution of eq. 6.3.2. The deep trapping potential of $U_0 = -19 \text{ mK}$ and the tight confinement leads to notable density dependent losses. Each data-point and error bar show the mean-value and standard deviation of 20 measurements.

Fit parameters are: $N_0 = 1.2 \cdot 10^5 \text{ atoms}$, $\gamma = 0.198 \text{ s}^{-1}$, $\beta' = 1.35 \cdot 10^{-4} (\text{atoms s})^{-1}$

Figure 6.9:



Atom number difference between two trap loss measurements where the atoms had been prepared initially in different hyperfine ground states ($F=2$ and $F=1$). The subtraction of the losses leaves only the contribution of the upper hyperfine ground state. All common, state independent contributions, like background gas collisions, subtract to zero. The fit (solid line) is based on the constant spin exchange loss rate model described in eq. 6.3.6 with exponential time constant $\tau = 230 \text{ ms}$. $U_0 = -17.8 \text{ mK}$

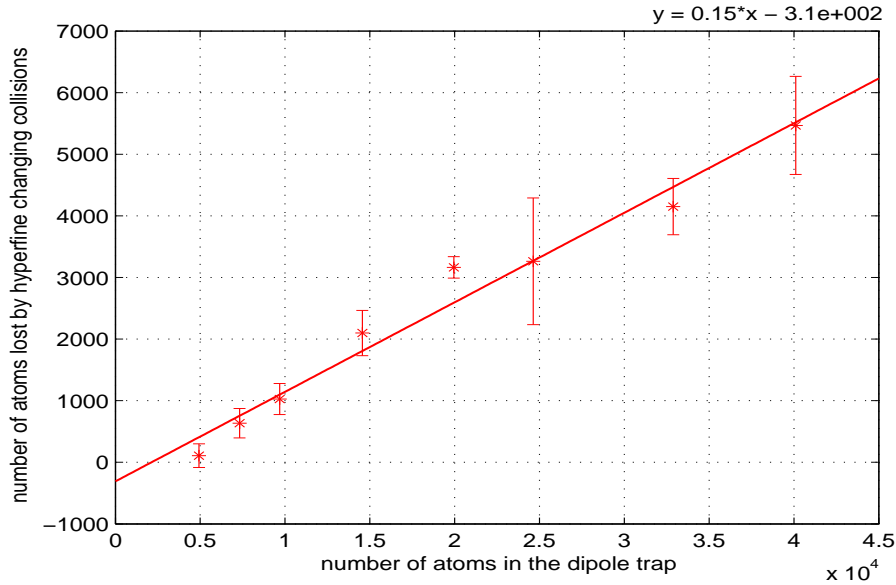
Figure 6.10:

Figure 6.10 shows the difference in atom loss of two trap loss measurements with identical trapping parameters but different initial preparation of the atomic sample. One sample is prepared in the $F=2$ hyperfine ground state, the other one optically pumped into the $F=1$ ground state. By taking the difference of the two loss curves, only losses which are dependent on the spin state contribute. All common, spin independent losses like background gas collisions subtract to zero. Assuming a rate equation model with a constant spin-exchange loss rate

$$\frac{dN}{dt} = -\alpha_{SE}N \quad (6.3.6)$$

gives an exponential decay time constant of $\tau = 1/\alpha_{SE} = 230 \text{ ms}$. Compared with the spontaneous photon scatter rate $\tau_{el} = 7 \text{ ms}$ the spin relaxation rate is 30 times slower. This is comparable with measurements of dipole trapped ^{85}Rb atoms, where relaxation rates up to a factor of 100 lower than the photon scatter rate have been found [149]⁸. Figure 6.11 shows

⁸For dipole laser detunings Δ large enough that the $^5P_{1/2}$ - $^5P_{3/2}$ fine-structure cannot be resolved, Raman scattering occurs at a rate ($\sim 1/\Delta^4$) [149].



Trap loss of atoms which were initially prepared in the F=2 hyperfine ground state vs. total atom number in the dipole trap. The ratio of atoms lost from the trap by hyperfine changing collisions to the total number of trapped atoms is 0.15. Data-points and error bars correspond to mean and standard deviation of 20 measurements.

Figure 6.11:

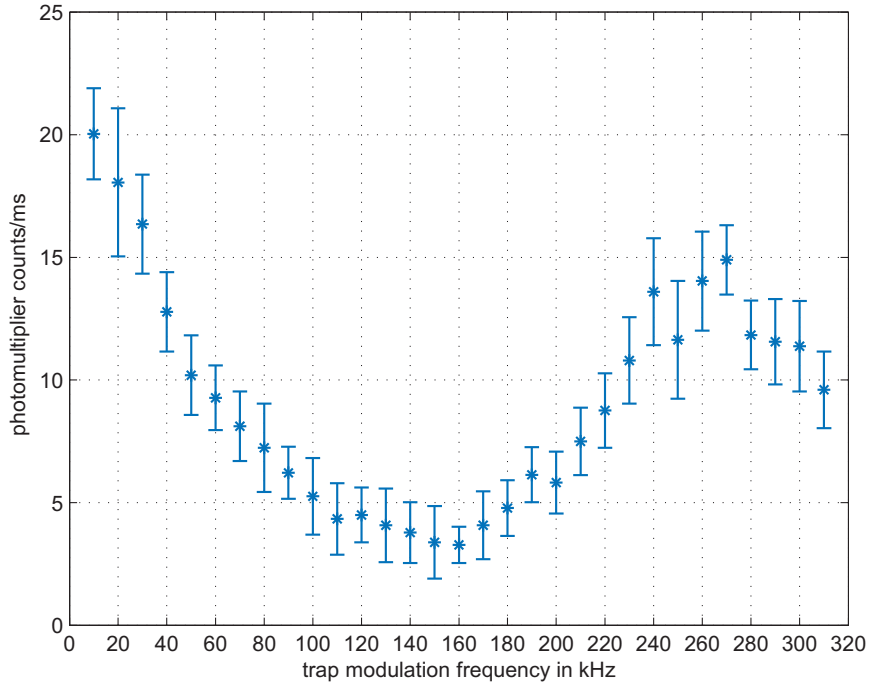
that the spin-state dependent atom loss in the tightly focused dipole trap is a constant fraction of 15% of the trapped atoms when the atoms are initially prepared in the F=2 hyperfine ground state.

6.3.5 Trap oscillation frequencies

The motional dynamics of atoms in a trap can be described by a harmonic oscillation with an associated oscillation frequency. Even for anharmonic potentials like the single Gaussian beam trap the harmonic approximation is justified, if the atomic sample is small compared to the waist size ω_0 and Rayleigh range $z_R = \frac{\pi\omega_0^2}{\lambda}$, i.e. provided that the thermal energy is much smaller than the optical potential, $\eta := \frac{K_B T}{U_0} \ll 1$.

Taylor expansion of the trapping potential $U(r,z)$ gives

$$U(r,z) = -U_0 \left[1 - 2 \left(\frac{r}{\omega_0} \right)^2 - \left(\frac{z}{z_R} \right)^2 \right] \quad (6.3.7)$$



(a) Periodic modulation of the trapping potential causes maximum trap-loss at twice the radial trap frequency. The trapping potential $U_0 = -17.8mK$, holding time is 400 ms, photomultiplier gate time 5 ms.

Figure 6.12:

and with the help of Hooke's law

$$U = -\frac{1}{2}kx^2 \quad (6.3.8)$$

$$\omega = \sqrt{\frac{k}{m}}$$

the radial and axial trap oscillation frequency can be calculated to:

$$\omega_r = \sqrt{\frac{4U_0}{m\omega_0^2}} \quad (6.3.9)$$

$$\omega_z = \sqrt{\frac{2U_0}{mz_R^2}}$$

In experiments trap frequencies can be measured by parametrically exciting the oscillations. This is done by amplitude modulation of the trapping laser or by fast switching of the trapping beams. Atom loss is then recorded as a function of modulation frequency or waiting time between the switching pulses [60].

The measurement shown in Figure 6.12 shows the remaining atoms after 400 ms trapping time as a function of the amplitude modulation frequency. A 720 mV d.c. control voltage modulated by a $\pm 10\text{mV}$ sine from a programmable function generator⁹ was applied to the modulation input of the AOM that controls the dipole trapping beam. This resulted in sufficient amplitude modulation to observe the frequency dependent loss spectrum. Trap-loss maximum occurs at 150 kHz which is equivalent to a radial trap frequency of $\omega_r = 2\pi \cdot 75\text{kHz}$.

With the optical power of 5.13 W and the measured trap frequency, eq.: 6.3.9 together with eq.: 4.3.2 and eq.: 4.3.6 allow the determination of the beam waist size and Rayleigh range:

$$\omega_0 = 5.4\ \mu\text{m}$$

$$z_R = 89\ \mu\text{m}$$

Compared with the values calculated by an optics-design program ($\omega_0 = 3.88\ \mu\text{m}$, $z_R = 45.8\ \mu\text{m}$, see Appendix B) the measured waist size and Rayleigh range are remarkably larger¹⁰. A calculation based on Huygens-Fresnel diffraction formulas [92] taking into account the beam truncation by the entrance aperture of the focusing objective results in a calculated waist size of $\omega_0 = 5.56\ \mu\text{m}$, in satisfactory agreement with the measured value.

6.4 Sample Temperature

The temperature is one of the main parameters for characterizing a trapped sample. Temperature determines the filling factor of the trap and combined with information about the atom number the sample density can be inferred.

The principle of measurement has been adapted from the MOT temperature estimation. Atoms are released from the trap and allowed to expand ballistically for a given time. Then the rate of cloud-expansion is measured for several time-steps and the temperature determined from the expansion velocity.

This principle works well for large atom numbers eg. in a MOT where the cloud can be imaged on a standard CCD-camera. For the reduced atom numbers in the small dipole trap an intensified CCD-camera (ICCD) would be required. Without ICCD camera available, we used the photomultiplier and a fixed aperture.

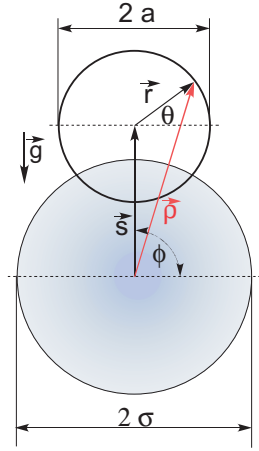
6.4.1 Imaging through a fixed aperture

As a photomultiplier cannot distinguish between different cloud sizes, the limited aperture of the detection region was used to get a quantitative expansion signal. The expanding cloud with Gaussian density distribution is imaged through a circular aperture and the fluorescence signal recorded after a certain time. Due to the cylindrically shaped detection region defined

⁹Stanford Research SRS DG345

¹⁰Oslo LT from Lambda Research Corporation

Oslo LT uses a paraxial ABCD matrix method to calculate Gaussian beam parameters.



Sketch of the cloud imaging geometry. The shaded circle represents the Gaussian density distribution of the expanding and falling atom cloud with $1/e^2$ radius σ . The smaller circle with radius a shows the circular aperture which defines the imaging region.

Figure 6.13:

by a circular aperture, the count signal decays as the atom cloud starts to extend beyond the detection region. In the following the dynamics of the temperature dependent fluorescence count signal is modeled and fit to the experimental data points.

In Figure 6.13 a geometrical sketch of the problem is shown. The shaded circle depicts the Gaussian density distribution of the expanding and falling atom cloud with $1/e^2$ intensity radius σ , and the smaller circle shows the circular aperture with radius a . Initially the center of the atom cloud coincides with the center of the detection region but gravitation leads to increased separation \vec{s} over time. The vector $\vec{\rho}$ which points from the center of the cloud to an arbitrary point inside the detection region can be written as

$$\vec{\rho} = \vec{r} + \vec{s} = (r \cdot \cos(\theta) + s \cdot \cos(\phi))\vec{e}_x + (r \cdot \sin\theta + s \cdot \sin(\phi))\vec{e}_y \quad (6.4.1)$$

$$|\vec{\rho}|^2 = s^2 + r^2 + 2sr \cdot \cos(\phi - \theta) \quad (6.4.2)$$

The signal S of the photomultiplier is proportional to the integral of the atomic density distribution¹¹ over the aperture with radius a .

$$S = S_0 \int_0^{2\pi} \int_0^a e^{-\left(\frac{\rho^2}{2\sigma^2}\right)} \cdot r \, dr d\theta \quad (6.4.3)$$

A pinhole inside a spatial filter assembly limits the detection region radially to $a = 18 \mu\text{m}$ around the trap center. In longitudinal direction the imaging region is not restricted. Inserting ρ^2 from equation 6.4.2 gives

$$S = S_0 \int_0^{2\pi} \int_0^a e^{-\left(\frac{r^2}{2\sigma^2}\right)} e^{-\left(\frac{s^2}{\sigma^2} + \frac{sr}{\sigma^2} \cos(\phi - \theta)\right)} \cdot r \, dr d\theta \quad (6.4.4)$$

¹¹The fluorescence light distribution is assumed to be proportional to the atom number.

The angle ϕ is equal to $\pi/2$ in fig. 6.13 but can be set arbitrarily since $\phi - \theta$ is running through all values $[0; 2\pi]$; here for simplicity we use $\phi = 0$

$$S = S_0 \int_0^{2\pi} \int_0^a e^{-\left(\frac{r^2}{2\sigma^2}\right)} e^{-\left(\frac{r^2}{2\sigma^2} + \frac{sr}{\sigma^2} \cos(\theta)\right)} \cdot r dr d\theta \quad (6.4.5)$$

Free thermal, isotropic expansion of the atom cloud dictates that the cloud radius¹² σ follows

$$\sigma^2 = \sigma_0^2 + \frac{k_B T}{m} \cdot t^2 \quad (6.4.6)$$

where σ_0 is the initial width of the cloud, m the mass of Rb, T the atom temperature and t the free expansion time. Under gravity the atom cloud moves the distance

$$|\vec{s}| = \frac{g}{2} \cdot t^2 \quad (6.4.7)$$

with $g = 9.81 \text{ m/s}^2$ causing decentered imaging.

Combining equation 6.4.5 with 6.4.6 and 6.4.7 the final expression for the photomultiplier count signal can be written as:

$$S(t) = S_0 e^{-\left[\frac{g^2 t^4}{8(\sigma_0^2 + k_B T/m \cdot t^2)}\right]} \int_0^{2\pi} \int_0^a e^{-\left(\frac{r^2}{2(\sigma_0^2 + k_B T/m \cdot t^2)}\right)} e^{-\left(\frac{g t^2}{2(\sigma_0^2 + k_B T/m \cdot t^2)} r \cos(\theta)\right)} \cdot r dr d\theta \quad (6.4.8)$$

From equation 6.4.5 the expression for the concentric geometry follows immediately by setting $s = 0$.

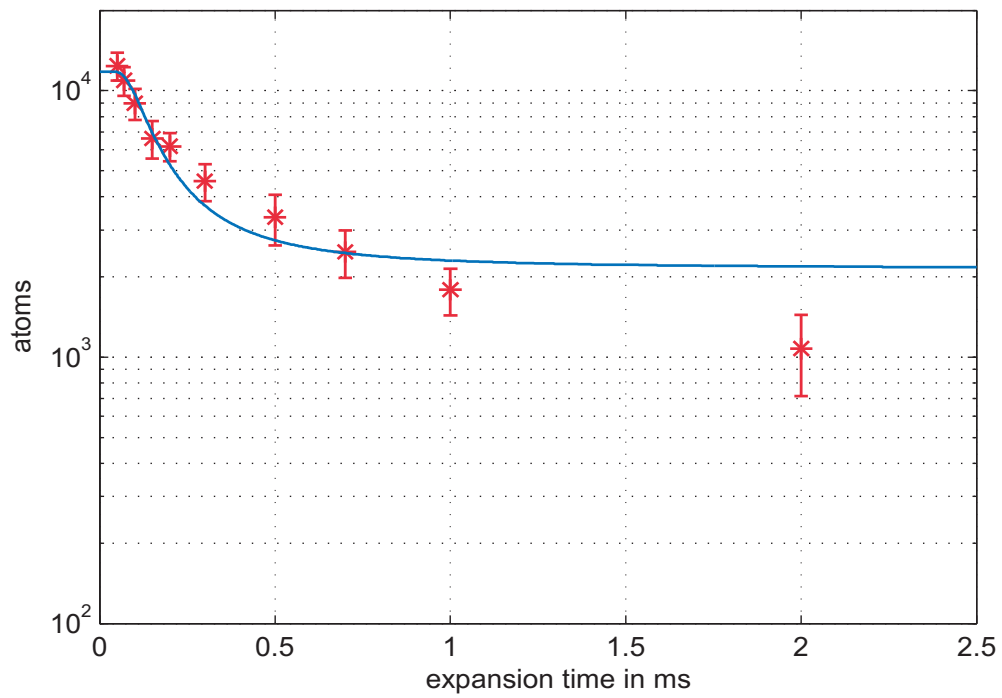
$$S = S_0 \int_0^{2\pi} \int_0^a e^{-\left(\frac{r^2}{2\sigma^2}\right)} \cdot r dr d\theta = S_0 \left[1 - e^{-\left(\frac{a^2}{2\sigma^2}\right)}\right] \quad (6.4.9)$$

Figure 6.14 shows a fit of equation 6.4.8 to a measured data set from the photomultiplier. Fit-parameters are the atom number upon release, the temperature of the sample and a constant offset accounting for background counts. Initial width of the atom cloud is set to $\sigma_0 = 2 \mu\text{m}$ whereas the waist size of the trap is $5.4 \mu\text{m}$. Although the initial cloud extension is dependent on temperature, the expanded cloud extension is largely dominated by thermal expansion (e.g. $\bar{v}_{thermal} = 150 \mu\text{m/ms}$ for a $100 \mu\text{K}$ cold sample). By treating the initial cloud size as a constant, a slight systematic error in the estimation of the temperature is introduced. Compared with the statistical uncertainties of the measured data, this error is insignificant for the overall accuracy of the method and can be neglected.

In figure 6.15 the temperature is measured after 1 second of holding time. In this case the increased storage time allowed a longer evaporation process and thus lead to a lower temperature of $53 \mu\text{K}$ compared to the previous measurement with otherwise unchanged parameters.

For longer expansion times all measurements show lower values than predicted by the isotropic thermal expansion model. This is a systematic observation and may be explained by anisotropic expansion of the cylindrically symmetric, elongated atom cloud ($\frac{\omega_z}{\omega_r} = 0.04$).

¹²The cloud radius σ is defined as the 1/e half-width of the normalized Gaussian density distribution



Temperature estimation fit (solid line) for atoms released after 400 ms holding time in the dipole trap. $T=104 \mu\text{K}$, detection gate time is 1 ms, detuning of the detection laser -4 MHz

Figure 6.14:

Anisotropic expansion after release from the trap, a well known feature of Bose-Einstein condensates and degenerate Fermi gases, is indicative of hydrodynamic behavior [139, 140]. In the hydrodynamic regime, the gas behaves as a uniform fluid governed by the Euler equation for the fluid-velocity field [140]. The anisotropy of the expanded gas reflects the anisotropy of the pressure force which is stronger in the direction of tighter confinement. For a thermal gas the particle dynamics depend on the mean free path at equilibrium. At low densities (collisionless regime), where the mean free path is large compared to the dimension of the cloud, the atomic motion is described by a single-particle Hamiltonian and expansion is isotropic. When the mean free path is reduced to a value smaller than the sample size, crossover to the hydrodynamic regime occurs.

Detection itself which lasts for 1 ms, essentially freezes the atomic motion with the radiation pressure compensated MOT beams¹³ and therefore should not attribute to a systematic effect. Calculation of the mean free path in the trap center for a uniform gas at a density of $n_0 = 8 \cdot 10^{14}$ atoms/cm³ (see 6.4.2) gives

$$\lambda_0 = \frac{1}{\sqrt{2}n_0\sigma} = 1.3 \mu m,$$

where $\sigma = 8\pi a^2$ is the elastic s-wave cross section with $a = 98.98(4)a_0$ the scattering length [141]. The elastic collision rate in the center of the trap is [142]

$$1/\tau_c = \frac{4\sqrt{2}\pi}{5}n_0\sigma v_{th} \approx 1.2 \cdot 10^5 s^{-1} \quad (6.4.10)$$

with the thermal velocity $v_{th} = (8k_B T/\pi m)^{1/2}$. From the axial and radial size parameters $l_i = (2k_B T/m\omega_i^2)^{1/2}$, $i \in \{r, z\}$ follows that in axial direction we are in the hydrodynamic regime and radially in the collisionless

$$\lambda_0/l_r \simeq \omega_r \tau_c \simeq 3.7$$

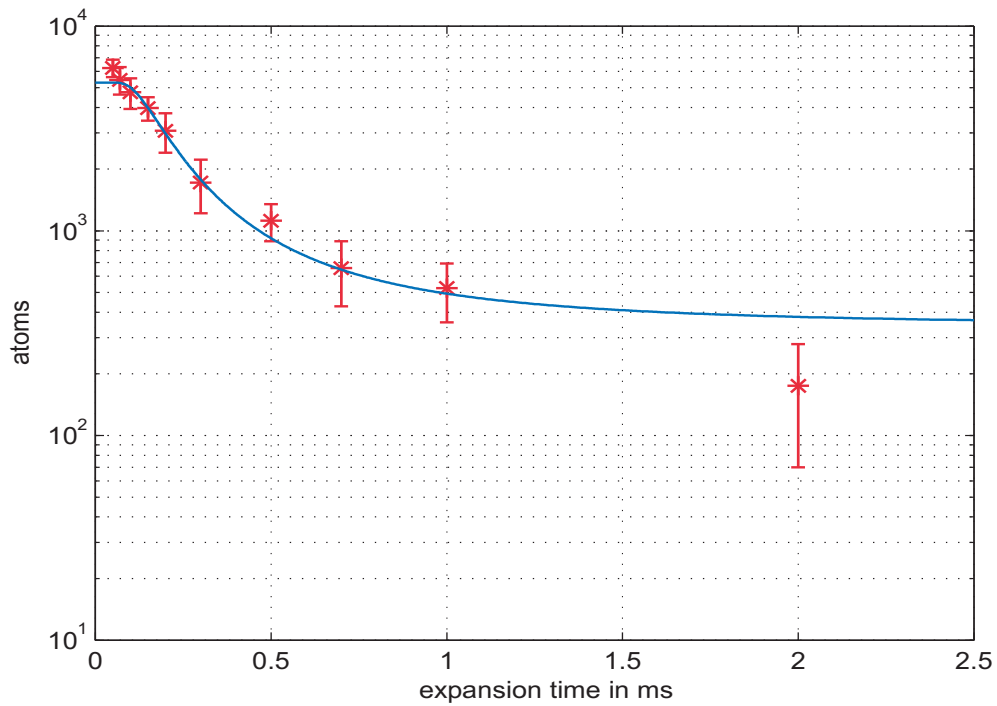
$$\lambda_0/l_z \simeq \omega_z \tau_c \simeq 0.11$$

The expansion of the cloud is therefore in an intermediate regime between collisionless expansion and hydrodynamic condition. Axially the cloud cools for a short time as it expands until no more collisions occur, resulting in a slower than expected expansion. Energy conservation then demands a faster radial expansion. This affects time-of-flight imaging of dense atom clouds, where the faster radial expansion causes a faster than expected rate of atoms leaving the detection region.

In Figure 6.15 the temperature is measured after 1 second of holding time. In this case the increased storage time allowed a longer evaporation process and thus lead to a lower temperature of $53 \mu K$ compared to the previous measurement with otherwise unchanged parameters.

This temperature estimation method works well for small to intermediate sized atom samples and requires only a photomultiplier and suitable aperture to define the detection region.

¹³The magnetic field is zero during detection



Temperature estimation fit for a holding time of 1 second. Compared to the measurement in Fig. 6.14, the temperature is lower ($T=53 \mu K$). Evaporation occurs over a longer period with more high energetic atoms ejected. Detection time is 1 ms, detuning of the detection laser -4 MHz.

Figure 6.15:

The primary function of the aperture is stray light reduction and thus the size of the aperture has to be selected accordingly. No additional modification to the optical setup is necessary and therefore implementation is straight-forward. Microsecond-precision timing is however required as the detection light pulse and the photomultiplier gate need to be synchronized with the release of the atoms.

6.4.2 Density of trapped atoms

During loading in a MOT or optical molasses, light-assisted collisions typically limit atom densities to about 10^{12} atoms/cm³. Experiments in crossed dipole traps [93, 94] and surface microtraps [95] unexpectedly revealed much higher densities $n_0 > 10^{14}$ atoms/cm³ which together with forced evaporative cooling allowed the production of *all-optical BEC* [84, 86].

Taking the data from measurement 6.14 with $N_0 = 10^4$ atoms, $T = 104 \mu\text{K}$, $U_0 = 8.7 \text{ mK}$, $\bar{\omega} = (\omega_r^2 \cdot \omega_z)^{1/3} = 2\pi \cdot 18.7 \text{ kHz}$ and the trap dimensions from the measured radial trap frequency, the volume occupied by the trapped sample calculates to (eq.: 6.3.5)

$$V = 1.2 \cdot 10^{-11} \text{ cm}^3$$

and the peak density reaches

$$n_0 = 8.6 \cdot 10^{14} \text{ atoms/cm}^3$$

Taking into account the expression for the phase space density inside a harmonic trap [98] quantum degeneracy occurs when

$$\rho = N \left(\frac{\hbar \bar{\omega}}{k_B T} \right)^3 = \zeta(3)^3 \approx 1.737, \quad (6.4.11)$$

where $\bar{\omega}$ is the geometrical average trapping frequency and ζ is the Riemann zeta function. Given the parameters above, onset of condensation occurs in a harmonic trap at a critical temperature¹⁴ of

$$T_c = \frac{1}{k_B} \left[\hbar \bar{\omega} \left(\frac{N}{\zeta(3)} \right)^{1/3} - \frac{\zeta(2)}{6\zeta(3)} \hbar (\omega_z + 2\omega_r) \right] = 16.7 \mu\text{K}$$

and the phase space product ρ reaches $1/167$, which corresponds to a phase space density of $1/500$ if we assume an equal distribution of spin projections.

This cold-atom densities are among the highest so far reported for incoherent matter. Comparable measurements on Yb-atoms in a crossed FORT [94] and on Rb-atoms in a holographic

¹⁴The first term inside the brackets is the transition temperature in the thermodynamic limit, the second term accounts for finite-size effects [138].

atom trap showed densities of up to $1.8 \cdot 10^{15}$ atoms/cm³ [103]. In dimple traps¹⁵ [97], strong density enhancements up to 10^{14} atoms/cm³ have been measured [95] and are crucial for the all-optical generation of BEC [96].

6.5 Trap-State Spectroscopy

Energy selective excitation of trapped atoms combined with fluorescence detection, which we refer to as *trap-state spectroscopy*, is a valuable tool to gain “in-vivo” information about the trapped atom sample. For traps, where the light shift of the atomic energy levels is large compared to the natural linewidth of the excited state or the probe-laser linewidth, the population distribution can be measured. From this the sample temperature and light-shift of the excited state can be inferred. Additionally time resolved detection of the number of atoms which escape from the trapping potential allows for the estimation of evaporation rates. Hence trap-state spectroscopy is a highly sophisticated tool for characterizing and investigating a trapped atomic sample. This will be shown in the measurement of thermal distributions and an anharmonic potential presented at the end of this chapter.

6.5.1 3D Harmonic Oscillator Model

The harmonic oscillator approximation of real trapping potentials, together with the assumption of noninteracting particles, is of great practical importance. It makes tractable the calculation of thermodynamic properties of confined quantum gases at equilibrium conditions while retaining the essential physics.

The energy of a particular 3D harmonic oscillator state can be written as

$$E_{n_x n_y n_z} = \hbar\omega_x(n_x + 1/2) + \hbar\omega_y(n_y + 1/2) + \hbar\omega_z(n_z + 1/2), \quad (6.5.1)$$

where $n_i = 0, 1, 2, \dots$ is the vibrational quantum number of the degree of freedom $i = x, y, z$ and ω_i is the corresponding angular oscillation frequency.

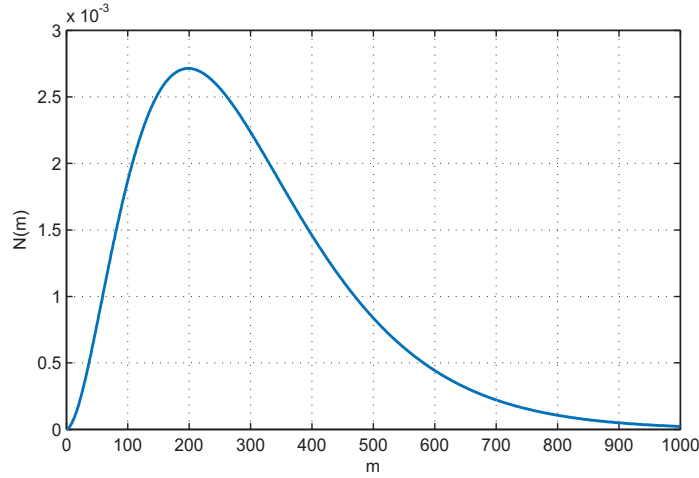
In case of an isotropic oscillator where $\omega = \omega_x = \omega_y = \omega_z$, 6.5.1 simplifies to

$$E_m = \hbar\omega(n_x + n_y + n_z + 3/2) \quad (6.5.2)$$

and the energy can be expressed in integral units of $\hbar\omega$. In total $\frac{1}{2}(m+2)(m+1)$ independent states with energy $m\hbar\omega$ are possible [99].

The total occupation number of all states with energy E_m is given by the Bose-Einstein

¹⁵A dimple trap is an additional optical microtrap which loads from a larger trapped atomic reservoir to increase locally the potential depth and elastic collision rate but has only marginal effects on the reservoir thermodynamics.



Occupation number distribution of a 3D-harmonic oscillator according to eq. 6.5.3.

Figure 6.16:

distribution multiplied by the degeneracy of the energy levels:

$$N_m = \frac{(m+2)(m+1)}{2(Ce^{\beta E_m} - 1)}. \quad (6.5.3)$$

Here $\beta := \frac{1}{k_B T}$ and C is a normalization constant which is chosen such that the total number of particles N is obtained by summation over all particle states¹⁶

$$N = \sum_{m=0}^{\infty} \frac{(m+2)(m+1)}{2(Ce^{\beta E_m} - 1)}. \quad (6.5.4)$$

Figure 6.16 shows an example of the occupation number distribution (6.5.3) with $\frac{\hbar\omega}{k_B T} = 1/100$ and $N = 1000$.

For systems with large numbers of particles, and when the energy level spacing of the trapping potential is much smaller than the thermal energy $\hbar\omega \ll k_B T$, the sum over the quantum states can be replaced by integrals over the phase space¹⁷. This leads to a density of states where the individual level structure is smoothed out

$$g(\varepsilon) = \frac{dG(\varepsilon)}{d\varepsilon}, \quad (6.5.5)$$

and where $G(\varepsilon)$ denotes the total number of states with energy less than ε . Hence $g(\varepsilon)d\varepsilon$ gives the number of quantum states with energy between ε and $\varepsilon + d\varepsilon$. For a d-dimensional

¹⁶From this equation the unknown C can be determined and then inserted in eq. 6.5.3

¹⁷For Bose-Einstein condensates it is only a good approximation for the excited states contribution. The ground state has to be treated separately.

harmonic oscillator the density of states [100] calculates to:

$$g(\varepsilon) = \frac{\varepsilon^{d-1}}{(d-1)! \prod_{i=1}^d \hbar \omega_i} \quad (6.5.6)$$

which in 3 dimensions gives:

$$g(\varepsilon) = \frac{\varepsilon^2}{2\hbar^3 \omega_x \omega_y \omega_z}. \quad (6.5.7)$$

In this continuum approximation, eq. 6.5.4 for the total number of particles becomes

$$N = \int_0^\infty d\varepsilon n(\varepsilon) = \int_0^\infty d\varepsilon g(\varepsilon) \frac{1}{C e^{\beta\varepsilon} - 1} \quad (6.5.8)$$

with the atom number distribution function

$$n(\varepsilon) = \frac{\varepsilon^2}{2\hbar^3 \omega_x \omega_y \omega_z} \cdot \frac{1}{C e^{\beta\varepsilon} - 1} \quad (6.5.9)$$

6.5.2 Adaptation to the Gaussian Potential

Atoms with energy $\varepsilon \ll U_0$ are well described by the harmonic model due to their confinement near the bottom of the potential well. For higher energetic atoms and larger filling ratios of the trap the harmonic approximation becomes increasingly inaccurate.

The real trapping potential is radially gaussian, while the axial z-direction is lorentzian. To simplify the calculation, and following Ref. [101], we approximate the potential in z-direction to be also gaussian with 1/e radius λ .

Expressed in cylindrical coordinates this yields

$$U(r, z) = U_0 (1 - e^{-2r^2/\omega_0^2 - z^2/\lambda^2}) \quad (6.5.10)$$

The geometric effect of the trapping potential is reflected in the density of states.

To obtain the density of states, the spatial integration

$$g(\varepsilon) = \frac{2\pi(2m)^{3/2}}{h^3} \int_{U \leq \varepsilon} \sqrt{\varepsilon - U(\mathbf{r})} d^3r \quad (6.5.11)$$

needs to be evaluated over all values \mathbf{r} where $U(\mathbf{r}) \leq \varepsilon$ [102].

O'Hara and coworkers [101] derived an analytical expression for this integral and the Gaussian potential given in 6.5.10. It can be written as a product of the density of states for a harmonic oscillator potential

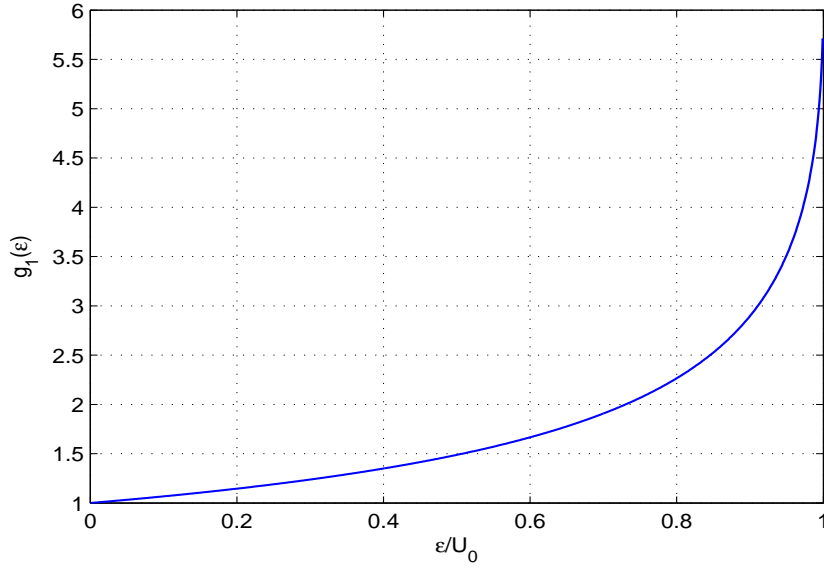
$$g_{ho}(\varepsilon) = \frac{\varepsilon^2}{2\hbar^3 \omega_x \omega_y \omega_z}$$

and a factor, which accounts for the anharmonicity, given by

$$g_1(\varepsilon) = \frac{\alpha^{3/2}(1-\delta)^{1/2}}{\delta^2} \frac{16}{\pi} \int_0^1 u^2 \sqrt{e^{\alpha(1-u^2)} - 1} du \quad (6.5.12)$$

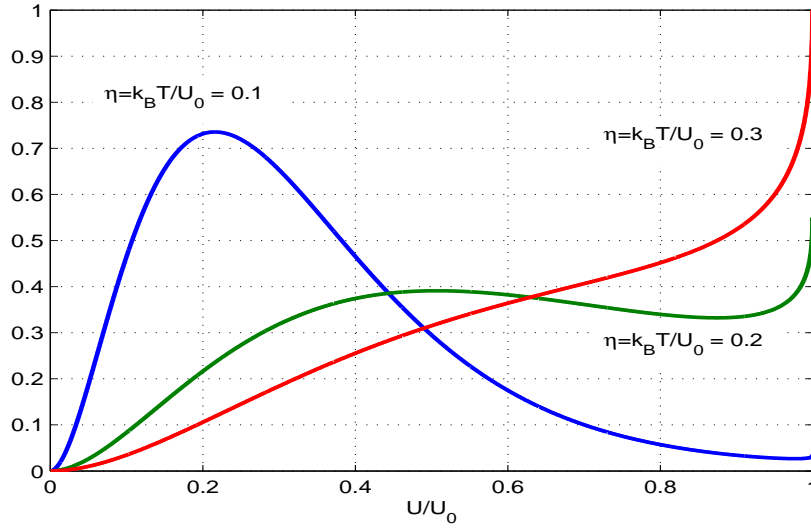
with $\alpha := -\log(1-\delta)$ and $\delta := \varepsilon/U_0$.

Figure 6.17 shows the Gaussian anharmonicity factor $g_1(\varepsilon/U_0)$ as a function of the particle energy normalized to the potential depth U_0 . This density of states for Gaussian trapping potentials, $g_{Gauss}(\varepsilon) = g_1(\varepsilon) \cdot g_{ho}(\varepsilon)$, will be used in the interpretation of spectroscopic measurements on the trapped atom samples presented in the following section.



(a) Gaussian potential correction factor to the density of states of a 3-dimensional harmonic oscillator

Figure 6.17:



(a) Calculated shape of the trap spectrum proportional to the total number of atoms with a certain energy U in a Gaussian trapping potential of depth U_0 , for $\eta=0.1$ (blue), $\eta=0.2$ (green) and $\eta=0.3$ (red curve)

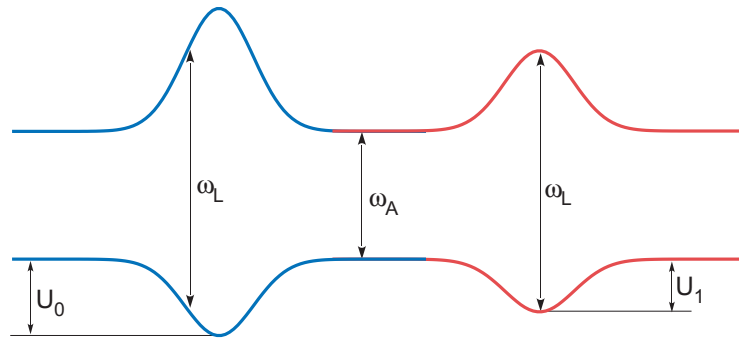
Figure 6.18:

In the regime where $\eta = 0.01 - 0.3$ the shape of the trap spectra changes notably as can be seen in Figure 6.18. This sensitivity to the thermal energy helps in the estimation of the parameters from the fitted data.

6.5.3 Measurements

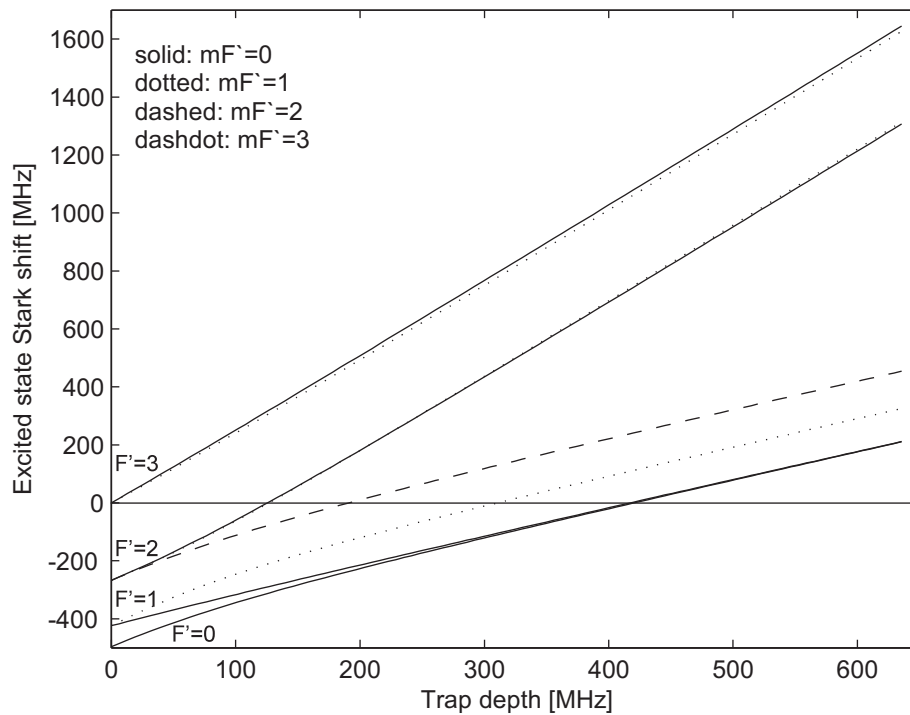
Determination of the total light shift

With knowledge of the ground state trapping potential and by comparison with the energy dependent population spectra it is possible to determine the contribution of the excited states light-shift for a specific dipole laser wavelength and polarization. During spectroscopy only a specific class of atoms gets excited for which the combined light shift of ground and excited state equals the probe-laser detuning. In our experiments the light shifts are much larger than the natural linewidth of the excited state (6 MHz) or the detection laser linewidth (~ 100 kHz). Figure 6.19 shows a schematic of the spatial dependence of the energy levels involved for two different levels of trap laser power.



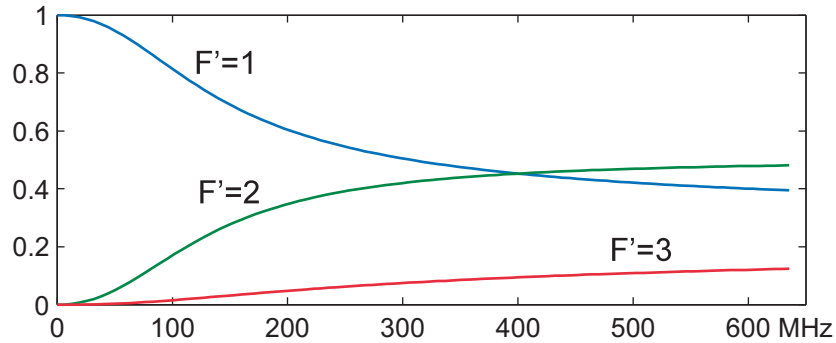
(a) Spatial energy dependence of the ground and excited state for two different trap power levels. The frequency of the probe laser is ω_L and ω_A is the transition frequency of the free-atom.

Figure 6.19:



Calculation of light induced level shifts for the $^{87}\text{Rb } 5S_{1/2} F=2 \rightarrow 5P_{3/2} F'=0,1,2,3$ transition. Energy shifts are given in MHz and include the ground state light-shift. The x-axis range corresponds to [0-10] W of dipole laser power. [Courtesy of M. Koschorreck]

Figure 6.20:



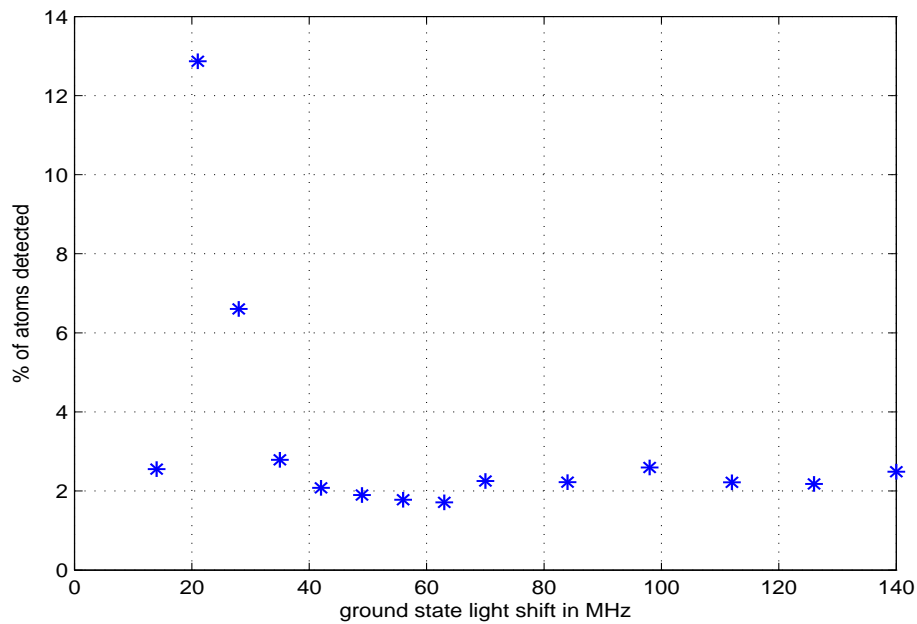
Change of the character of the $F' = 1, m_{F'} = 1$ magnetic state from a bare state to a superposition of different hyperfine states, all with $m_{F'} = 1$, caused by the coupling of the dipole light. The x-axis shows the strength of the trapping potential in MHz and corresponds to [0-10] W of dipole laser power.[Courtesy of M. Koschorreck]

Figure 6.21:

A calculation of the energy level shifts of the excited state is shown in figure 6.20 [150]. It can be seen, that magnetic sub-states of the same hyperfine state are shifted differently with increasing trapping potential¹⁸. When the light shifts reaches the order of the excited state hyperfine splittings (> 100 MHz), several hyperfine states couple and state mixing occurs, as can be seen in Fig.6.21 [150].

One method to measure the light shift is the following: In the experiment the detection laser frequency ω_L is +78 MHz detuned to the high frequency (blue) side with respect to the free atom resonance ω_A . The trap laser power is set to a power level where the potential depth U_0 is larger than the detuning and the fluorescence of the trapped atoms is recorded for 1 up to 10 ms. The trap laser power is reduced and the detection procedure repeated until no atoms are detected anymore. If the total frequency shift on the atomic transition becomes less than the detection laser detuning, all atoms will be quickly heated out of the trap by the then blue detuned detection laser. In contrast, if the laser frequency is smaller than the light-shift, atoms will be cooled.

¹⁸This is caused by the coupling of the excited state to various other states.

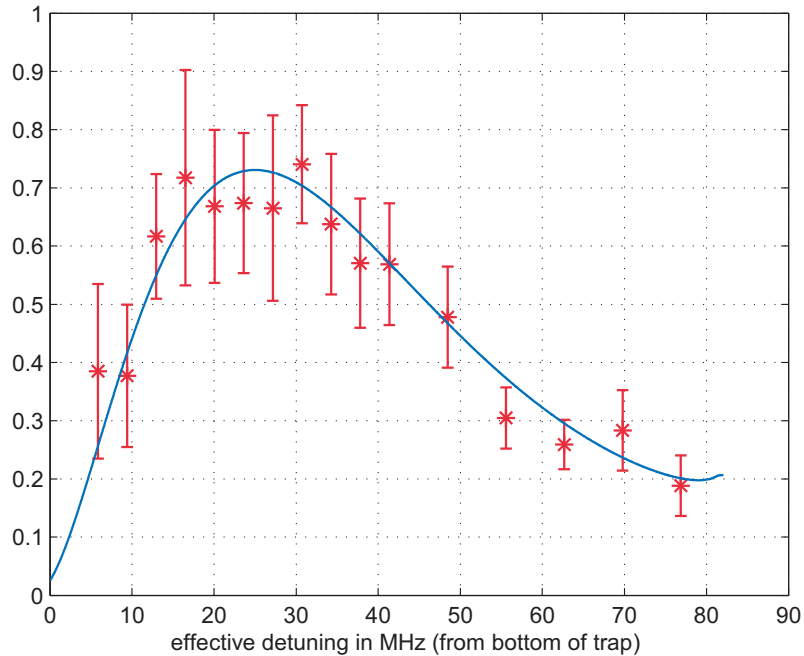


(a) Detection of trapped atoms after 300 ms holding time with a probe-laser detuning of +78 MHz. The ordinate shows the percentage of atoms detected by excitation of trapped atoms and fluorescence measurement. At 400 mW laser power, which equals a ground state potential of 28 MHz, the atoms are heated out of the trap. Photomultiplier gate time for detection is 10 ms.

Figure 6.22:

Figure 6.22 shows the corresponding measurement. According to a calculated energy spectrum, which reproduces the peak in fig. 6.22, the trap power where the atoms are heated out of the trap is around 400 mW or equivalent a ground state frequency shift of 28 MHz. This leaves a 50 MHz contribution from the excited state. Therefore the ground state contributes 36% and the excited state 64% to the total light shift at 1030 nm for the $F = 2 \rightarrow F' = 3$ transition.

Energy distribution



Energy spectrum of a trapped atom sample. The solid line shows a fit of an energy distribution with average thermal energy equal to 14% of the trap depth (86 MHz). Holding time is 300 ms, detection time 10 ms. Each data-point indicates the mean of 30 measurements, error bars the standard deviation.

Figure 6.23:

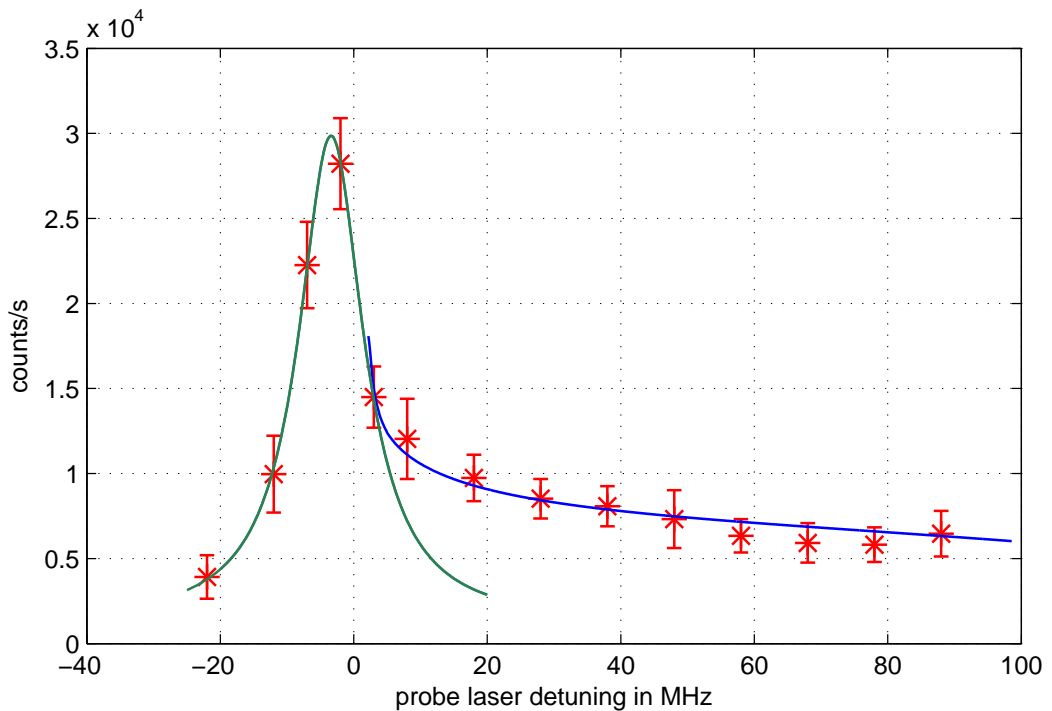
Figure 6.5.2 shows the energy distribution of a trapped sample after 300 ms of holding time. The optical potential at the trap center is $U_0 = 86$ MHz. The frequency of the detection laser, in this case the horizontal MOT beam, is fixed at +78 MHz relative to the free atom resonance. Repumper light was added for increased detection efficiency. The measurement procedure is the following: Trap laser power is stepwise reduced from 1200 mW to 200 mW and for each power level fluorescence from the trapped atoms is recorded for 10 ms. This results in a variable effective detuning of the probe laser depending on the light shift (see figure 6.19) which is proportional to the trap laser power. To minimize the effect that the atom numbers in the dipole trap are different for each power setting¹⁹, the atom numbers obtained by detection of the trapped atoms are divided by the total atom number in the trap for the specific dipole power level. The blue curve shows a fit according to the Gaussian energy distribution model 6.5.2 convoluted with the natural linewidth of the excited state.

¹⁹Detection in the trap after 300 ms holding time and +78 MHz detuning gives atom numbers from ~ 50 atoms for 200 mW of dipole light power to ~ 400 atoms for 1200 mW.

From the fit an average potential energy²⁰ per trapped atom of $\eta = \frac{k_B T}{U_0} = 0.14$ is determined with an anharmonicity factor of $g_1(0.14) = 1.097$ (see eq. 6.5.12).

This measurement procedure, with fixed detuned detection laser and stepwise reduction of the trap laser power, leads to lower heating by intensity noise compared to the case where the trap depth is held constant and the detection laser detuning is changed. In this regime, the higher energetic trap states are less populated when compared with the energy spectra of the following paragraph.

Occupation of high energetic states



Trap state occupation close to the edge of the potential. The peak close to zero detuning is the free atom resonance of unbound particles. The average thermal energy of the atoms is $\eta = \frac{k_B T}{U_0} = 0.26$ with $U_0 = 230$ MHz. Holding time is 300 ms, detection time 10 ms. Note that the detuning axis is inverted relative to that of Fig. 6.23.

Figure 6.24:

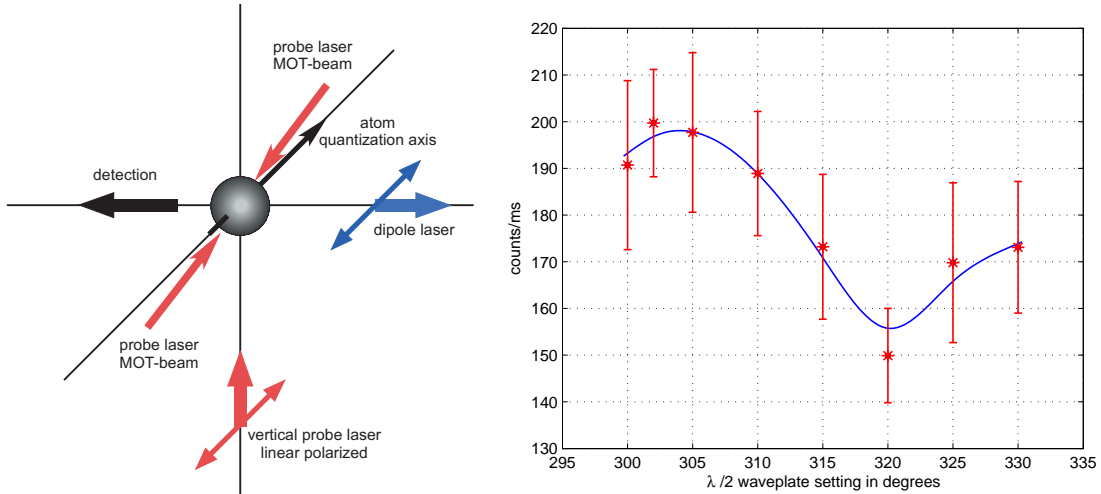
The high elastic collision rate of the very dense trapped samples and heating from laser intensity-noise (see 5.1.1) causes atoms to gain enough energy to occupy high lying trap states or even to evaporate. In the spectra this can be seen as fluorescence at small or even zero detuning from the free atom resonance.

²⁰Strictly speaking a thermal distribution is not possible for finite trap depths because the highest energetic atoms evaporate. However if the average energy per trapped atom is much smaller than the trapping potential most collisions redistribute the energy thus leading to a quasithermal equilibrium.

In figure 6.24 the spectrum shows clearly the increase of the atom number distribution close to the trap edge. The dark line shows the fit of the Gaussian number distribution model with $\eta = 0.26$, $g_1(0.26) = 1.199$ (see eq. 6.5.12) and $U_0 = 230$ MHz. Fluorescence detection lasted for 10 ms, the holding time was 300 ms. The light-gray line is a fit of a Lorentzian lineshape function with a full width of $\sim 2\Gamma$ and centered at a detuning of $\Delta = -\frac{\Gamma}{2}$, typical for free atom detection with a single MOT-beam pair (see fig.6.3).

One sees, that the measured energy distribution is well described by the combination of the two contributions, and the effect of the Gaussian trap potential is clearly visible in the increasing atom number towards the edge of the trap.

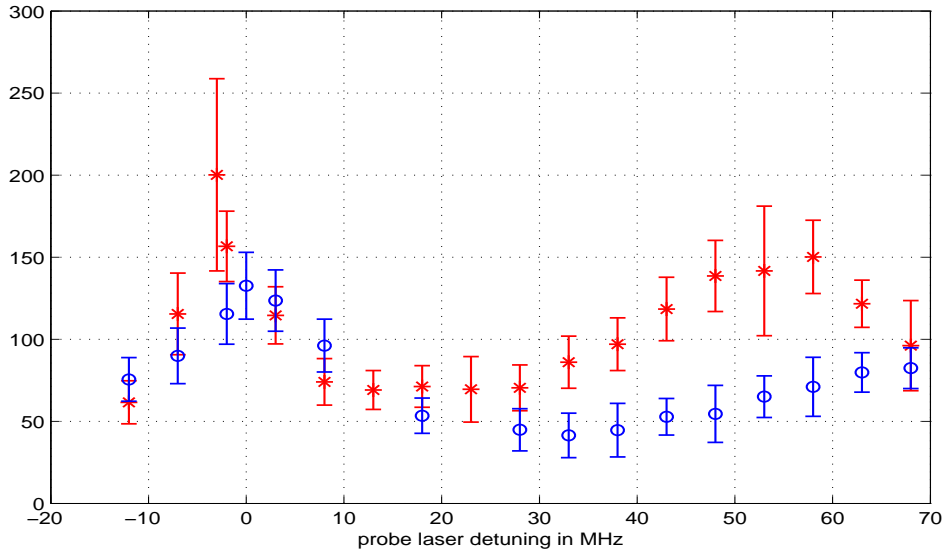
Polarization dependence



Left: Scheme of the probe and trapping beam geometry and polarization. Right: Fluorescence signal dependence on the polarization direction of the excitation laser. The 302° setting of the half-wave plate corresponds to linear polarization direction perpendicular to the detection direction. Detuning of the detection laser is +30 MHz, photomultiplier gate time 1 ms, holding time in the dipole trap 300 ms.

Figure 6.25:

With the choice of polarization for the excitation laser, and by optical pumping, different hyperfine and magnetic sub-states can be populated and probed. The level-specific coupling to the linearly polarized dipole light leads to notable differences in the trap spectra. In figure 6.26 two spectra are shown where preparation and storage conditions are identical, but the polarization of the excitation laser is different. The red data-points (stars) are obtained by detection with the $\sigma_+ - \sigma_-$ polarized MOT-beam pair and the blue data-points (circles) by detection with a linearly polarized beam driving π -transitions (see fig. 6.25 for the beam geometry and quantization axis). A magnified part of the spectrum can be seen in Fig.6.27. The fluorescence contribution from excitation with π -polarized light has been subtracted, leaving only the signal from the σ_{\pm} -excitation. From the energy distribution fit, the center frequency of the resonance is determined at +69 MHz, as well as the average thermal energy of the atoms with $k_B \cdot 360 \mu K$.



Trap population spectra obtained by detection with $\sigma_+ - \sigma_-$ polarized light (stars) and π polarized light (circles). The trapping potential $U_0 = 410$ MHz, holding time is 200 ms. Here the detuning is referenced to the free atom resonance.

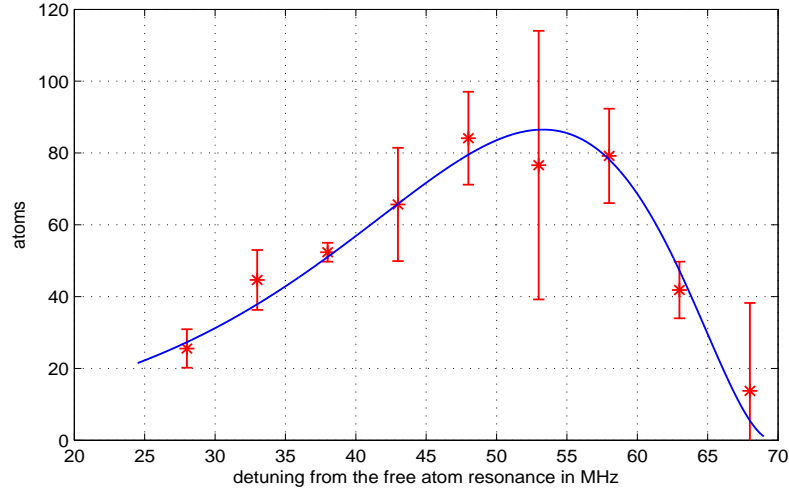
Figure 6.26:

A similar spectrum can be seen in Fig. 6.28, where excitation is done with the circularly polarized, retroreflected MOT-beam. The resonance emerging at large detunings is the light-shifted $F'=1$ excited state (see Fig. 6.20).

Evaporation Rates

From the height of the free atom peak it is possible to obtain the number of atoms which are evaporated during the detection time. Assuming that the balanced MOT-detection beam doesn't disturb considerably the energy spectrum during the short detection interval, the evaporation rate can be determined from the part of the spectrum, where the atoms are unbound. The small detection region of $18\ \mu\text{m}$ around the trap center guarantees that the atoms leave the detection region in a fraction of the photomultiplier gate time²¹. This and the calibration of the detection count signal with the sensitive photodiode^{3.5.1} provides reliable atom numbers. Figure 6.29 shows a spectrum of evaporating atoms after adiabatic lowering of the trapping potential from 230 MHz to 90 MHz and recompression of the dipole potential. From a fit of a Lorentzian lineshape function to the part of the spectrum where the atoms are free (negative detunings) the following parameters are estimated: center of the free atom peak is at -5.44 MHz, the half width is 5.7 MHz, the amplitude ~ 2140 atoms and background ~ 130 atoms. In this case the evaporation rate calculates to $\sim 4 \cdot 10^5$ atoms/s.

²¹Atoms with a mean temperature of $100\ \mu\text{K}$ have left the detection region in about 0.12 ms



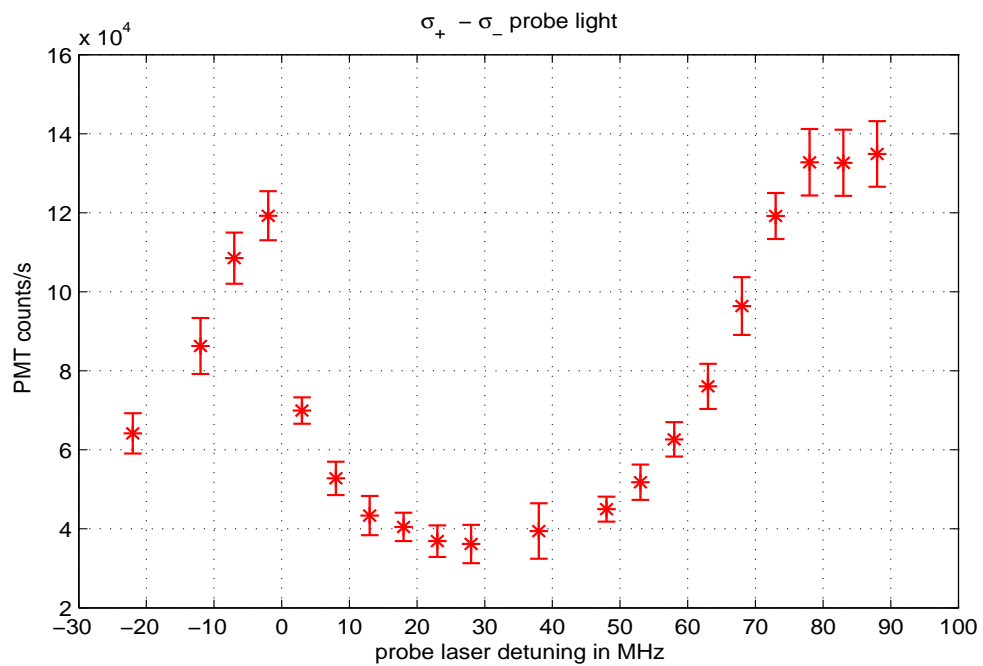
Magnified part of the trap population spectrum from Fig.6.26 where the signal contribution from the π -polarized excitation light has been subtracted so that only fluorescence from σ_{\pm} -transitions is shown. From an energy distribution fit (solid line) the center frequency of the resonance is determined at +69 MHz and the average thermal energy of the atoms is estimated with $k_B \cdot 360 \mu K$.

Figure 6.27:

Summary

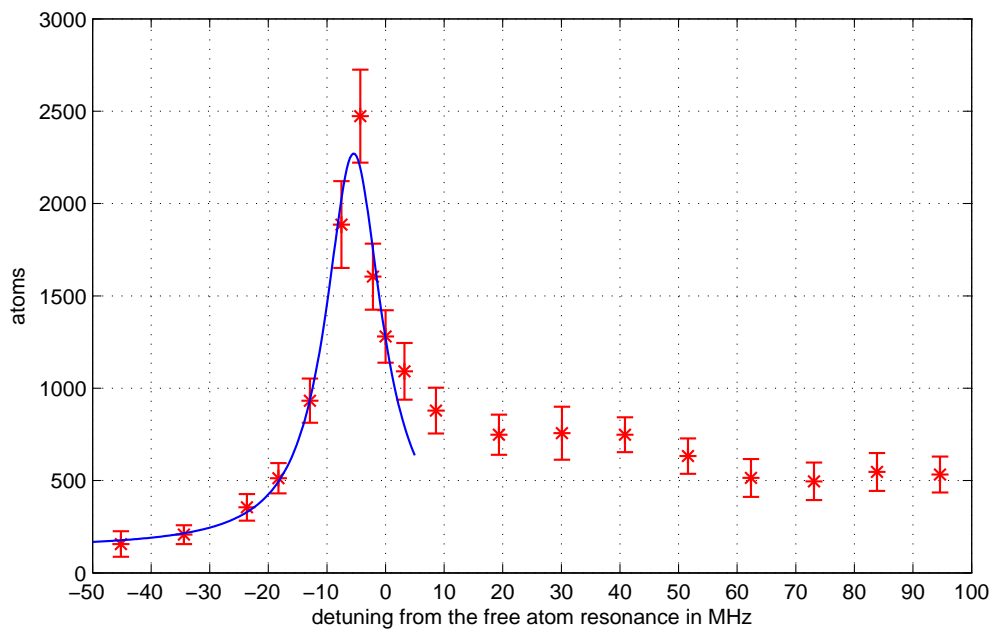
The measurements show, that trap state spectroscopy is a valuable investigative tool for characterizing trapped atoms clouds. This is especially the case for tightly confined and dense atom clouds where elastic collisions populate high energetic trap states. In this regime, the shape of the confining potential modifies strongly the sample energy distribution and predictions based on the ubiquitous harmonic potential approximation have to be checked carefully. The Gaussian potential model describes more accurately the physical situation of cold atoms inside a focused single beam trap and can be easily adapted to the crossed-beam geometry. Our model calculations based on a non-interacting, thermal Bose-gas confined in an anisotropic, 3-dimensional, Gaussian potential are consistent with the measured spectra. From this, information about the sample temperature, state occupation and light-shifts is gained. Combined with the atom number measurement, densities and cloud extensions are inferred, important parameters for the optimization of QND-type interaction as well as for other QI applications.

Interpretation of the spectra is not trivial. The multilevel structure of rubidium and the polarization dependent coupling to the dipole and excitation laser has to be considered. However, with proper state preparation techniques, where the atoms are optically pumped into a single magnetic sub-state, excitation of multiple states can be avoided. A second complication arises for deep traps, where the light-shift is comparable to the hyperfine energy. Magnetic sub-states belonging to different hyperfine states start to mix and the initially uncoupled states become superpositions of several hyperfine states.



Trap spectrum obtained with $\sigma_+ - \sigma_-$ polarized detection beam. Here the holding time (110 ms) is shorter compared to the measurement in Fig. 6.26. In this case, the higher sample temperature leads to a broader resonance and population of higher energetic states (less detuning). Detection time is 10 ms, $U_0=440$ MHz. The resonance emerging at large detunings is the light-shifted $F'=1$ excited state.

Figure 6.28:



Spectrum of the evaporating atoms after adiabatic lowering of the trapping potential from 230 MHz to 90 MHz and recompression. The solid line shows a fit of a Lorentzian lineshape function to the part of the spectrum where the atoms are free (negative detunings). The fit-parameters are: center of the free atom peak: -5.44 MHz, half width: 5.7 MHz, amplitude: ~ 2140 atoms and background: ~ 130 atoms. Holding time is 200 ms, detection time 5 ms.

Figure 6.29:

7 Outlook

This chapter serves as a brief outlook for the experimental steps necessary to implement spin squeezing on cold atomic samples, a first step towards more complex building-blocks for ensemble-based quantum information circuits like quantum memory or teleportation. [108] As the implementation of spin squeezing is currently under way with our setup, the following paragraphs should serve as an overview.

Our experimental setup incorporates a dipole trap with a waist size of $56\mu\text{m}$ producing a shallow confining potential of $260\mu\text{K}$. In this trap $5 \cdot 10^5$ atoms have been stored¹ serving as the atomic reservoir for a quantum light-matter interface based on a **Quantum Non Demolition** (QND) interaction.

Atomic ensemble experiments gained widespread attention in recent years, in great part owing to the possibility of entangling billions of particles for long time periods [107]. The lifetime of atomic multi-qubit entanglement is strongly dependent on the number of particles involved, as particle loss usually destroys the state. If however the sample of weakly interacting particles as a whole contributes to a collective quantum state, a much more robust type of entanglement can be achieved.

Spin squeezing, the conceptually simplest implementation of this QND-type light-matter interface, is outlined in the following paragraphs together with a description of the physical model and basic interaction [106].

7.1 Collective spin operators

In our description a collective atomic spin operator is defined as

$$\hat{\mathbf{F}} = \sum_{i=1}^N \hat{f}^{(i)} \quad (7.1.1)$$

where $\hat{f}^{(i)}$ denotes the total angular momentum of the i -th atom.

Commutation relations for these operators

$$[\hat{\mathbf{F}}_i, \hat{\mathbf{F}}_j] = i\hbar\epsilon_{ijk}\hat{\mathbf{F}}_k \quad (7.1.2)$$

require that the Heisenberg uncertainty relations such as

$$\langle \Delta \hat{\mathbf{F}}_x^2 \rangle \langle \Delta \hat{\mathbf{F}}_y^2 \rangle \geq \frac{1}{4} |\langle [\hat{\mathbf{F}}_x, \hat{\mathbf{F}}_y] \rangle|^2 \quad (7.1.3)$$

¹determined by recapture measurement [144]

hold.

7.2 Polarization states

Useful in the context of atom-light interaction is the representation of the polarization states in the Stokes formalism. Components of the Stokes vector are hereby expressed in terms of the creation and annihilation operators of the σ_{\pm} -field modes.

$$\begin{aligned}\hat{S}_x &= \frac{1}{2}(\hat{a}_-^\dagger \hat{a}_+ + \hat{a}_+^\dagger \hat{a}_-), \\ \hat{S}_y &= \frac{1}{2}(\hat{a}_-^\dagger \hat{a}_+ - \hat{a}_+^\dagger \hat{a}_-), \\ \hat{S}_z &= \frac{1}{2}(\hat{a}_+^\dagger \hat{a}_+ - \hat{a}_-^\dagger \hat{a}_-)\end{aligned}\tag{7.2.1}$$

Similar to eq.7.1.2 the Stokes components satisfy angular momentum commutation relations:

$$[\hat{\mathbf{S}}_i, \hat{\mathbf{S}}_j] = i\varepsilon_{ijk} \hat{\mathbf{S}}_k\tag{7.2.2}$$

Exactly this mathematical equivalence between the atomic spin and the light pseudo-spin suggested interactions where information can be exchanged between the quantum states of atoms and light.

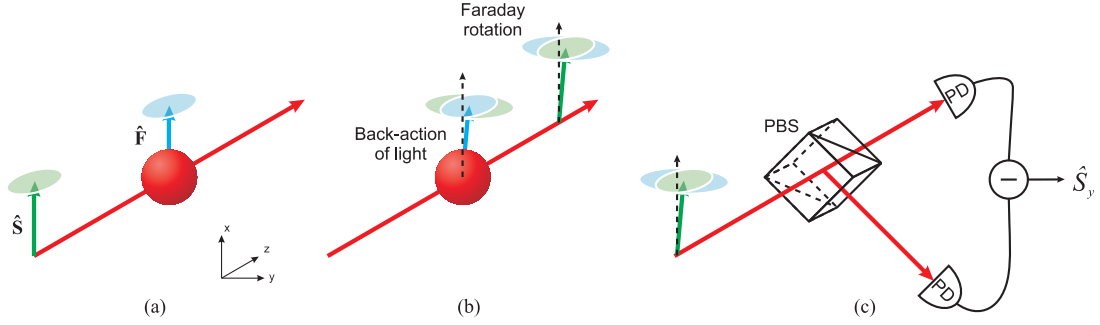
7.3 Spin squeezing

Ideally, information about the quantum state should be accessible without destroying the state. This, a prerequisite for quantum memory, requires a QND type interaction between the atoms and the light field. Off resonant, dispersive phase shifts depending on the polarization state provide exactly the desired interaction.

For the further discussion we assume both the atomic spin and polarization vector prepared in a coherent state along the x-axis (see figure 7.1). As the probe-light pulse propagates through the sample (in z direction) it interacts via the dipole coupling with the collective spin. Circular birefringence caused by the spin component in propagation direction² lead to a rotation of the light polarization around the z-axis. This is called the Faraday-effect. On the other hand the atomic spin state is rotated by the quantum fluctuations of the light. This back action essentially entangles the quantum fluctuations of the spin and polarization states. By measuring the amount of polarization rotation³ information about the fluctuations of \hat{F}_z is gained, or equivalently speaking $\Delta\hat{F}_z$ is squeezed.

²Even though $\langle F_z \rangle = 0$ the quantum fluctuations cause polarization rotation

³ $\Delta\hat{S}_y$ is measured



(a) (a): initial state preparation; (b): light-atom interaction; (c): polarimetric state detection by a polarizing beam splitter (PBS) and photodetectors (PD)

Figure 7.1:

The degree of squeezing⁴, which quantifies the non-classicality, can be expressed as [109–111]:

$$\xi^2 = \frac{1}{1 + \rho_0 \eta} \quad (7.3.1)$$

with ρ_0 the resonant optical density⁵ and η the spontaneous emission rate⁶. The definition is such that for a coherent state $\xi^2 = 1$, for squeezed states $\xi^2 < 1$. From this expression it is clear that squeezing gets stronger the higher the product of optical density and spontaneous emission is. The optical density on resonance

$$\rho_0 = \frac{N_{atom} \sigma}{A} \quad (7.3.2)$$

gives the probability for a single photon to get elastically scattered [109]. Here N_{atom} is the atom number interacting with the probe light, σ is the resonant cross section for the probed transition⁷ and A the cross section of the illuminated sample. Accordingly, the spontaneous emission rate in the far detuned case calculates to

$$\eta = \frac{N_{photon} \sigma}{A} \left(\frac{\Gamma}{\Delta} \right)^2 \ll 1. \quad (7.3.3)$$

N_{photon} is the photon number of the probe pulse, Γ the excited state decay rate and Δ the detuning. Unfortunately spontaneous emission destroys the fragile coherences and has to be kept low by detuning far off resonance. This leaves the optical density as the figure of merit for the interaction strength and thus for the amount of squeezing or entanglement⁸. Rewriting eq. 7.3.2 by using $N_{atom} = n \cdot V$ and assuming a cylindrical atomic sample with

⁴ignoring decoherence and loss

⁵In the large dipole trap we expect to reach $\rho_0 \sim 100$.

⁶For a probe pulse it is the total number of scattered photons per atom during the pulse duration. In our case $\eta \sim 0.06$

⁷For the $^{87}\text{Rb}D_2$ line and π -polarized probe light the effective $\sigma = 1.938 \cdot 10^{-9} \text{ cm}^2$ [145].

⁸Spin squeezing is a sufficient condition for an N-particle system to be entangled so the squeezing parameter indicates in some way the amount of entanglement [113].

volume $V = A \cdot l$, cross section A and length l results in

$$\rho_0 = n \cdot l \cdot \sigma \quad (7.3.4)$$

with n as the mean density of the atomic sample⁹.

Optimal for spin-squeezing applications are therefore elongated, pencil shaped, cold atomic samples with high column densities.

Taking the measured data for the tightly focused trap from paragraph 6.4.2, where the peak density of the 12 μm long atom sample reaches $n_0 = 8 \cdot 10^{14} \text{ cm}^{-3}$, the average density¹⁰ calculates to [146]

$$\langle n \rangle_{3D} = N^{-1} \int \int \int n^2(\vec{r}) d^3\vec{r} = n_0/2^{3/2} = 2.8 \cdot 10^{14} \text{ atoms/cm}^3 \quad (7.3.5)$$

leading to an optical density of $\rho_0 \sim 650$.

Compared to typical values of the optical density in a MOT ($\rho_0 \sim 25$), high density atomic samples in a FORT promise a stronger light-atomic ensemble coupling by less decoherence. This is reflected in the higher degree of squeezing attainable even if losses and decoherence are taken into account [106].

⁹We assume that the probe beam covers the entire atomic sample.

¹⁰A Gaussian density distribution is assumed

8 Appendix A

The New Focus-1801 Photodetector

The circuit analyzed here consists of a modified version of the original New Focus 1801 [58] photodetector circuit where the photo diode has been replaced by a high sensitivity Silicon-PIN photo diode (Siemens/Infineon BPX 65).

From the manufacturer data sheet:

bandwidth (BW):	dc-125 MHz	min. NEP.:	$3.3 \text{ pW}/\sqrt{\text{Hz}}$
transimpedance gain:	$4 \cdot 10^4 \text{ V/A}$	responsivity:	0.5 A/W @800 nm
saturation power :	$110 \mu\text{W}$		

Table 8.1:

The minimal detectable signal due to electronic noise is $NEP \cdot \sqrt{BW}$ ¹, in this case

$$3.3 \text{ pW}/\sqrt{\text{Hz}} \cdot \sqrt{125 \text{ MHz}} = 38 \text{ nW} (-44 \text{ dBm}) \quad (8.0.1)$$

or 0.75 mV with a gain of $2 \cdot 10^4 \text{ V/W}$. For incident optical power larger than $15 \mu\text{W}$ the detector is quantum noise limited (under optimal circumstances).

Measurements on the circuit

The Johnson-Nyquist noise power: $4 \cdot Kb \cdot T \cdot BW = 2 \text{ pW} (-87 \text{ dBm})$ is not a limiting factor. For a balanced detector made with the same amplifier circuit, the shot-noise level is $\sqrt{2}$ higher (for uncorrelated noise currents the variances sum up) with the big advantage that the incident light power can be higher leading to a better shot-noise to electronic noise ratio. The bandwidth of a balanced detector will be reduced to around 80 MHz due to the higher source capacity of a second photodiode.

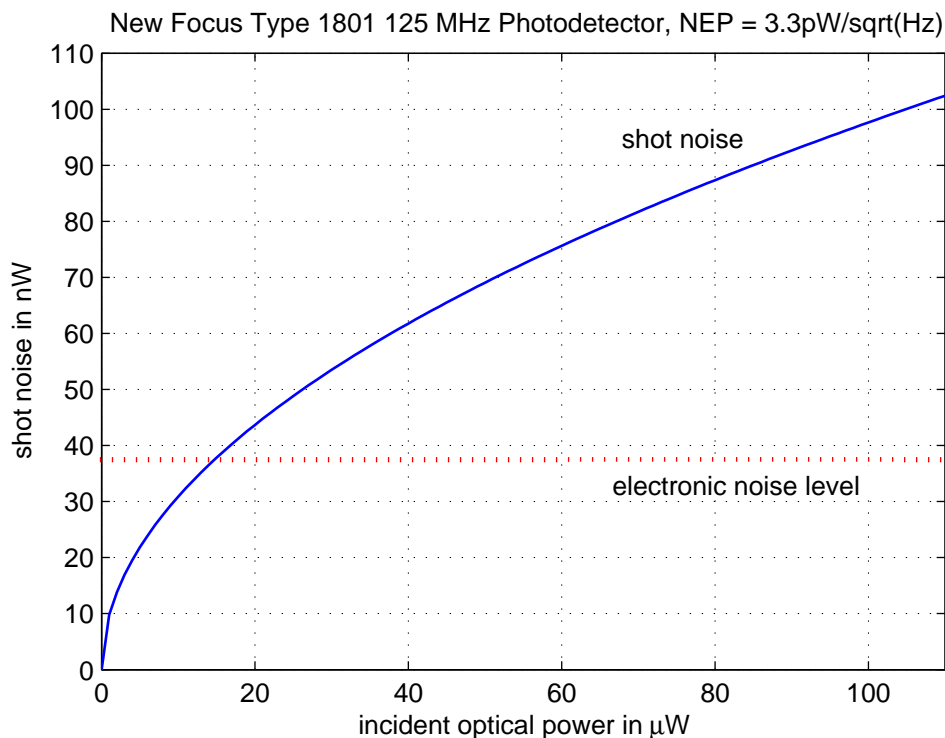
Noise level at 1 MHz according to the data sheet is -125 dBm in 10 Hz BW.

In 10 KHz:

$$-135 + 10 \cdot \log_{10}(BW) = -135 + 10 \cdot \log_{10}(10^4 \text{ Hz}) = -95 \text{ dBm}. \quad (8.0.2)$$

This agrees well with the measurement in 10.2 (red curve).

¹The Noise Equivalent Power (NEP) is defined as the minimum incident power required to generate a photo current equal to the noise current of the photo detector at a specified frequency f , and within a specific bandwidth BW.



(a) Calculated shot noise power vs. incident light power (blue curve)

Figure 8.1:

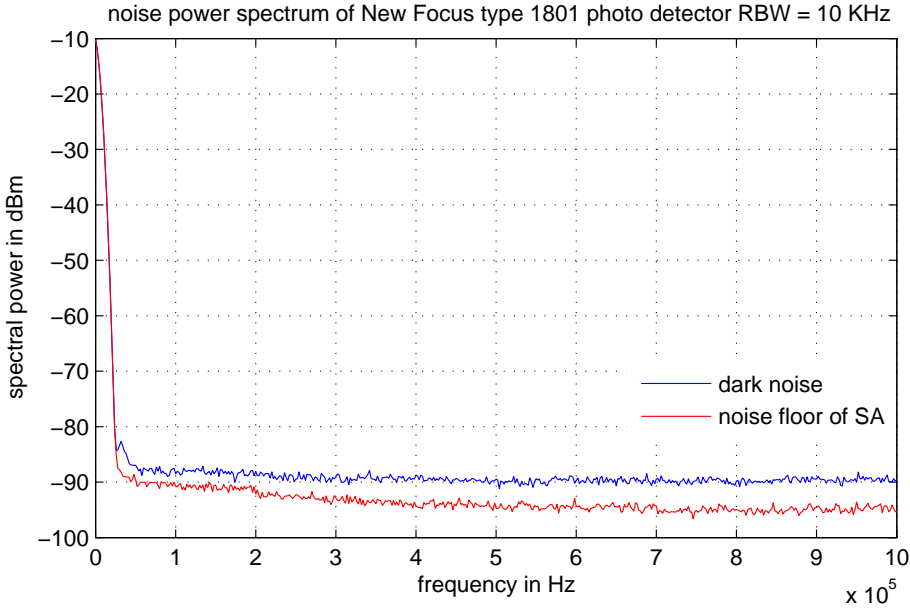
Full Bandwidth:

The average displayed noise level of 501 data points taken from a frequency range of 200 KHz to 125 MHz is -78.9 dBm. Resolution bandwidth: 10 KHz, VBW: 1 KHz, averaging, sample detector Maximum noise in 1 Hz bandwidth: 4 fW (-114 dBm) @ 39 MHz

- Effect of the log averaging: Since both video filtering and averaging over 17 trace points is performed in the log display mode, the result would be 2.51 dB too low (difference between logarithmic noise average and noise power).
- Equivalent noise bandwidth: To correct for the effect of the 4-pole Gaussian filter form instead of a rectangular filter, an equivalent noise bandwidth of 1.128* BW-3dB is used. Therefore -0.52 dB is subtracted.
- Insertion Loss: Taking into account the insertion loss of the mounted d.c.-block (< 0.8 dB in the pass band from 9 KHz to 18 GHz), 0.8 dB is added to the displayed signal.

The final corrected noise level is -78.9 dBm + 2.51 dBm - 0.52 dB + 0.8 dB

$$P_{noise} = -76.11 \text{ dBm} \quad (8.0.3)$$



(a) Detector dark noise (blue) and SA noise floor (red) measured from 50 KHz to 1 MHz.

Figure 8.2:

The average value of the noise equivalent power calculates to:

$$\langle NEP \rangle_{125MHz} = 27.4 \text{ pW} / \sqrt{Hz} \tag{8.0.4}$$

The d.c. incident optical power to reach the shot noise limit is around 1150 μW which is much higher than the saturation limit would allow.

The exceptionally good low noise behavior of the amplifier (as stated in the data sheet) is therefore strongly dependent on the bandwidth and detection frequency.

Bandwidth limited case (15 MHz Mini Circuit Low Pass Filter on PD output):

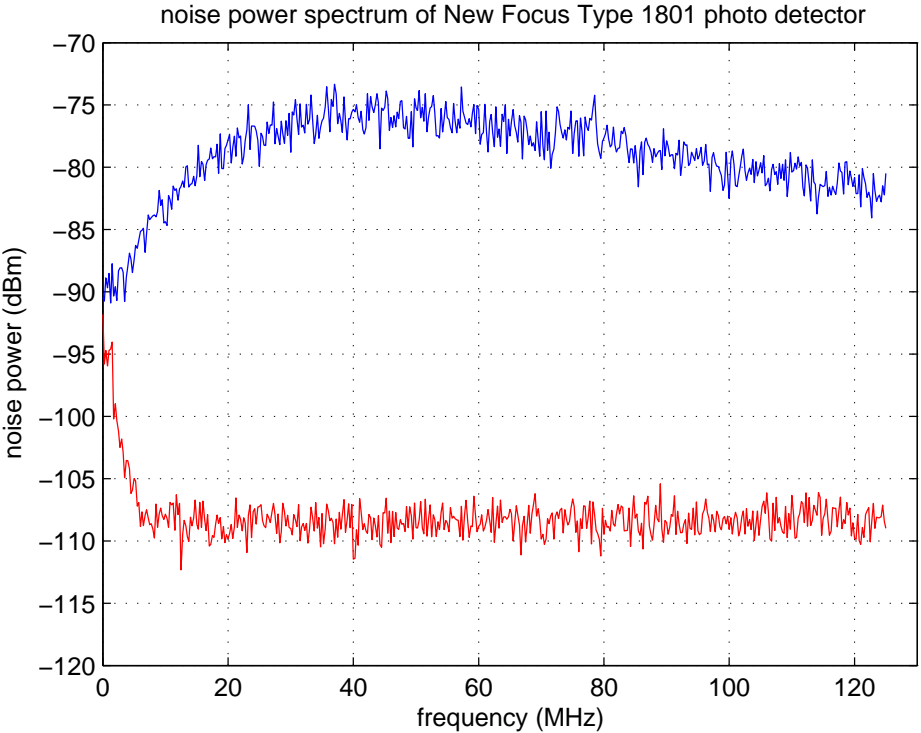
Measurement of the RMS noise voltage with the oscilloscope (Tektronix TDS300) and 15 MHz low pass filter:

$$U_{tot} = 730 \text{ } \mu\text{V} (50\Omega) \tag{8.0.5}$$

Measurement of the RMS noise voltage of the oscilloscope terminated:

$$U_{Osc} = 137 \text{ } \mu\text{V} (50\Omega)$$

$$U_{PD} = \sqrt{U_{tot}^2 - U_{osc}^2} = 717 \text{ } \mu\text{V}_{RMS} \tag{8.0.6}$$



(a) blue curve: Noise power spectrum of the photodetector (125 MHz bandwidth) and spectrum analyzer noise floor (red curve)

Figure 8.3:

Detector noise power :

$$U_{PD}^2/50\Omega = 10.3 nW_{RMS} \text{ or } -49.87 \text{ dBm} \tag{8.0.7}$$

Taking into account the transmission loss of the low pass filter in the pass band (< 1 dB), the detector noise power in 15 MHz bandwidth is:

$$P_{det} = -48.9 \text{ dBm} \tag{8.0.8}$$

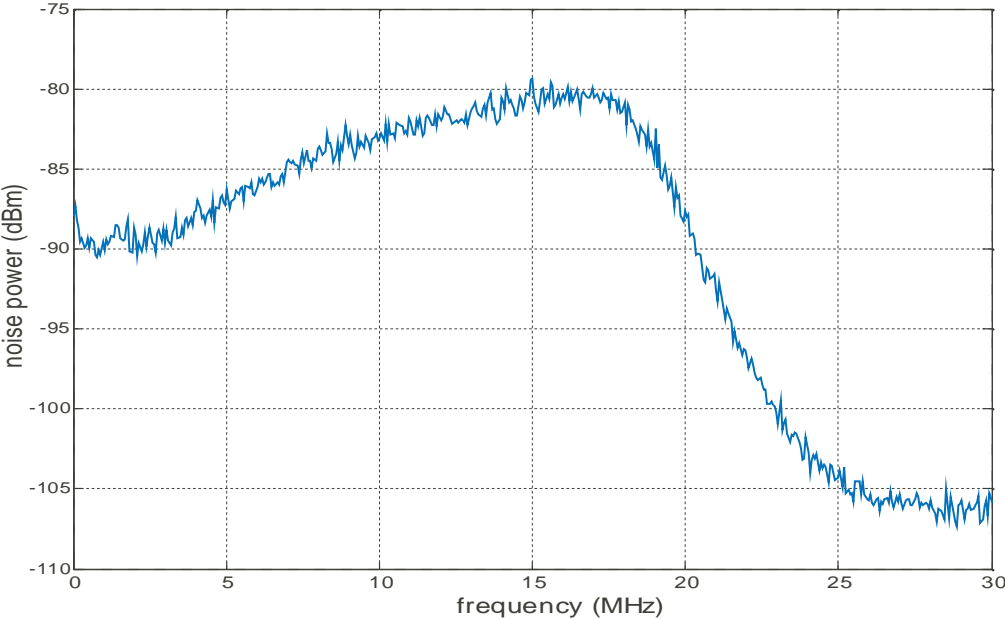
Normalized to 1 Hz bandwidth the noise power density is:

$$-48.9 - 10 \cdot \log_{10}(15 \cdot 10^6 \text{ Hz}) = -120.7 \text{ dBm/Hz} \tag{8.0.9}$$

The measurement taken with the in noise marker function of the SA around 7 MHz and corrected for the insertion loss of the D.C. block gives: -121.9 dBm/Hz . Figure 9.4 shows the trace taken with the spectrum analyzer.

Assuming a nominal bandwidth of 15 MHz (-3dB point) the mean noise equivalent power calculates to

$$\langle NEP \rangle_{15\text{MHz}} = 3.3 \text{ pW}/\sqrt{\text{Hz}} \tag{8.0.10}$$



(a) Noise power spectrum of the bandwidth limited detector. Resolution bandwidth is 10 KHz, video bandwidth 1 kHz, averaging and detector in sample mode.

Figure 8.4:

The minimum. incident optical power to reach the shot noise limit is $15\mu W$ or in units of photons/s @ 780 nm

$$15\mu W = 5.9 \cdot 10^7 \text{ photons}/\mu s \tag{8.0.11}$$

9 Appendix B

Analysis of the optical performance of the high aperture objective

This 4-lens objective is a modified version of a commercially available high aperture objective (HALO) [62]. The design was originally described in [59] and optimized for 780 nm by Mathias Schulz [60]. With the replacement of the previously used Ti:Sa trapping laser system by a solid state laser at 1030 nm¹ the objective had to be modified. The design goal was a diffraction limited spot size for 1030 nm, a high numerical aperture, a working distance > 30 mm and additionally an imaging performance at 780 nm as high as possible. Optimization is not trivial taking into account the substantial dispersion from the 250 nm difference between the trapping and imaging light. Aberrations from the vacuum cell are considered in the design and minimized by optimization of the spacing between the lenses.

The following figures show the detailed simulation carried out with the free version of the commercial optics design software Oslo from Lambda Research [61].

Performance at 1030 nm

*PARAXIAL SETUP OF LENS

APERTURE			
Entrance beam radius:	3.050000	Image axial ray slope:	-0.084599
Object num. aperture:	3.0500e-20	F-number:	5.910268
Image num. aperture:	0.084599	Working F-number:	5.910268
FIELD			
Field angle:	0.500000	Object height:	-8.7269e+17
Gaussian image height:	0.314627	Chief ray ims height:	0.314616
CONJUGATES			
Object distance:	1.0000e+20	Srf 1 to prin. pt. 1:	15.969821
Gaussian image dist.:	9.981005	Srf 11 to prin. pt. 2:	-26.071628
Overall lens length:	51.202273	Total track length:	1.0000e+20
Paraxial magnification:	-3.6053e-19	Srf 11 to image srf:	9.979668
OTHER DATA			
Entrance pupil radius:	3.050000	Srf 1 to entrance pup.:	11.169199
Exit pupil radius:	3.518511	Srf 11 to exit pupil:	-31.609674
Lagrange invariant:	-0.026617	Petzval radius:	-66.001534
Effective focal length:	36.052633		

Figure 9.1:

The wavefront distortion plot (9.4) shows clearly that for small field angles the peak to valley optical path-difference (P-V OPD) is much smaller than $\lambda/4$ (diffraction limit) resulting in

¹Yb:YAG Thin-Disk Laser from ELS Elektronik Laser System GmbH, Germany

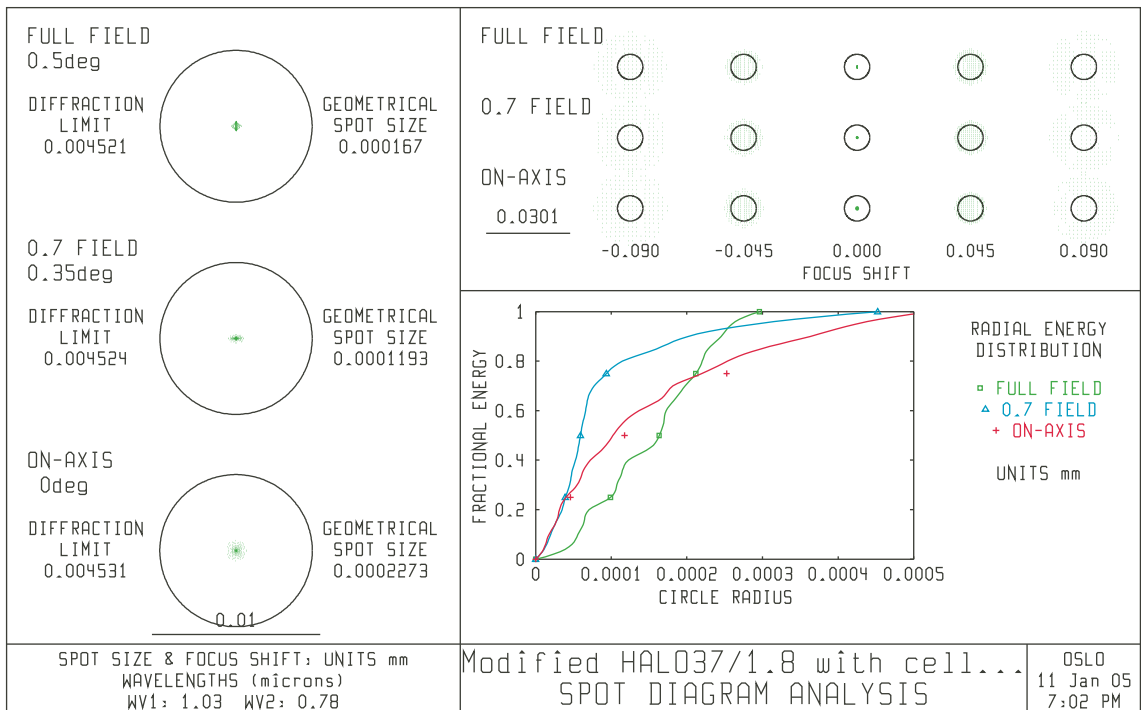
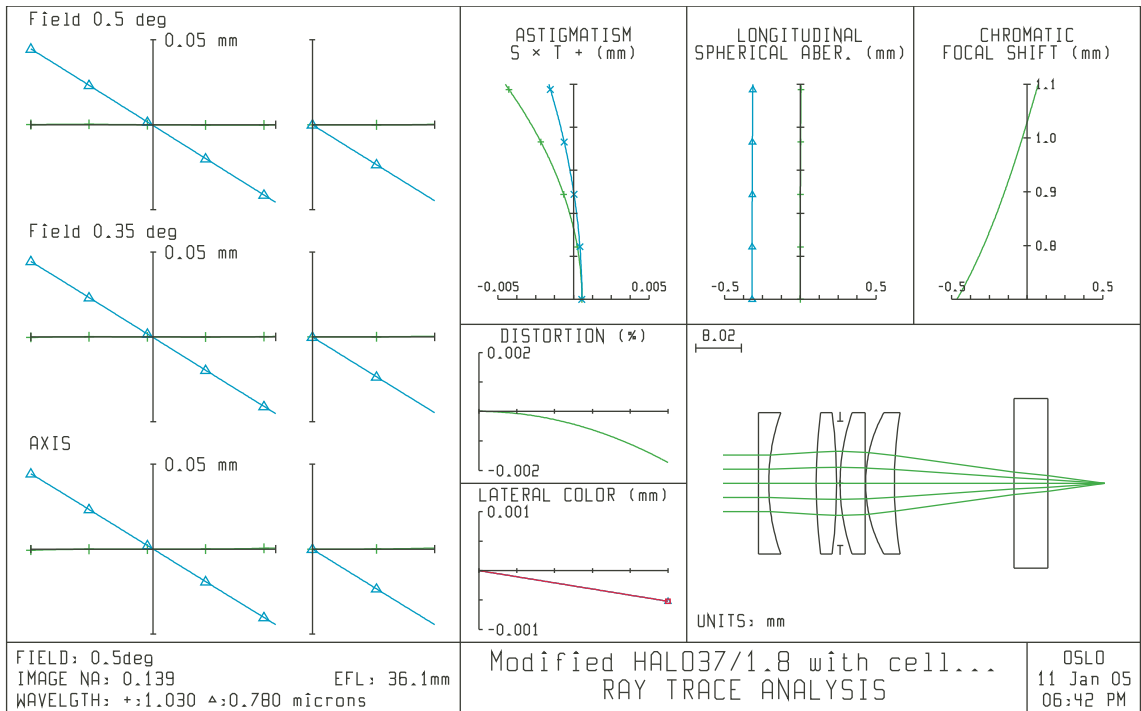


Figure 9.2:

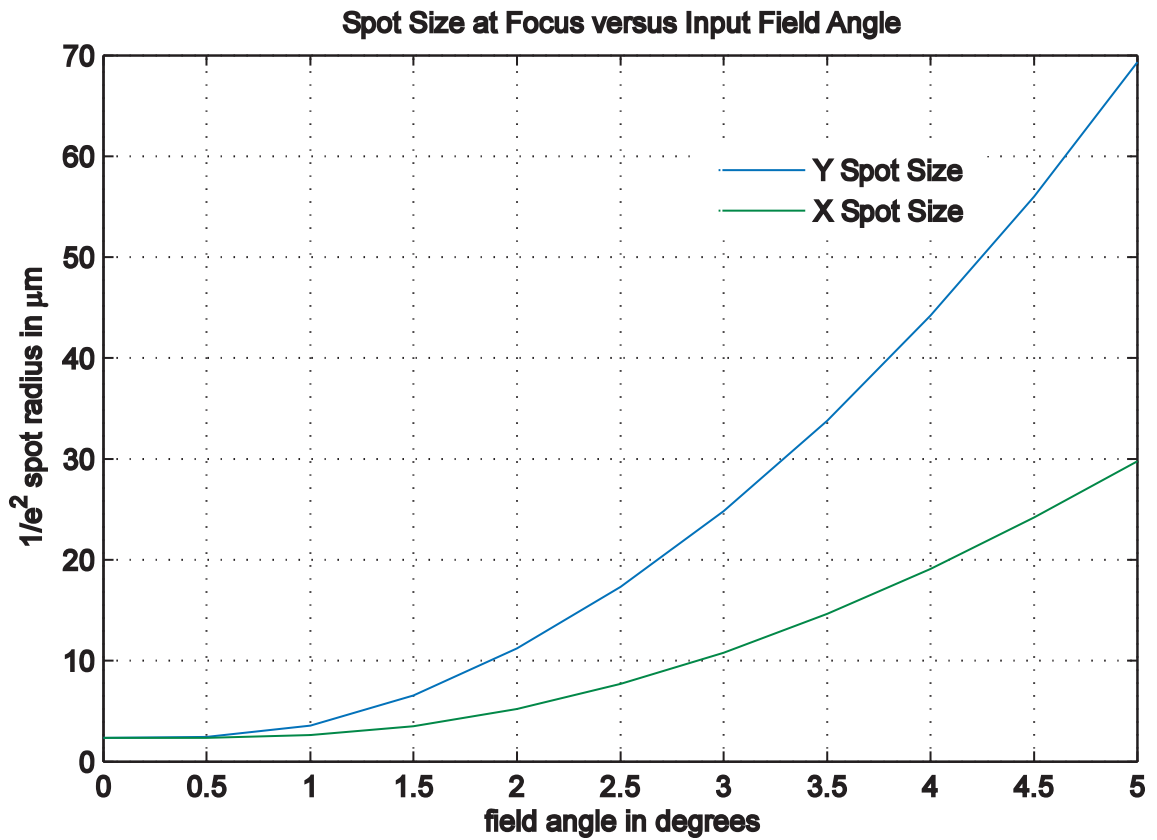
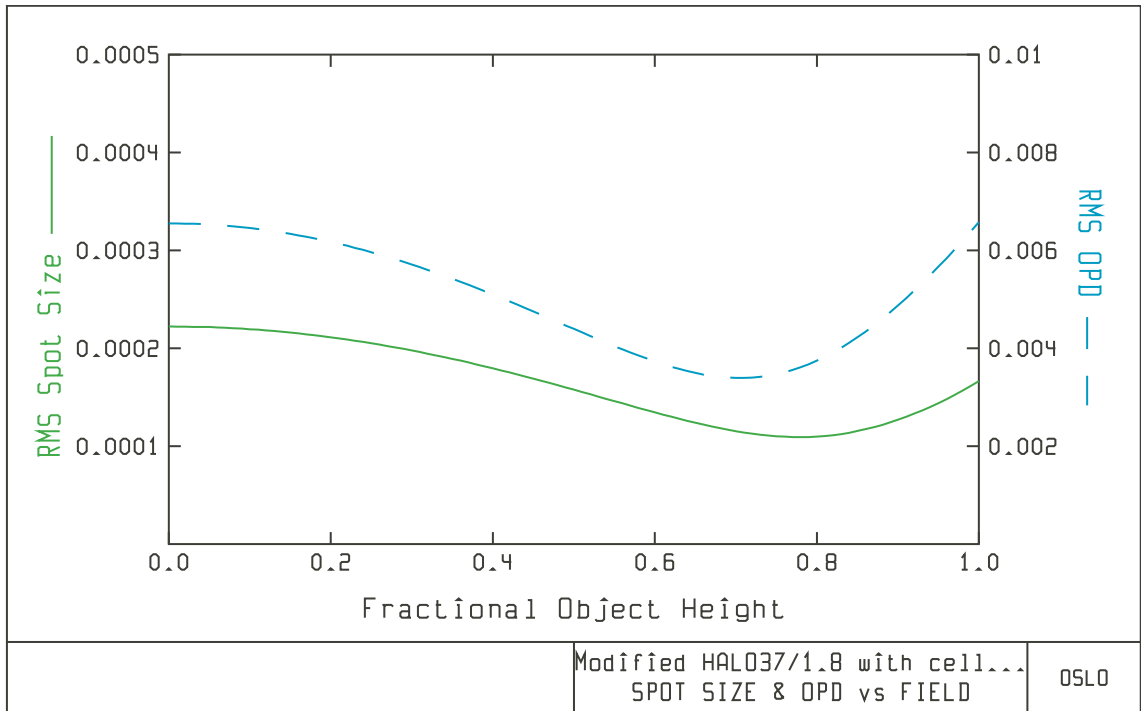


Figure 9.3:

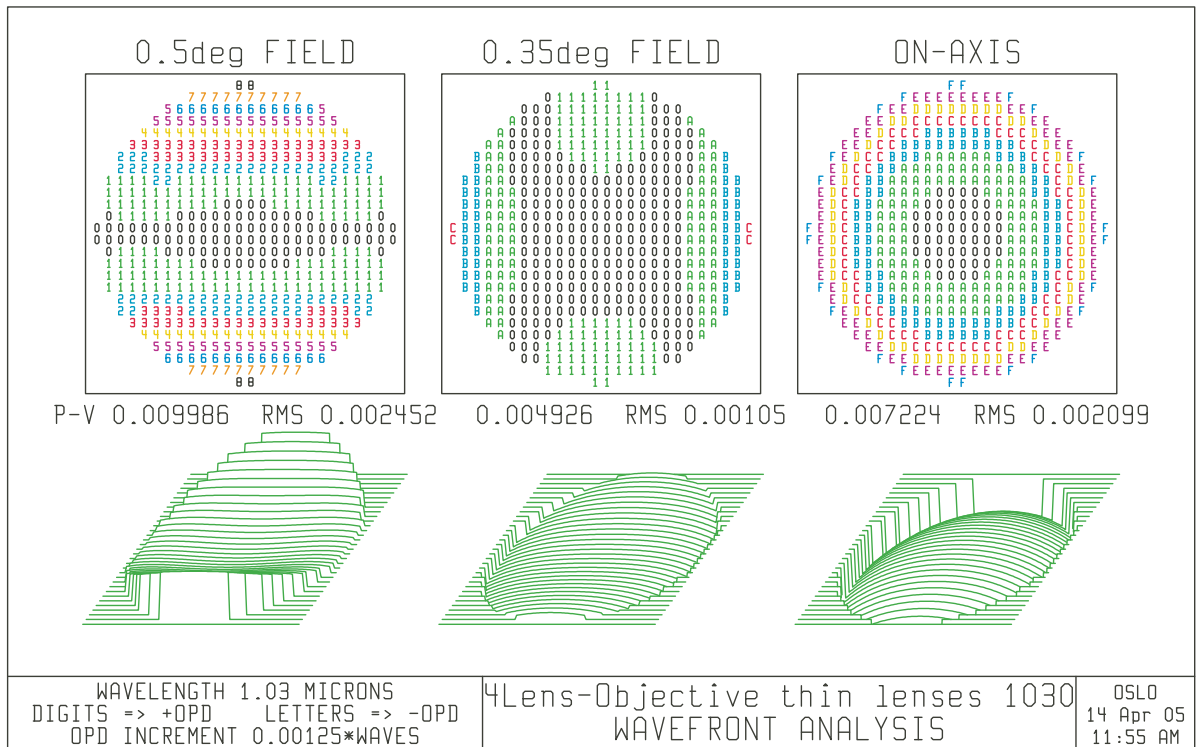


Figure 9.4:

Surface data

4Lens Objective thin lenses 1030 nm

SRF	RADIUS	THICKNESS	APERTURE RADIUS	GLASS SPE NOTE
OBJ	--	1.0000e+20	8.7269e+17	AIR
1	--	1.841110 S	12.500177	BK7 C
2	38.100000	8.400333	12.500177	AIR
3	103.291467	3.568289 S	12.500177	BK7 C
4	-103.291467	0.650067	12.500177	AIR
AST	--	9.9541e-05	11.000000 A	AIR
6	38.100000	4.408890 S	12.500177	BK7 C
7	--	0.100156	12.500177	AIR
8	26.000369	5.074152	12.500177	BK7 C
9	78.161110	21.159000 V	12.500177	AIR
10	--	6.000000	15.000000	SILICA C
11	--	10.000000	15.000000	VACUUM M
IMS	--	-0.020332	0.314741 S	

Figure 9.5:

a Strehl ratio of $S = e^{-2(2\pi\sigma)^2} = 0.9995$, where σ is the RMS wavefront aberration. It is common for high aperture objectives, that diffraction limited performance (spot size, wavefront distortions) deteriorates quickly with increasing field angles (10.2).

Bichromatic performance (1030/780 nm)

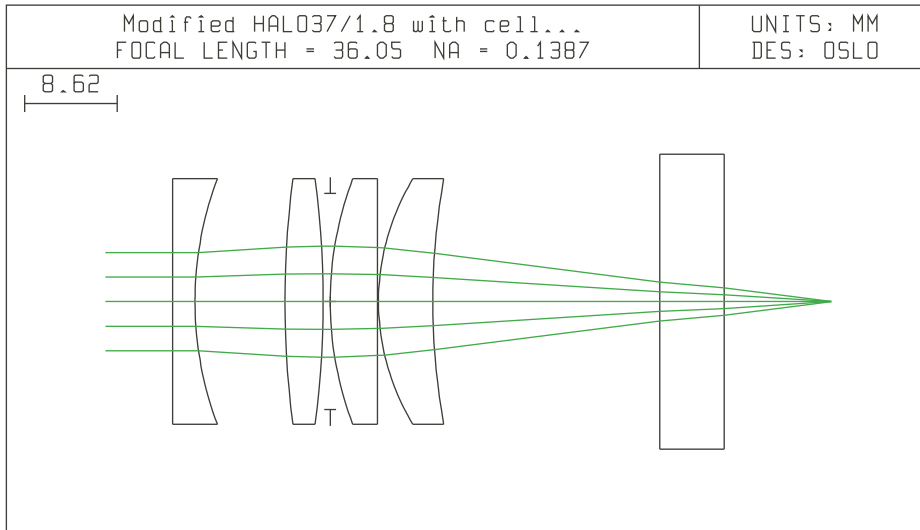
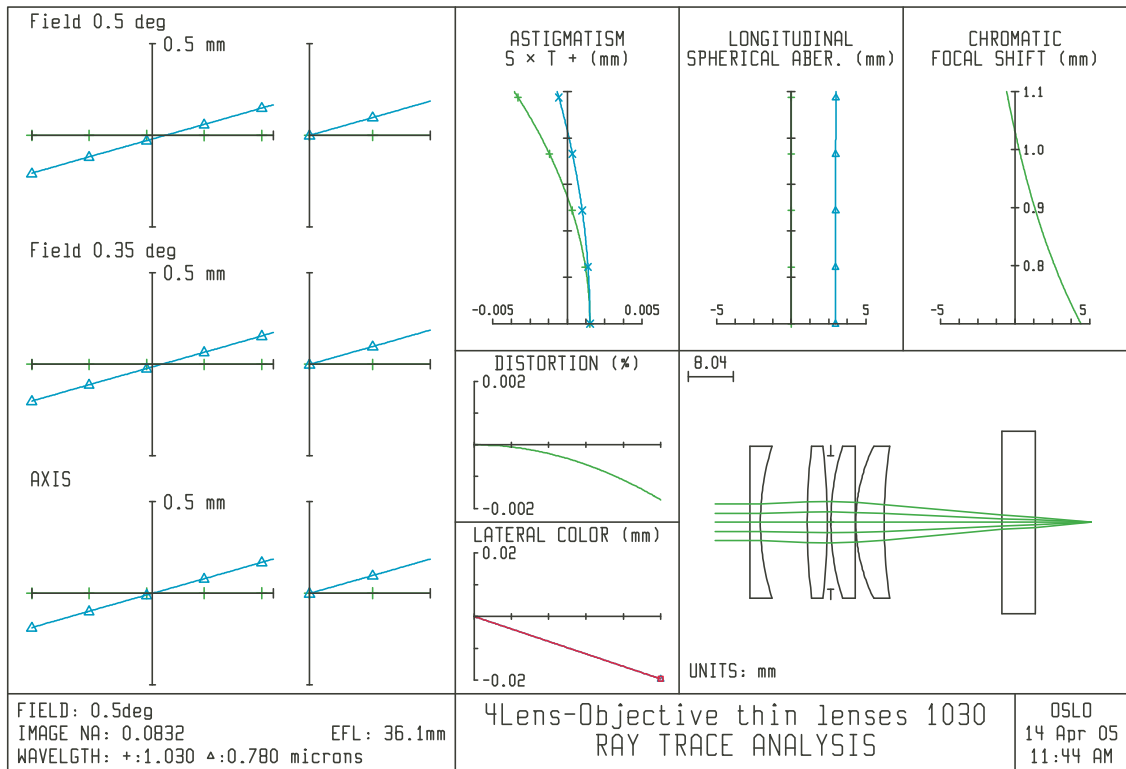
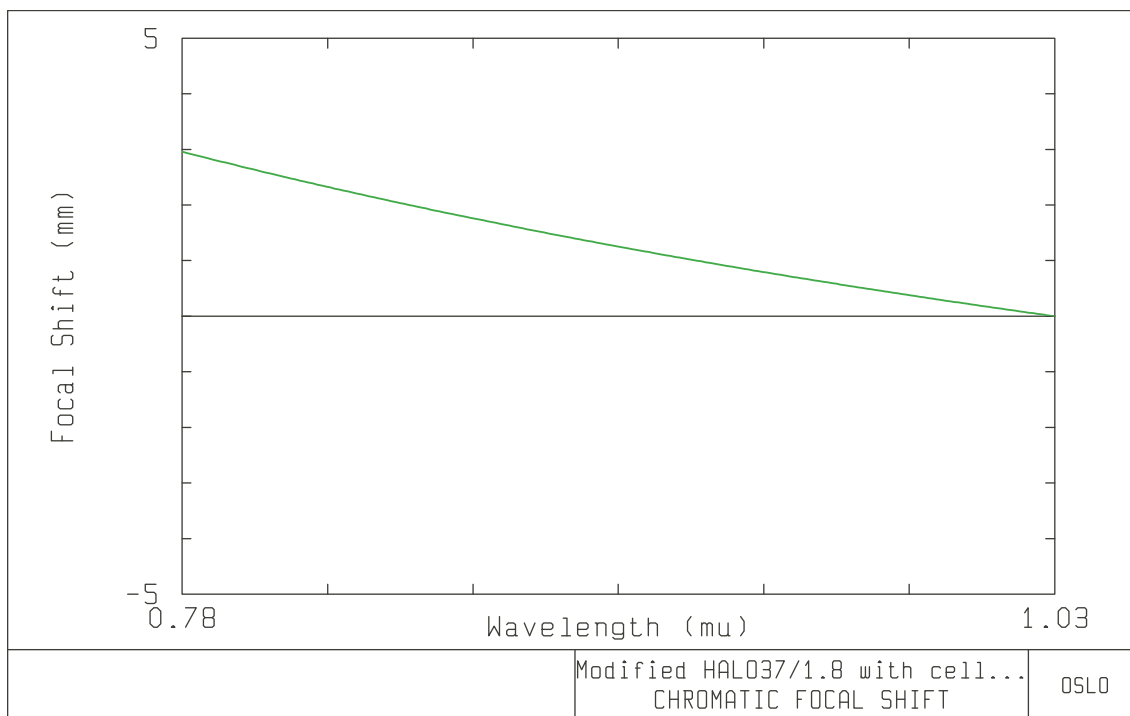


Figure 9.6:



Gaussian Beam Analysis:

*GAUSSIAN BEAM - YZ PLANE
 WAVELENGTH = 0.780000 M-SQUARED = 1.000000
 SOLUTION I

SRF	SPOT SIZE	DIVERGENCE	WAIST SIZE	WAIST DIST	INC RADIUS	RFR RADIUS	RAYLEIGH RG
INC	3.050000	8.1404e-05	3.050000	--	--	--	3.7468e+04
1	3.050000	5.3867e-05	3.050000	--	--	--	5.6620e+04
2	3.050000	0.040899	0.006067	-74.531918	-1.7413e+09	-74.532212	0.148263
3	3.393758	0.015964	0.010291	-212.571782	-82.932515	-212.573736	0.644584
4	3.450726	0.007049	0.035222	-489.507415	-216.141993	-489.558420	4.996750
5	3.455308	0.007049	0.035222	-490.157482	-490.208419	-490.208419	4.996750
6	3.455309	0.026008	0.006316	132.827125	-490.208519	132.827569	0.242788
7	3.340618	0.039291	0.006316	84.978313	128.418694	84.978616	0.160660
8	3.336681	0.069313	0.002367	48.062151	84.878461	48.062175	0.034088
9	2.984411	0.085188	0.002907	34.948485	42.988026	34.948519	0.034047
10	1.177535	0.058677	0.002907	20.045121	13.789392	20.045243	0.049494
11	0.825072	0.063675	0.002907	12.940013	14.045295	12.940173	0.045599
12	0.188777	0.063675	0.002907	2.960344	2.961047	2.961047	0.045599

*GAUSSIAN BEAM - YZ PLANE
 WAVELENGTH = 1.030000 M-SQUARED = 1.000000
 SOLUTION I

SRF	SPOT SIZE	DIVERGENCE	WAIST SIZE	WAIST DIST	INC RADIUS	RFR RADIUS	RAYLEIGH RG
INC	3.050000	0.000107	3.050000	--	--	--	2.8373e+04
1	3.050000	7.1326e-05	3.050000	--	--	--	4.2761e+04
2	3.050000	0.040572	0.008076	-75.133503	-9.9317e+08	-75.134030	0.198956
3	3.391004	0.015888	0.013691	-213.412043	-83.534310	-213.415522	0.861659
4	3.447702	0.007021	0.046696	-490.995573	-216.983754	-491.085657	6.650631
5	3.452265	0.007021	0.046696	-491.645639	-491.735604	-491.735604	6.650631
6	3.452266	0.025824	0.008422	133.654982	-491.735704	133.655778	0.326070
7	3.338387	0.038908	0.008422	85.758496	129.246915	85.759042	0.216357
8	3.334488	0.068872	0.003154	48.339041	85.658887	48.339084	0.045718
9	2.984467	0.084398	0.003875	35.277955	43.264937	35.278015	0.045810
10	1.194435	0.058276	0.003875	20.472847	14.118927	20.473062	0.066427
11	0.844385	0.084398	0.003875	9.980972	14.473152	9.981182	0.045810
12	0.003877	0.084398	0.003875	0.001304	1.610606	1.610606	0.045810

10 Appendix C

Video-Clock-Generator

For getting precisely timed images from a standard analog video camera, the framegrabber board requires advanced locking circuitry. Our framegrabber board ¹ was not able to lock on asynchronously triggered video signals, but provided inputs for user supplied external timing signals.

The genlock and synchronization circuitry described here receives the incoming video signal and generates a pixelclock (PCLK), horizontal sync (HSYNC), and vertical sync (VSYNC) signal for use by the acquisition board. The synchronization circuitry interacts with the voltage-controlled oscillator (VCO) and phase-locked loop (PLL), which generates and controls the PCLK.

According to the ITU-PAL standard a video signal has 25 frames/s, 405 vertical lines, a line rate of 10,125 lines/s and an image size of 768 x 576 pixels.

The duration of a video line is fixed at $64 \mu s$ (1 hsync period) resulting in a horizontal frequency of 15.625 KHz. Considering only pixel information, the video line duration is $52 \mu s$. This leads to a pixel-clock rate at:

$$f_{clk} = \frac{768 \text{ pixel}}{52 \mu s} = 14.7692 \text{ MHz}$$

The clock divider ratio to generate the horizontal frequency calculates then to

$$\frac{14.7692 \text{ MHz}}{15.625 \text{ KHz}} = 945$$

¹National Instruments PCI-1408
www.ni.com

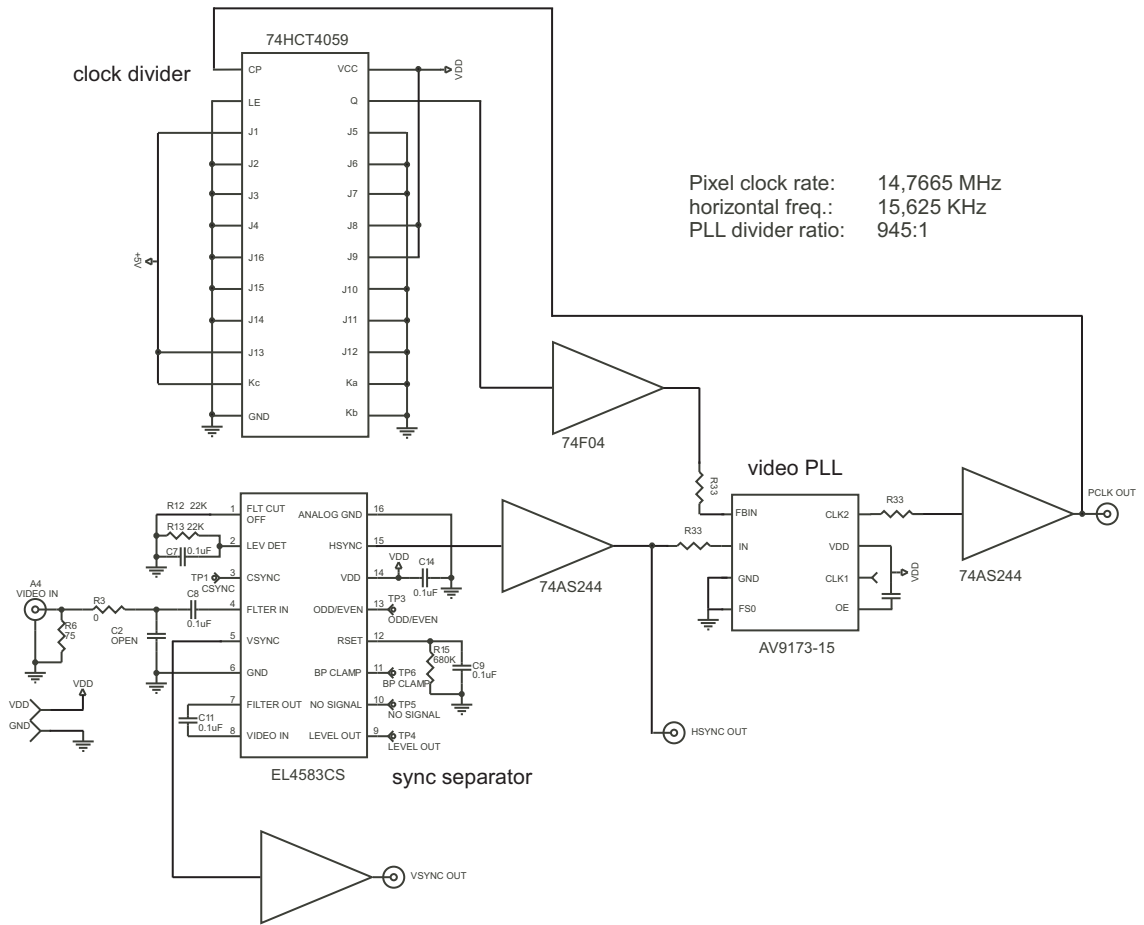


Figure 10.1:

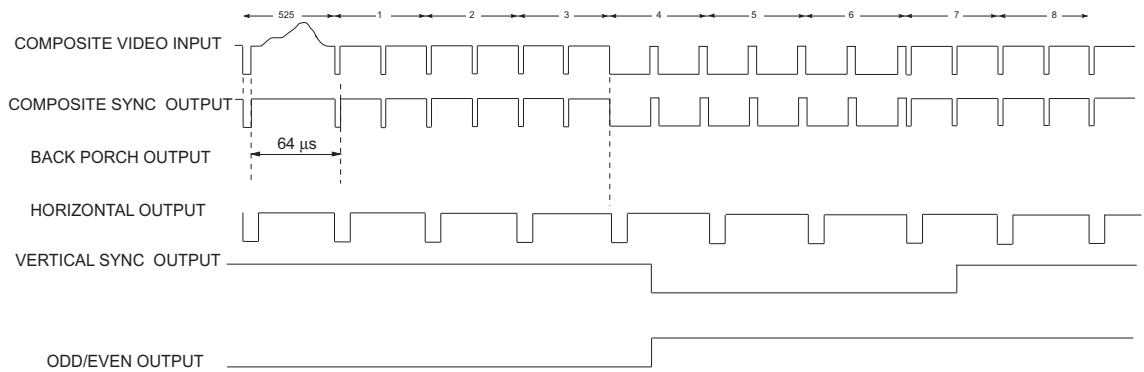
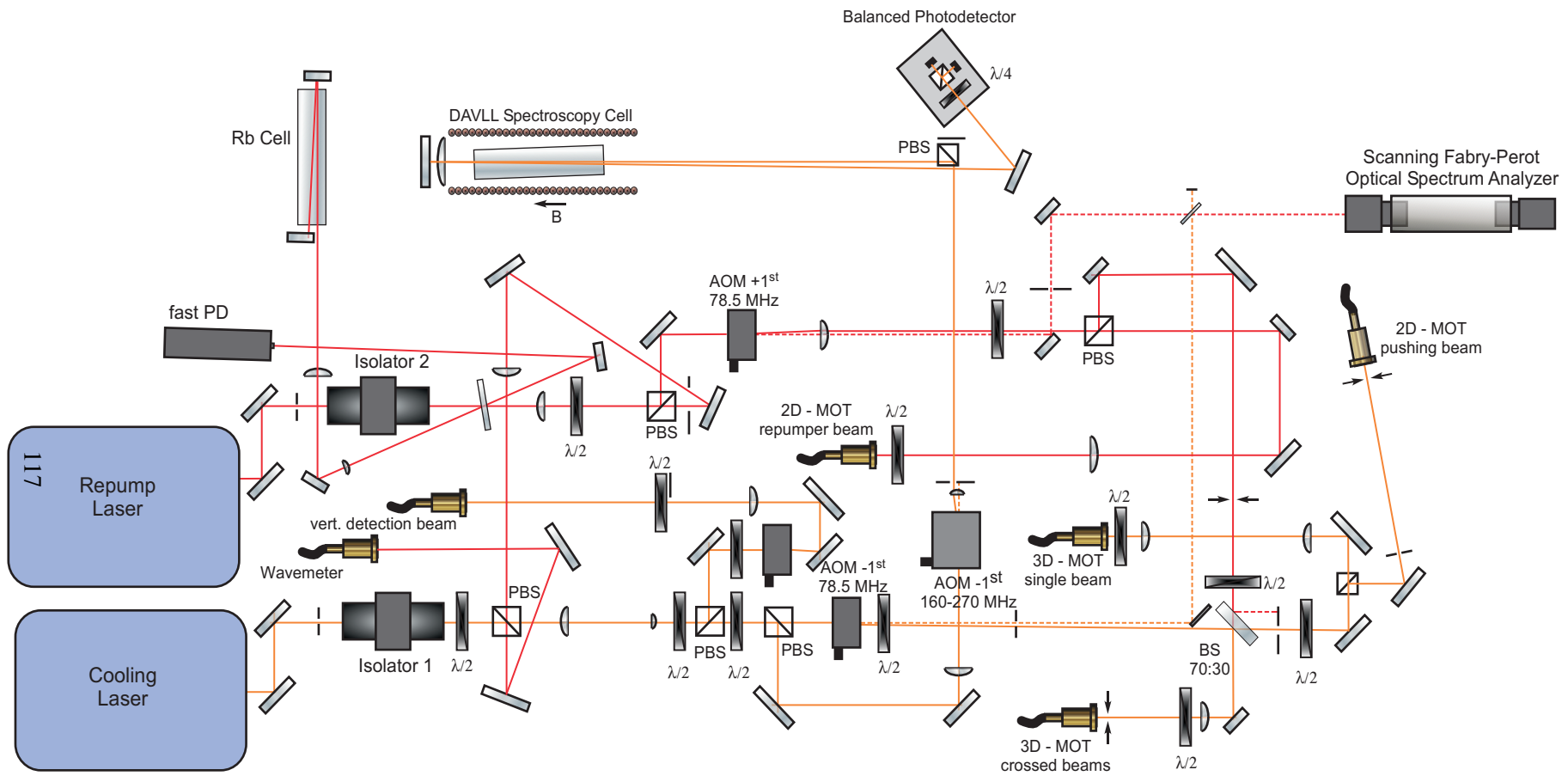


Figure 10.2:

11 Appendix D

Scheme of the MOT cooler and repump-laser optical set-up

The injection locked master-slave diode laser system delivering cooler laser light to the 2D-MOT system is not shown here.



Bibliography

- [1] Rabi, I.I., Zacharias, J.R., Millman, S., Kusch
A new method of measuring nuclear moments
Phys. Rev. **53**, 318 (1938)
- [2] Ramsey, N.F.
A new molecular beam resonance method
Phys. Rev. **76**, 996 (1949)
- [3] Kastler, A.
Quelques suggestions concernant la production optique et la détection optique d'une inégalité de population des niveaux de quantification spatiale des atoms
J. Phys. **11** 255-265 (1950)
- [4] Hänsch, T.W., Shawlow, A.L.
Opt. Comm. **13**, 68 (1975)
- [5] Neuhauser, W., Hohenstatt, M., Toschek, P., Dehmelt, H.
Optical-sideband cooling of visible atom cloud confined in parabolic well
Phys. Rev. Lett. **41**, 233-236 (1978)
- [6] Wineland, D.J., Drullinger, R.E., Walls, F.E.
Radiation pressure cooling of bound resonant absorbers
Phys. Rev. Lett. **40**, 1639-1642 (1978)
- [8] Dalibard, J., Cohen-Tannoudji, C.,
Laser cooling below the Doppler-limit by polarization gradients
J. Opt. Soc. Am. **B6**, 2023 (1989)
- [10] Ashkin, A.
Trapping of atoms by resonance radiation pressure
Phys. Rev. Lett. **40**, 729 (1978)
- [7] Lett, P.D., Watts, R.N., Westbrook, C. I., Phillips, W. D., Gould, P.D., Metcalf, H.J.,
Observation of atoms laser cooled below the Doppler limit
Phys. Rev. Lett. **61**, 169 (1988)
- [9] Anderson, M.H., Ensher, J.R., Matthews, M.R., Wieman, C.E., Cornell, E.A.
Observation of Bose-Einstein condensation in dilute atomic vapor
Science **269**, 198-2001 (1995)
- [14] Weiner, J. Bagnato, V. S., Zilio, S., Julienne, P.S.
Experiments and Theory in cold and ultracold collisions
Rev. Mod. Physics **71**, No. 1, (1999)
- [11] Raab, E.L., Prentiss, M., Cable, A., Chu, S. and Prichard, D.E.
Trapping of neutral sodium atoms with radiation pressure
Phys. Rev. Lett. **59**, 2631 (1987)

- [12] Chu, S., Bjorkholm, J.E., Ashkin, A.S., Cable, A.
Experimental observation of optically trapped atoms
Phys. Rev. Lett. **57**, 314 (1986)
- [13] Cirac, J.I., Parkins, A.S., Blatt, R.
Nonclassical states of motion in ion traps
Adv. Atom, Mol., Opt. Phys. **37**, 237-296 (1996)
- [15] Tiesinga, E., Verhaar, B.J., Stoof, H.T.C.
Threshold and resonance phenomena in ultracold ground state collisions
Phys. Rev. A **47**, 4114-4122 (1993)
- [16] Fisher, M.P.A., Weichman, P.B., Grinstein, G., Fisher, D.S.
Boson localization and the superfluid-insulator transition
Phys. Rev. B **40**, 546-570 (1989)
- [17] Greiner, M., Mandel, O., Esslinger, T., Hänsch, T.W., Bloch, I.
Quantum phase transition from a superfluid to a Mott insulator in a gas of ultracold atoms
Nature **415**, 39-44 (2002)
- [18] Zwierlein, M.W., Abo-Shaer, J.R., Schirotzke, A., Schunck, C.H., Ketterle, W.
Vortices and superfluidity in a strongly interacting Fermi-gas
Nature **453**, 1047-1051, (2005)
- [19] Tinkham, M.
Introduction to Superconductivity
2nd edn, Dover, Mineola, NY, 2004
- [20] Jaksch, D., Zoller, P.
The cold atom Hubbard toolbox
Ann. Phys. **315**, 52-79 (2005)
- [21] Chevy, F., Salomon. Ch.
Superfluidity in Fermi gases
Physics World **18(3)**, 43-47 (2005)
- [22] Diedrich, F., Bergquist, J.C., Itano, W.M., Wineland, D.J.
Laser cooling to the zero-point energy of motion
Phys. Rev. Lett. **62**, 403-406 (1989)
- [23] Cirac, J.I., Zoller, P.
Quantum computation with cold trapped ions
Phys. Rev. Lett. **74** 4091-4094 (1995)
- [24] Stean, A.
The ion trap quantum information processor
Appl. Phys. B, **64** 623-642 (1997)
- [25] Blatt, R., Stean, A.
Quantum information processing with trapped ions
eds. Van derPyl, T., Karlson, A., Belina-Podgaetsky, M.
Communication in Europe, 161-169, European Communities, 2005
- [26] Young, B.C., et al.
Laser Spectroscopy XIV

- eds. Blatt, R., Eschner, J., Leibfried, D., Schmidt Kahler, F.,
World Scientific, Singapore, 1999
- [27] Hall, J., Notcutt, M., Ye, J.
Improving Laser Coherence
eds. Hinds, E.A., Ferguson, A., Riis, E.
Proceedings of the Int. Conference in Laser Spectroscopy, 2005
- [28] Diddams, S.A., et al.
An optical clock based on a single trapped ^{199}Hg ion
Science **293**, 825-828 (2001)
- [29] Reichert, J., Holzwarth, R., Udem, Th. Hänsch, T.W.
Measuring the frequency of light with mode-locked lasers
Opt. Commun. **172**, 59-68 (1999)
- [30] <http://www.menlosystems.com>
- [31] Apolonski, A., et al.
Controlling the phase evolution of few cycle light pulses
Phys. Rev. Lett. **85**, 740-743 (2000)
- [32] Marian, A., Stowe, C. M., Lawall, J.R., Felinto, D., Ye, J.
United Time-Frequency Spectroscopy for Dynamics and Global Structure
Science **306**, 2063 (2004)
- [33] Stowe, M., Cruz, F., Marian, A., Ye, J.
High Resolution Atomic Coherent Control via Spectral Phase Manipulation of an Optical Frequency Comb
Phys. Rev. Lett. **96**, 153001 (2006)
- [34] Neuhauser, N., Hohenstatt, M., Toschek, P.E., Dehmelt, H.
Localized visible Ba^+ mono-ion oscillator
Phys. Rev. A **22**, 1137-1140 (1980)
- [35] Wineland, D., Dehmelt, H.
Proposed $10^{14}\Delta\nu < \nu$ laser fluorescence spectroscopy on Tl^+ mono-ion oscillator
Bull. Am. Phys. Soc. **20**, 637 (1975)
- [36] Rafac, R. J., Young, B.C., Beall, J.A., Itano, W. M., Wineland, D.J., Bergquist, J.C.
Sub-dekahertz ultraviolet spectroscopy of $^{199}\text{Hg}^+$
Phys. Rev. Lett. **85**, 2462-2465 (2000)
- [37] Walther, H.
Adv. At. Mol. Opt. Phys. **31**, 137 (1993)
- [38] Monroe, C., Meekhof, D. M., King, B. E., Itano, W. M. & Wineland, D. J.
Demonstration of a universal quantum logic gate
Phys. Rev. Lett. **75**, 4714-4717 (1995)
- [39] S. Gulde, M. Riebe, G.P.T. Lancaster, C. Becher, J. Eschner, H. Häffner, F. Schmidt-Kaler, I.L. Chuang, and R. Blatt
Implementing the Deutsch-Jozsa algorithm on an ion-trap quantum computer
Nature **421**, 48 (2003)
- [40] F. Schmidt-Kaler, H. Häffner, M. Riebe, S. Gulde, G. P. T. Lancaster, T. Deuschle, C. Becher, C. F. Roos, J. Eschner, and R. Blatt

- Realization of the Cirac-Zoller controlled-NOT quantum gate*
Nature **422**, 408 (2003)
- [41] Blatt, R., Zoller, P.
Quantum jumps in atomic systems
Eur. J. Phys. **9**, 250 (1988)
- [42] Jaksch D., Briegel H.J., Cirac, J.I., Gardiner, C.W., Zoller, P.
Entanglement of atoms via cold controlled collisions
Phys. Rev. Lett. **82**, 1975-1978 (1999)
- [43] Dalibard, J., Cohen-Tannoudji, C.
Dressed atom approach to atomic motion in laser light: the dipole force revisited
J. Opt. Soc. Am. B **2**, 1707-1720 (1985)
- [44] J. R. Fuhr, H. R. Felrice, K. Olsen, and J. Hwang
Bibliographic database on atomic transition probabilities
National Institute of Standards and Technology, Atomic Physics Division
<http://physics.nist.gov/PhysRefData/ASD/index.html>
- [45] Cohen-Tannoudji, C., Dupont-Roc, J., Grynberg, G.
Atom-Photon Interactions: Basic Processes and Applications
John Wiley & Sons, Inc (1992)
- [46] Glauber, R.J.
Coherent and Incoherent States of the Radiation Field
Phys. Rev. **131**, 2766 (1963)
- [47] Arfken, G.
Spherical Harmonics and Integrals of the Products of Three Spherical Harmonics
Mathematical Methods for Physicists, 3rd ed. Orlando, FL:Academic Press (1985)
- [48] Sobelman, I.J.
Atomic Spectra and Radiative Transitions
Springer, Berlin (1992)
- [49] Mathematica from Wolfram Research
<http://www.wolfram.com/products/mathematica/index.html>
- [50] Metcalf, J.H., van der Straten, P.
Laser Cooling and Trapping
Graduate Texts in Contemporary Physics, Springer, Heidelberg (1999)
- [51] Brink, D.M., Satchler, G.R.
Angular Momentum
Oxford (1962)
- [52] Loudon, R.
The Quantum Theory of Light
2nd ed. Oxford University Press (1983)
- [53] Corwin, K.L.
A Circularly-Polarized Optical Dipole Trap and other Developments in Laser trapping of Atoms
Ph.D. thesis, Univ. of Colorado (1999)

- [54] Davidson, N., Lee, H.J., Adams, C.S., Kasevich, M., and Chu, S.
Long Atomic Coherence Times in an Optical Dipole Trap
Phys. Rev. Lett. **74**, 1311 (1995)
- [55] Kuga, T., Torii, Y., Shiokawa, N., Hirano, T., Shimizu, Y., and Sasada, H.
Novel Optical Trap of Atoms with a Doughnut Beam
Phys. Rev. Lett. **78**, 4713 (1997)
- [56] Müller-Seydlitz, T., Hartl, M., Brezger, B., Hänsel, H., Keller, C., Schnetz, A., Spreew, R. J. C., Pfau, T., and Mlynek, J.
Atoms in the Lowest Motional Band of a Three-Dimensional Optical Lattice
Phys. Rev. Lett. **78**, 1038 (1997)
- [57] Ozeri, R., Khaykovich, L., and Davidson, N.
Long spin relaxation times in a single-beam blue-detuned optical trap
Phys. Rev. A **59**, R1750 (1999)
- [58] New Focus, San Jose, USA www.newfocus.com/
- [59] Alt, W.
An objective lens for efficient fluorescence detection of single atoms
Optik 113, No. **3** 142-144 (2002)
- [60] Schulz, M.
Tightly confined atoms in optical dipole traps
Ph.D. thesis, University of Innsbruck (2002)
- [61] Lambda Research Corporation www.lambdaresearch.com
- [62] Linos Photonics GmbH + Co. KG www.linos.com
- [63] International Telecommunication Union www.itu.int/
- [64] Binnewies, T., et al.
Doppler Cooling and Trapping on Forbidden Transitions
Phys. Rev. Lett. **87**, 123002 (2001)
- [65] Katori, H., Tetsuya, I., Yoshitomo, I., and Makoto, K.G.
Magneto-Optical Trapping and Cooling of Strontium Atoms down to the Photon Recoil Temperature
Phys. Rev. Lett. **82**, 1116-1119 (1999)
- [66] Castin, Y. and Dalibard, J.
Europhys. Lett. **14**, 761 (1991)
- [67] Dieckmann, K., Spreew, R. J. C., Weidemüller, M., Walraven, J. T. M.
Two-dimensional magneto-optical trap as a source of slow atoms
Phys. Rev. A **58**, 3891 (1998)
- [68] Cairns, A.R.L., Telles, G.D., Mancini, M.W., Marcassa, L.G., Bagnato, V.S., Wilkowski, D., Kaiser, R.
Intensity Dependence for Trap Loss Rate in a Magneto-Optical Trap of Strontium
Brazilian Journal of Physics, **34**, no. 4A, (2004)
- [69] Riis, E., Weiss, D.S., Moler, K.A., Chu, S.
Atom funnel for the production of a slow, high-density atomic beam
Phys. Rev. Lett. **64**, 1658 (1990)

- [70] K. Dieckmann, K., Spreew, R. J. C., Weidemüller, M., Walraven, J.T.M.
Two-dimensional magneto-optical trap as a source of slow atoms
Phys. Rev. A **58**, 3891-3895 (1998)
- [71] Monroe, C., Swann, W., Robinson, H., Wieman, C.
Very Cold Trapped Atoms in a Vapour Cell
Phys. Rev. Lett. **65**, 1571(1990)
- [72] Bali, S., O' Hara, K.M.O., Gehm, M.E., Granade, S.R., Thomas, J.E.
Quantum-diffractive background gas collisions in atom-trap heating and loss
Phys. Rev. A **60**, R29-R32 (1999)
- [73] Schoser, J., Batär, A., Löw, R., Schweikhard, V., Grabowski, A., Ovchinnikov, Yu. B., Pfau, T.
An Intense Source of Cold Rb Atoms from a Pure 2D-MOT
arXiv:physics/0201034 v1 (2002)
- [74] Roos, C.F., Cren, P., Dalibard, J., Guery-Odelin, D.
A source of cold atoms for a continuously loaded magnetic guide
arXiv:cond-mat/0212060 v1 3 Dec 2002
- [75] Lett, P.D., et al.,
Optical Molasses,
J. Opt. Soc. Am. B **6**, 2084 (1989)
- [76] Arnold, A.S., Manson, P.J.
Atomic density and temperature distributions in magneto-optical traps
J. Opt. Soc. Am. B **17**, 497 (2000)
- [77] Sesko, D.W., Walker, T.G., Wieman, C.E.
Behavior of neutral atoms in a spontaneous force trap
J. Opt. Soc. Am. B **8**, No. 5 946 (1991)
- [78] Townsend, C.G., Edwards, N.H., Cooper, C.J., Zetie, K.P., Foot, C.J.
Phase-space density in the magneto-optical trap
Phys. Rev. A **52**, 1423 (1995)
- [79] Hillenbrand, G., Foot, C.J., Burnett, K.
Heating due to long-range photon exchange interactions between cold atoms
Phys. Rev. A **50**, 1479-1489 (1994)
- [80] Hoffmann, D., Feng, P., Walker, T.
Measurements of Rb trap-loss collision spectra
J. Opt. Soc. Am. B **11**, 712 (1994)
- [81] Grego, S., Colla, M., Fioretti, A., Müller, J.H., Verkerk, P., Arimondo, E.
A cesium magneto-optical trap for cold collision studies
Opt. Comm. **132**, 519-526 (1996)
- [82] Gehm, M.E., O'Hara, K.M., Savard, T.A., Thomas, J.E.
Dynamics of noise-induced heating in atom traps
Phys. Rev. A **58**, 3914-3921 (1998)
- [83] Miller, C.M.
Intensity Modulation and Noise Characterization of High-Speed Semiconductor

- Lasers*
IEEE LTS, pp. 44-52, (1991)
- [84] Barrett, M.D., Sauer, J.A., Chapman, M.S.,
All-Optical Formation of an Atomic Bose-Einstein Condensate
Phys. Rev. Lett. **87**, 010404 (2001)
- [85] Dumke, R., Johanning, M., Gomez, E., Weinstein, J.D., Lett, P.D., Jones, K.M.,
All-optical generation and photoassociative probing of sodium Bose-Einstein condensates
New Journal of Physics **8** (2006) 64
- [86] Kobayashi, J., Izumi, Y., Kumakura, M., Takahashi, Y.
Stable all-optical formation of Bose-Einstein condensate using pointing-stabilized optical trapping beams
Appl.Phys. B **83**, 21-25 (2006)
- [87] Stenger, J., Inouye, S., Stamper-Kurn, D.M., Miesner, H.-J., Chikkatur, A.P., Ketterle, W.
Spin domains in ground-state Bose-Einstein condensates
Nature **396**, 345-348 (1998)
- [88] Chang, M.S., Hamley, C.D., Barrett, M.D., Sauer, J.A., Fortier, K.M., Zhang, W., You, L., Chapman, M.S.
Observation of Spinor Dynamics in Optically Trapped ^{87}Rb Bose-Einstein Condensates
Phys. Rev. Lett. **92**, 140403 (2004)
- [89] Granade, S.R., Gehm, M.E., O'Hara, K.M., Thomas, J.E.
All-Optical Production of a Degenerate Fermi Gas
Phys. Rev. Lett. **88**, 120405 (2002)
- [90] Kuppens, S.J.M., Corwin, K.L., Miller, K.W., Chupp, T.E., Wieman, C.E.
Loading an optical dipole trap
Phys. Rev. A **62**, 013406 (2000)
- [91] Ahmadi, P., Timmons, B.P., Sunny, G.S.
Geometrical effects in loading of an optical atom trap
Phys. Rev. A **72**, 023411 (2005)
- [92] Urey, H.
Spotsize, depth-of-focus, and diffraction ring intensity formulas for truncated Gaussian beams
APPLIED OPTICS **43**, No.3 620-625 (2004)
- [93] Han, D.J., DePue, Marshall T., Weiss, D.S.
Loading and compressing Cs atoms in a very far-off-resonant light trap
Phys. Rev. A **63**, 023405 (2001)
- [94] Takasu, Y., Honda, K., Komori, K., Kuwamoto, T., Kumakura, M., Takahashi, Y., Yabuzaki, T.
High-Density Trapping of Cold Ytterbium Atoms by an Optical Dipole Force
Phys. Rev. Lett. **90**, 023003 (2003)

- [95] Hammes, M., Rychtarik, D., Nägerl, H.-C., Grimm, R.
Cold-atom gas at very high densities in an optical surface microtrap
Phys. Rev. A **66**, 051401 (2002)
- [96] Kraemer, T., Herbig, J., Mark, M., Weber, T., Chin, C., Naegerl, H.-C., Grimm, R.
Optimized production of a cesium Bose-Einstein condensate
Appl. Phys. B 79 Nr. 8 1013-1019 (2004)
- [97] Stamper-Kurn, D. M., Miesner, H.-J., Chikkatur, A. P., Inouye, Stenger, J., Ketterle, W.
Reversible Formation of a Bose-Einstein Condensate
Phys. Rev. Lett. **81**, 2194-2197 (1998)
- [98] Bagnato, V., Pritchard, D. E., Kleppner, D.
Bose-Einstein condensation in an external potential
Phys. Rev. A **53**, 4354-4358 (1987)
- [99] Messiah, A.
Quantum Mechanics
Dover Publications (1999)
- [100] Li, M., Chen, L., Chen, Ch.
Density of states of particles in a generic power-law potential in any dimensional space
Phys. Rev. A **59**, 3109-3111 (1999)
- [101] O'Hara, K.M.
Optical Trapping and Evaporative Cooling of Fermionic Atoms
Thesis, Duke University (2000)
- [102] Luiten, O.J., Reynolds, M.W., Walraven, J.T.M.
Kinetic theory of the evaporative cooling of a trapped gas
Phys. Rev. A **53**, 381-389 (1996)
- [103] Sebby-Strabley, J., Newell, R.T., Day, J.O., Brekke, E., Walker, T.G.
High-density mesoscopic atom clouds in a holographic atom trap
Phys. Rev. A **71**, 021401(R) (2005)
- [104] Shvarchuck, I., Buggle, Ch., petrov, D.S., Kemmann, M., von Klitzing, W., Shlyapnikov, G.V., Walraven, J.T.M.
Hydrodynamic behavior in expanding thermal clouds of ^{87}Rb
Phys. Rev. A **68**, 063603 (2003)
- [105] Kagan, Yu., Surkov, E.L., and Shlyapnikov, G.V.
Evolution of a Bose gas in anisotropic time-dependent traps
Phys. Rev. A **55** R18 (1997)
- [106] de Echaniz, S.R., Mitchell, M.W., Kubasik, M.K., Koschorreck, M., Crepaz, H., Eschner, J., Polzik, E.S.
Conditions for spin squeezing in a cold ^{87}Rb ensemble
J. Opt. B: Quantum Semiclass. Opt. **7**, 548-552 (2005)
- [107] Julsgaard, B., Kozhokin, A., Polzik, E.S.
Experimental long-lived entanglement of two macroscopic objects
Nature **413**, 400-403 (2001)

- [108] Hald, J., Sørensen, J.L., Schori, C., Polzik, E.S.
Spin squeezed atoms: A macroscopic entangled ensemble created by light
Phys. Rev. Lett. **83**, 1319-1322 (1999).
- [109] Hammerer, K., Mølmer, K., Polzik, E.S., Cirac, J.I.
Light-matter quantum interface
Phys. Rev. A **70**, 044304 (2004)
- [110] Madsen, L.B., Mølmer, K.
Spin squeezing and precision probing with light and samples of atoms in the Gaussian description
Phys. Rev. A **70**, 052324 (2004)
- [111] J. H. Müller, J.H., Petrov, P., Oblak, D., Garrido Alzar, C.L., de Echaniz, S.R., Polzik, E.S.
Diffraction effects on light-atomic-ensemble quantum interface
Phys. Rev. A **71**, 033803 (2005)
- [112] Kitagawa, M., Ueda, M.
Squeezed spin states
Phys. Rev. A **47**, 5138-5143 (1993)
- [113] Sørensen, A.S., Mølmer, K.
Entanglement and Extreme Spin Squeezing
Phys. Rev. Lett. **86**, 4431 - 4434 (2001)
- [114] Beijerinck, H.C.W.
Rigorous calculation of heating in alkali-metal traps by background gas collisions
Phys. Rev. A **61**, 033606 (2000)
- [115] Ellinger, K., Cooper, J., Zoller, P.
Light-pressure force in N-atom systems
Phys. Rev. A **49**, 3909-39033 (1994)
- [116] Aspect, A., Arimondo, E., Kaiser, R., Vansteenkiste, N., Cohen-Tannoudji, C.
Laser Cooling below the One-Photon Recoil Energy by Velocity-Selective Coherent Population Trapping
Phys. Rev. Lett. **61**, 826 - 829 (1988)
- [117] Kasevich, M., Chu, S.
Laser cooling below a photon recoil with three-level atoms
Phys. Rev. Lett. **69**, 1741 - 1744 (1992)
- [118] Cirac, J. I., Zoller, P., Kimble, H. J., Mabuchi, H.
Quantum state transfer and entanglement distribution among distant nodes in a quantum network.
Phys. Rev. Lett. **78**, 3221(1997)
- [119] Kuhn, A., Hennrich, M., Rempe, G.
Deterministic single-photon source for distributed quantum networking
Phys. Rev. Lett. **89**, 067901 (2002)
- [120] Raimond, J. M., Brune, M., Haroche, S.
Manipulating quantum entanglement with atoms and photons in a cavity
Rev. Mod. Phys. **73**, 565 (2001)

- [122] Kuzmich, A., Bigelow, N. P., Mandel, L.
Atomic quantum non-demolition measurements and squeezing
Europhys. Lett. **42**, 481 (1998)
- [121] Hald, J., Sørensen, J. L., Schori, C., Polzik, E. S.
Spin squeezed atoms: A macroscopic entangled ensemble created by light.
Phys. Rev. Lett. **83**, 1319 (1999)
- [123] Kozhokin, A. E., Mølmer, K., Polzik, E. S.
Quantum memory for light.
Phys. Rev. A **62**, 033809 (2000)
- [124] Eisaman, M. D., Andre, A., Massou, F., Fleischhauer, M., Zibrov, A. S., Lukin, M. D.
Electromagnetically induced transparency with tunable single-photon pulses.
Nature **438**, 837-841 (2005)
- [125] Sherson, J.F., Krauter, H., Olsson, R.K., Julsgaard, B., Hammerer, K., Cirac, J.I., Polzik, E.S.
Quantum teleportation between light and matter
Nature **443**, 557-560 (2006)
- [126] Wiseman, H. M.
In-loop squeezing is like real squeezing to an in-loop atom
Phys. Rev. Lett. **81**, 3840-3843 (1998)
- [127] van Handel, R., Stockton, J., Mabuchi, H.
Modelling and feedback control design for quantum state preparation
J. Opt. B: Quantum Semiclass. Opt. **7** 179-197 (2005)
- [128] Julsgaard, B., Sherson, J., Cirac, J.I., Fiurásek, J., Polzik, E.
Experimental demonstration of quantum memory for light
Nature **432**, 482 - 486 (2004)
- [129] Saffman, M., Walker, T.G.
Analysis of a quantum logic device based on dipole-dipole interactions of optically trapped Rydberg atoms
Phys. Rev. A **72**, 022347 (2005)
- [130] Shvarchuck, I., *et al.*
Hydrodynamic behavior in expanding thermal clouds of Rb
Phys. Rev. A **68**, 063603 (2003).
- [131] Grimm, R., Weidemüller, M., Ovchinnikov, Yu.B.
Optical dipole traps for neutral atoms
Adv. At. Mol. Opt. Phys. **42**, 95 (2000)
- [132] Comparat, D., Fioretti, A., Stern, G., Dimova, W., Laburthe Tolra, B., Pillet, P.
Optimized production of large Bose-Einstein condensates
Phys. Rev. A **73**, 043410 (2006)
- [133] Green, C.H., Dickinson, A.S., Sadeghpour, H.R.
Creation of Polar and Nonpolar Ultra-Long-Range Rydberg Molecules
Phys. Rev. Lett. **85**, 2458 - 2461 (2000)

- [134] Greene, C.H., Hamilton, E.L., Crowell, H., Vadla, C., Niemax, K.
Experimental Verification of Minima in Excited Long-Range Rydberg States of Rb₂
Phys. Rev. Lett. **97**, 233002 (2006)
- [135] Liu, I.C.H., Rost, J.M.
Polyatomic molecules formed with a Rydberg atom in an ultracold environment
Eur. Phys. J. D **40**, 65 (2006).
- [136] Tong, D., Faroogi, S.M., Stanojevic, J., Krishnan, S., Zhang, Y.P., Coté, R., Eyler, E.E., Gould, P.L.
Local Blockade of Rydberg Excitation in an Ultracold Gas
Phys. Rev. Lett. **93**, 063001 (2004)
- [138] Gerbier, F., Thywissen, J.H., Richard, S., Hugbart, M., Boyer, P., Aspect, A.
Critical Temperature of a Trapped, Weakly Interacting Bose Gas
Phys. Rev. Lett. **92**, 030405 (2004)
- [137] Ahmadi, P., Behinaein, G., Timmons, B.P., Summy, G.
Experimental investigation of optical atom traps with a frequency jump
J. Phys. B: At. Mol. Opt. Phys. **39** 1159-1168
- [139] Menotti, C., Pedri, P., Stringari, S.
Expansion of an Interacting Fermi Gas
Phys. Rev. Lett. **89**, 250402
- [140] Pitaevskii, L., Stringari, S.
Bose-Einstein Condensation
Clarendon Press, Oxford (2003)
- [141] van Kempen, E.G.M., Kokkelmans, S.J.J.M.F., Heinzen, D.J., Verhaar, B.J.
Interisotope Determination of Ultracold Rubidium Interactions from Three High-Precision Experiments
Phys. Rev. Lett. **88**, 093201 (2002)
- [142] Pedri, P., Guéry-Odelin, D., Stringari, S.
Dynamics of a classical gas including dissipative and mean-field effects
Phys. Rev. A **68**, 043608 (2003)
- [143] Gensemer, S.D., Sanchez-Villicana, V., Tan, K.Y.N., Grove, T.T., Gould, P.L.
Trap-loss collisions of ⁸⁵Rb and ⁸⁷Rb: Dependence on trap parameters
Phys. Rev. A **56**, 4055-4063 (1997)
- [144] Kubasik, M.
Private communication
ICFO (2006)
- [145] Steck, D.A.
Rubidium 87 D Line Data
Los Alamos National Laboratory, revision 1.6 (2003)
- [146] Beijerinck, H.C.W.
Heating rates in collisionally opaque alkali-metal atom traps: Role of secondary collisions
Phys. Rev. A **62**, 063614 (2000)

-
- [147] Nesnidal, R., Walker, T.
Light-induced ultracold spin-exchange collisions
Phys. Rev. A **62**, 030701 (2000)
- [148] Burke, J., Bohn, J., Esry, B.D., Green, Ch.H.
Impact of the 87Rb singlet scattering length on suppressing inelastic collisions
Phys. Rev. A **55**, R2511 - R2514 (1997)
- [149] Cline, R.A., Miller, J.D., Matthews, M.R., Heinzen, D.J.
Spin relaxation of optically trapped atoms by light scattering
Opt. Lett. **19**, 3 207-209 (1994)
- [150] Koschorreck, M.
Private communication
ICFO (2007)

Acknowledgements

First of all I have to say that I cannot express the magnitude of debt that I owe to all the people who contributed to this work and supported me over the years.

I thank Rainer Blatt for accepting the role as my supervisor, for having ambitious ideas for the experiment and for showing me how to run efficiently a large, world class research group.

I'm indebted to Jürgen Eschner, who as my project supervisor from the start of my diploma thesis on, supported me always strongly throughout all the years and in difficult times. He also provided me with the opportunity to follow him to sunny Spain. I wish him all the best with his rapidly expanding team and some more TV interviews.

One, who always succeeded to amaze me with his vast knowledge about physics is Morgan Mitchell. He contributed substantially behind the scene to the success (and safe relocation) of the atom trap experiment. I'm convinced that he and his team will earn the fruits of hard work, preferably with a string of Nature papers.

Special thanks goes to Sebastian de Echaniz. He convinced us that indeed a rubidium atom could pass as a fake electron at the border control station of Spin-land.

Thanks too to Marcin Kubasik and Marko Koschorreck who's PhD work ran parallel to my own and so were often in the same situation as I was. Their invaluable help in setting up the system will never be forgotten.

A large part of the praise deserves the management unit and the technical workshop staff. Their unconditional support when I had to fight against the odds in the Omega building and their constant efforts to improve research conditions is warmly recognized. Numerous more people from all over the world provided a culturally rich experience and made ICFO an enjoyable place for doing research. Thanks to all of them.

My parents who always stood by my side and occasionally even showed interest in my work. Unfortunately my father died unexpectedly in February 2006 and therefore cannot share my success. Thank you both for all the love you showed to me.